STRUCTURE-BORNE NOISE OF MARINE DIESEL ENGINES: TRANSFER-PATH ANALYSIS OF ONBOARD TRANSMISSION AND UNDERWATER RADIATION

by © Jacopo Fragasso

A Thesis submitted to the School of Graduate Studies

in partial fulfillment of the requirements for the degree of

Doctor of Philosophy

Ocean and Naval Architectural Engineering

Faculty of Engineering and Applied Science

Memorial University of Newfoundland

June 1, 2023

St. John's, Newfoundland and Labrador, Canada

Abstract

Onboard machinery generates structure-borne noise that propagates onboard and underwater. Structure-borne noise has a direct influence on the onboard noise comfort and the underwater noise footprint of the vessel. Vibrational transfer-path analysis (TPA) can be used to understand how noise is transmitted from onboard noise sources to the ship structures or radiated underwater. The focus of this research is on the noise radiated from resiliently-mounted marine diesel engines because of their dominant impact on the noise signature of the vessel.

With TPA, the main components of the vibrational transfer path are analyzed separately and then combined together. Noise levels at the receiver can be reduced by identifying the critical points in the transfer path and improving their design. The characterization of the vibration isolator mounted under the diesel engine is performed with the use of numerical models built and validated with the aid of experimental tests and response surface methodology (RSM). Similarly, a finite-element model for the analysis of underwater sound radiation of vibrating structures is developed using sound and vibration measurements acquired with acoustic measurements in a water tank.

This work presents an experimental procedure for the characterization of the vibration isolator at different static preloads. The dynamic response of a numerical simulation is fit to the experimental response using a hyperelastic material model and an implicit time-integration scheme. Moreover, the coupled acoustic-structural analysis of the underwater radiation yields accurate results and provides a coefficient of sound radiation (σ). An

analytical formulation of the transfer path is developed to combine the contributions of the components of the transfer path to estimate noise and vibration levels at the receiving point.

This thesis highlights the importance of numerical models in the TPA of structure-borne noise and shows how dynamic simulations can help ship designers estimate the contribution of the components of the transfer path using standardized testing procedures and model-scale experiments.

Acknowledgements

I would like to personally thank my supervisor, Dr. Lorenzo Moro. His motivation, guidance and expertise made the completion of this work possible.

I would also like to extend my gratitude to my supervisory committee, Dr. Bruce Colbourne and Dr. Bruce Quinton, for their valuable support and contribution to the development of this research project.

Finally, a special thanks goes to my parents, for the trust and encouragement during the time I have been working on this thesis.

We acknowledge the support of the Natural Sciences and Engineering Research Council of Canada (NSERC), [funding reference number 211146].

Cette recherche a été financée par le Conseil de recherches en sciences naturelles et en génie du Canada (CRSNG), [numéro de référence 211146].

Table of contents

List of Tables

List of Figures

Chapter 1

Introduction

1.1. Leading drivers for the investigation of sound and vibration produced by onboard sources and transmitted to the ship structures and underwater

In the marine industry, the reduction of sound and vibration levels generated onboard is currently one of the main areas of investigation.

Onboard-generated noise and vibration have a direct influence on a large number of issues related to vessels' comfort, habitability, health and safety of crew members, and the vessel's impact on the surrounding marine environment. The most relevant issues are discussed hereafter.

1.1.1. Comfort and habitability of crew spaces

Comfort and habitability of crew spaces are key issues on all ships. I identified three categories where structure-borne noise needs to be accurately controlled and regulated: passenger ships, fishing vessels, and navy ships.

In the case of passenger ships, reducing structure-borne noise and vibration is one of the key aspects of onboard comfort [11]. This issue is related to several criteria, including aesthetics, ergonomics, acoustics, and temperature. Among them, noise comfort is the factor having the highest effect on the overall desirability of the ship. The report [94] highlights the importance of noise and low-frequency vibrations in the desirability of ferry boats for passenger transportation: in the feedback acquired from the passengers, noise and low-frequency vibrations had primary relevance in the comfort perception experienced onboard. Furthermore, the need for effective solutions to improve onboard noise comfort emerges as the main area of improvement in a survey conducted on cruise ships' crew during sea trials, discussed in [40], and significantly contributes to the comfort assessment of luxury vessels [97].

In the marine fisheries sector, exposure to hazardous levels of structure-borne noise is a well-documented issue [74, 110], which majorly affects the safety of fishing vessels. The study [16] summarizes the body of research performed in this field and highlights the need for design interventions to improve vessels' noise safety. In particular, ship designers have to identify the dominant transfer paths of sound transmission and optimize the vibration characteristics of the interested ship's components [15].

In the naval field, shipboard habitability is strongly related to noise comfort. The study [102] analyzes the results of a survey about the quality of shipboard life conducted on US Navy sailors. High noise levels in crew spaces are identified as one of the most dissatisfying aspects of shipboard life, negatively influencing the sailors' retention plans. Furthermore, in the study [90], the sleep quality of a sample group of Royal Norwegian Navy officers and sailors was monitored using actiwatches. During active duty, the test subjects were exposed to a 65 dB continuous noise level onboard. The analysis shows the negative impact of onboard noise levels on the seamen's sleep quality.

1.1.2. Underwater sound radiation

In addition to the noise comfort of the vessel, the control of structure-borne noise generated onboard is critical for reducing the underwater noise radiated from the ship [57, 95]. This is of primary importance in the marine industry because of the negative effects on the marine fauna [53]. The negative impact of ship-generated underwater noise on marine fauna is documented [25, 29, 53, 86, 103], especially in the case of marine mammals: for example, [101] reported changes in vocalizations, respiration, swim speed, diving, and foraging behaviour in response to increased levels of shipping noise in several different species of marine mammals.

International maritime trade has increased considerably in the last 50 years. The UNCTAD yearly review [87] reports an increase in the total cargo loaded from 2605×10^6 t (1970) to $10\,985 \times 10^6$ t (2021). After the temporary decline in the international maritime trade caused by the COVID pandemic, the growth in this sector is estimated at 3.2% per year

[87]. As a consequence, underwater noise has increased considerably [75]. With regards to the polar environment, a recent study from the Arctic Council reports that underwater noise in some areas has effectively doubled since 2013 [76].

Over the past fifty years, the rapid expanse of marine traffic and the increasing use of seismic surveys and scanning sonars have significantly increased the anthropogenic impact on underwater sound radiation [75]. In particular, commercial shipping activities are the primary cause of the increase in ocean ambient noise [2].

The recognition of short- and long-term consequences of exposure to hazardous noise levels on marine life, combined with the increasing environmental pressure on the marine ecosystem, has caused the International Maritime Organization (IMO) to ratify voluntary guidelines in 2014 [45] to address the adverse impacts of shipping noise.

In addition, the scientific and technical community has developed procedures to control vessels' underwater radiated noise (URN) by measuring and characterizing ships as underwater sound sources, simulating ships' URN, and developing technology to control the URN of existing and new ships. ISO and ANSI Standards define the methodology to measure underwater noise radiated from ships under prescribed operating conditions [3, 47]. ITTC Guidelines [48] developed an experimental procedure for the measurement of underwater noise radiation in model-scale facilities in standardized conditions.

1.2. Transfer-path analysis of structure-borne noise produced by the marine diesel engine

Onboard noise and vibration are generated by a large number of sources, including the prime movers, the propeller and components of the shaft line, the air conditioning systems, the maneuvering devices, auxiliary machinery and the noise generated by the impact of the hull onto the sea surface [18].

Among them, medium-speed diesel engines generally produce the highest amount of structure-borne noise and vibrations transmitted to the surrounding structures [70, 109]. Moreover, the prime mover is a dominant noise source in the marine vessel underwater-noise footprint [89]. Its contribution is especially notable in the case of low-power vessels and ships moving at low speed [1, 100]. In the case of two-stroke diesel engines, the lack of well-defined tonal components makes the analysis of the engine sound spectra challenging [104].

For this reason, it is crucial to understand how the vibrations are transmitted from the marine diesel engine to the receiving structures in order to reduce the vibration levels measured onboard. This is done using Transfer Path Analysis (TPA), a large group of experimental techniques that allows the designer to represent the transmission of vibrational energy in terms of forces and vibrations displayed at the interface with the receiving point [4]. The original problem is then split into the analysis of the source excitation and the representation of the structural/acoustic transfer characteristics. By doing so, the dominant

paths of vibration transmission can be identified, and the designer can make changes to the vibration source (in this case, the marine diesel engine) or the components of the transfer path to reduce the transmission of structure-borne noise [96].

Figure 1.1 shows how noise and vibration produced by the diesel engine are transmitted to the surrounding environment. These transmission paths can be classified into two categories [69]:

1. first-order structure-borne noise (paths #1,3,4,5): the vibrational energy is transmitted to the ship structures through solid structures: the resilient mounting elements (#1), the flexible pipes (#3), the flexible coupling between the diesel engine and the gearbox(#4), and the flexible connection between the diesel engine and the exhaust gas system (#5);

2. second-order transmission paths (path #2): sound radiated from the engine to the surrounding environment through the air medium. Subsequently, sound waves may transmit energy back to the ship structures in the form of vibrational waves [30].

The components of the transfer path of structure-borne noise generated by the marine diesel engine have been the topic of recent research studies. The works [9, 34, 35, 71] focus on the dynamic characterization of the vibration isolator mounted under the diesel engine. The dynamics of the engine foundation was analyzed in [58] using modal techniques and in [44, 59, 81] with Statistical Energy Analysis (SEA). The paper [15] presents an application of SEA for the characterization of the transfer path in the vibration analysis of small fishing vessels.

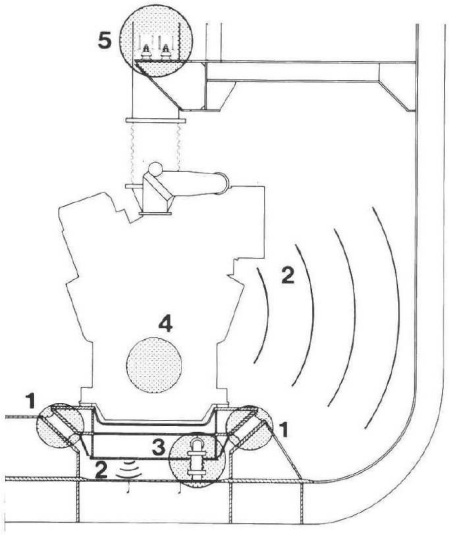

Figure 1.1: Main sound transfer paths from a marine diesel engine to the adjacent ship structures [98]

1.3. Characterization of the resilient mounting element

A crucial component of the TPA of marine structures is the dynamic characterization of the vibration isolators placed between the marine diesel engine and the ship foundation. These elements need to be accurately modeled, as they have primary importance in the reduction of the vibration levels detected at the receiving location [98]. A wide variety of vibration isolators are commercially available, with different sizes and shapes (generally cylindrical, conical, or parallelepipedal) and featuring different connections to the engine feet and the foundation. These components are characterized by their efficiency along all directions and in the design technique implemented to reduce the vibrational energy transmission, generally by using rubber of different Shore hardness or metal inserts [70]. To represent the effect of the resilient mount using TPA, the designer needs to know the element's structural/acoustic properties.

Several sources of nonlinearity need to be taken into account in the characterization of vibration isolators. These are related to the non-linear stress-strain relation of the rubber material within the isolator [88] and the dynamic nonlinearities caused by the internal resonances of this element [27].

The work [9] outlines a two-step procedure to obtain an accurate characterization of a simple resilient mounting element that can accurately represent the effect of the material nonlinearities.

The first step of the procedure consists in the analysis of the response of the resilient mounting element to static stress. An experimental force-displacement curve is acquired for a set of displacement values. Then, the parameters of a hyperelastic model are calculated by fitting the behaviour of the finite element model of the resilient mounting element to the experimental force-displacement curve. Geometry and properties of the resilient mounting element are presented in [52], while the details of the fitting procedure are described in [7].

The second step yields the dynamic characterization of the resilient mounting element. The dynamic characterization of the resilient mounting element is performed by finding the optimal value of the shear modulus of the rubber material. The values of the hyperelastic coefficients, calculated with the static characterization of the isolator, are used to represent the rubber material in the numerical model of the dynamic simulations. Similarly to the static characterization, this is done by comparing the numerical and experimental transfer stiffness curves and adjusting the shear modulus coefficients with an iterative procedure.

Moro et al. [69, 71] were able to extend the approach presented by Beijers et al. [9] to the case of resilient mounting elements having a more complex geometry: while the work by

Beijers et al. analyzed a rubber cylinder constrained between two steel plates, in the paper [71] a similar technique was applied to the analysis of a marine resilient mounting element designed for medium-speed diesel engines. The difficulties to overcome in order to extend this approach are related to the complex representation of the contact between the rubber isolator and the steel cups and the use of a multi-dimensional state of stress. The transfer mobility function of the isolator, expressing the frequency-dependent ratio between the velocity levels measured on the top surface of the isolator and the force levels estimated on the bottom surface, is measured using an experimental test rig. Then, a finite-element model is created to represent the modal behaviour of the isolator. The dynamic coefficients of this model are iteratively changed in order to optimize the fit to the experimental measures.

1.4. Modelling of underwater sound radiation

Providing naval architects with tools to simulate ships' URN is of utmost importance as they can assess any hazardous URN noise levels in the early design phases of new ships and evaluate alternative design solutions. Due to the rapid increase in marine traffic, the problem of estimating and controlling the levels of acoustic noise radiated underwater from marine vessels has acquired primary importance [60].

The analytical representation of radiated underwater noise requires the accurate characterization of the radiating source, the components of the transfer path, and the sound radiation environment since the early design stage.

An analytical representation of the radiation of structure-borne sound in a fluid is

available only for simple geometries and ideal boundary conditions [108]. In order to analyze more complex setups and material models, researchers have to rely on empirical representations and numerical modelizations [60].

In the review presented in [79], it is noted that the validation of numerical predictive models developed for plate-like structures rely on the benchmark case of sound radiation models of flat rectangular plates in the air.

On the other hand, empirical models to represent underwater noise are based on full-scale field measurements, which are not available during the design stage, and they can estimate the vessel's noise signature accurately only within certain frequency bands and specific operating conditions [53]. Moreover, these models depend on the specific features of the ship under analysis, and the results cannot be easily generalized to a broader vessel population. In [53] Kellett et al. cite the statistical analysis by Gray and Greeley about underwater noise radiation from cavitating propellers in single-screw merchant vessels presented in [41], as an example of this type of model.

1.4.1. Experimental analysis of the relationship between shipboard sources and underwater noise

The reduction of underwater noise levels requires an accurate investigation of the relationship between vibration levels measured in the proximity of the onboard noise sources and at the underwater receivers.

In [49], the noise source levels of a cavitating propeller are estimated from the measured sound levels on an array of hydrophones. The authors develop a simple beamforming method

for propeller noise monitoring, validated with the results of the model-scale experimental setup.

Turkmen et al. [95] perform full-scale measurements of underwater noise and onboard vibrations on a research vessel. Onboard noise levels caused by the propeller cavitation were measured with accelerometers placed on the hull structure and the engine foundation, and underwater radiated noise was measured with an array of hydrophones. Tests were repeated for different engine speeds. The authors observe a linear relationship between onboard vibration and offboard noise in the lower frequency range (0-500 Hz).

The work [57] characterizes the underwater radiated noise generated by a coastal tanker under design loading conditions. The authors examine the correlation between full-scale on-site measurements of onboard vibration and underwater noise, model testing in a cavitation tunnel, and the results of hybrid CFD methods. The underwater noise radiation predicted with the model testing has a good correlation with the full-scale noise spectra. The tip vortex cavitation measured in sea trial and model tests is captured by the hybrid CFD method, but the predicted strength and extension were underestimated.

The work [21] analyses the acoustic signature of a Royal Canadian Navy (RNC) Orca-class training vessel. Onboard vibration is measured in the proximity of the most prominent sources, and underwater sound levels are detected by two hydrophones at depths of 25.3 m and 42 m, respectively. The authors identify a transfer function specific to the vessel under analysis that relates the average velocity levels of the onboard noise sources to a prediction of underwater sound levels in the frequency range 10-10 000 Hz.

These works define a relationship between onboard vibration levels and underwater

radiated noise for a variety of full-scale case studies. However, their results are restricted to a specific experimental setup or a limited frequency range. Global models to estimate the impact of onboard noise sources on the vessel noise footprint are still missing.

1.5. Contributions of this research activity

This thesis presents a procedure to characterize the components of the vibrational transfer path of structure-borne noise produced by onboard noise sources. This procedure relies on the use of numerical models that predict the dynamic behaviour of the components of the transfer path, and an analytical single-point model of vibration transmission, that combines the contribution of each element.

The focus is on the marine diesel engine, because of its primary role in the vessel's noise signature, and the resilient mount, because the analysis of its static and dynamic response presents several challenging aspects.

The procedure has been developed through the steps presented in the following Sections.

1.5.1. Static characterization of the resilient mount

In this work, the numerical model of the axial compression of the resilient mounting element is run using an implicit time-integration solver using the Newmark-Beta method, as it allows for a significantly larger time step and simulates the compression test of the resilient mount in significantly less time than explicit time-integration schemes.

Moreover, the comparison between the experimental force-displacement curve and the

results of the numerical model is conducted using Response Surface Methodology (RSM) to create a set of numerical models defined by different rubber properties and produce a predictive equation, relating the values of the coefficients of the hyperelastic material model to the global fitting performance of the system. It is possible to estimate the importance of each coefficient of the material model in the global behaviour of the numerical system and to find the best values of the coefficients following a simple optimization procedure.

The choice of RSM is supported by the several advantages it has over classical optimization methods, where the optimal values of the independent variables are estimated via sequential search (one-factor-at-a-time, OFAT technique). OFAT procedures are followed in [7] and [71] to calculate the best values of the Yeoh coefficients. The advantages of RSM, highlighted in [5] and [24], relate to the higher efficiency of RSM techniques (as classical experimental techniques cannot predict the behaviour of a system over the design space using a small number of experiments) and the possibility of observing the interaction effect between the independent variables. RSM is based on the factorial design approach, saying that the experimenter should vary all independent variables simultaneously and perform the experiments in random order to maximize accuracy and reduce the chance of wrong conclusions [64]. This work presents the first application of Response Surface Methodology for the mechanical characterization of rubber components.

This work aims to provide a framework of reference for the characterization of resilient mounting elements, to be used to predict the reduction in vibration levels produced by the marine diesel engine and transmitted to the ship structure. Following this set of techniques, the ship designer will be able to improve the comfort onboard from the early stages of the

project.

1.5.2. Dynamic characterization of the resilient mount

Previous research activities on the dynamic characterization of vibration isolators have focused on the detailed analysis of the mechanical properties of the rubber compounds used in resilient mounting elements [51] or have described the vibroacoustic characterization of isolators with an experimental methodology [8, 71]. To my knowledge, a comprehensive design procedure to estimate the mechanical properties of resilient mounting elements with complex geometries, based on a numerical modelization and the results of experimental tests, has never been developed.

I performed an experimental campaign to estimate the experimental transmissibility function of the vibration isolator. This was calculated by measuring the acceleration levels on the top and bottom surfaces of the resilient mounting element under a uniform excitation in the frequency range 100-1000 Hz. The test rig, built following the guidelines of ISO Standard 10846 [28], is designed to mechanically insulate the element under test from the rest of the structure. Vibration levels are measured on the top and bottom surfaces of the resilient mount. Then, a finite-element model for modal analysis is built. The hyperelastic constitutive relation for the rubber material, calculated using the Yeoh model in the quasi-static characterization of the component, is used in this analysis to represent the static force-deformation characteristics of the rubber part of the isolator. The dynamic properties of the isolator are updated by varying the values of the frequency-dependent damping ratio of the rubber material. The use of RSM allows the designer to fit the behavior

of the numerical model to the dynamic stiffness curve measured experimentally using a small number of runs. The optimization can be restricted to the frequency range where the internal resonance modes of the vibration isolator are observed.

Moreover, this work analyzes the effect of the static preload applied to the vibration isolator on the resulting transmissibility curve. This allows the designer to estimate the dynamic properties of the element under test at its intended working condition, and to visualize the effect of the preload on the stiffness of the isolator.

The procedure hereby outlined can be followed by a marine designer to estimate the dynamic behaviour of resilient mounting elements with complex geometries, from the analysis of the results of a mono-axial compression test and vibration measurement.

The described procedure is applied to two case studies, having different shape, size, and load capacity.

1.5.3. Representation of underwater radiated noise with model-scale setup

The transfer-path analysis of structure-borne noise was extended to include the contribution of the engine foundation and the radiation through the water medium. When full-scale data are not available, designers need to estimate these quantities using numerical models and model-scale measurements.

I developed an experimental procedure to represent sound transmission from a model-scale radiating noise source on the water surface to the underwater receiver. Vibration transfer path analysis was used to represent the dynamic behaviour of each component separately and then combine their contributions together.

I built a mock-up model of the engine foundation and tested its dynamic response to harmonic excitation using vibrational modal analysis. I measured the noise levels produced by the mock-up structure suspended over the water tank, with the bottom plate kept at the water level.

The experimental results were compared with the numerical solution produced by a Finite Element (FE) model, in order to estimate the dynamic properties of the mock-up structure and the water tank. I calculated each term of the transfer path, including a coefficient of sound radiation efficiency, in order to estimate the energy transmitted from the engine to the receiver in a broadband representation.

1.6. List of published papers

The list of publications produced during this research activity is attached below. Chapters 2 and 3 describe how each one contributes to that part of the thesis.

1. Fragasso, J., Moro, L., Lye, L., and Quinton, B. W. T. (2019). Characterization of resilient mounts for marine diesel engines: prediction of static response via nonlinear analysis and response surface methodology. *Ocean Engineering*, 171:14–24;

2. Fragasso, J. and Moro, L. (2019). Dynamic analysis of the stationary behavior of resilient mounting elements for marine applications. In *Proceedings of the IMAM Conference, Varna, Bulgaria*;

3. Fragasso, J. and Moro, L. (2019). Design procedure to estimate the mechanical behaviour of resilient mounting elements for marine applications. In *PRADS 2019, 14th*

International Symposium on Practical Design of Ships and Other Floating Structures;

4. Fragasso, J. and Moro, L. (2022). Structure-borne noise of marine diesel engines: Dynamic characterization of resilient mounts. *Ocean Engineering*, 261;

5. Fragasso, J., Helal, K. M., and Moro, L. (2023). Transfer-path analysis to estimate underwater radiated noise from onboard structure-borne sources. *Applied Acoustics*. Manuscript submitted for publication.

Chapter 2

Methods

Section 2.1 was adapted from the paper [35]; Section 2.1.2 was adapted from the papers [32, 33, 34]; Section 2.2 was adapted from the paper [31].

2.1. Characterization of the resilient mount

2.1.1. Static characterization

The procedure followed in this work to perform the static characterization of the resilient mount is represented in the flow chart of Figure 2.1 and briefly described here.

The experimental force-displacement curve is acquired by performing the compression test of the resilient mounting element described in Section 2.1.1.2.

This curve is compared with the results of a set of numerical simulations, performed for different values of the Yeoh coefficients of the numerical model.

The design space for the numerical simulations is defined by selecting the range of

each Yeoh coefficient. This determines the region where the optimal values of the Yeoh coefficients were sought. This step is described in Section 3.1.1.1.

A design is defined in the space region under investigation, using Response Surface Methodology (Section 3.1.1.2).

The table of the design is shown in Table 3.2, composed of sets of Yeoh coefficients, to be tested in the numerical model.

Then, each set of Yeoh coefficients is tested in the numerical model, described in Section 2.1.1.3, to obtain a group of numerical force-displacement curves (one for each run in the design).

The numerical results are then compared with the experimental force-displacement curve by means of a measure of performance. In this work, the Nash-Sutcliffe efficiency index, described in Section 2.1.1.10 is used.

With the computed Nash-Sutcliffe efficiency indexes, a statistical model is fitted to the design points to create a predictive equation. This model needed to be validated by checking the assumptions of the analysis of variance (ANOVA) and testing a set of validation points. The analysis of the computed statistical model is shown in Section 3.1.1.4.

If the validation is successful, the optimal values of the Yeoh coefficients are calculated and tested using the numerical model. Otherwise, the analysis needs further refinement by varying the factors' range or the type of design.

Finally, the optimal values of the Yeoh coefficients are estimated by performing an optimization procedure using the statistical model. The procedure is described in Section 3.1.1.5.

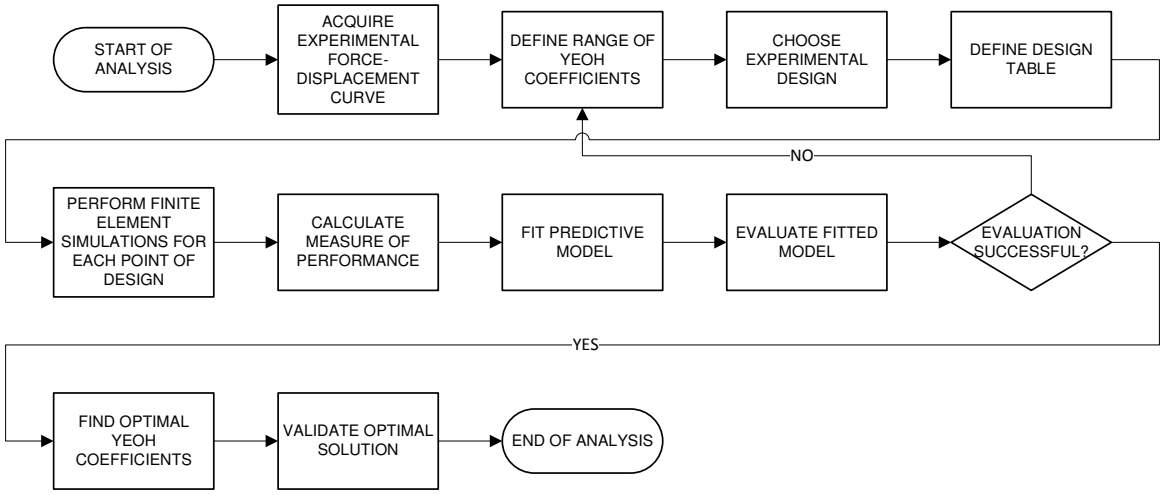

Figure 2.1: Graphical representation of the procedure followed in the static characterization of the isolator

2.1.1.1 The Yeoh model

Rubber materials are extensively used in a wide variety of structural applications because they can experience large non-permanent deformations.

The static and dynamic characterization of rubber materials is complex, as constitutive relations for rubber materials are nonlinear in terms of both material and geometric behaviour.

Furthermore, for a complete characterization of a rubber material, the effects of temperature, environment, strain history, loading rate and amount of strain must be considered. Also, manufacturing process and composition have a significant effect [19].

In engineering applications, complex material models describing the behaviour of rubber elements are generally not readily available to the designer or are kept confidential [9]. Therefore, the material's constitutive relation must be determined experimentally, by conducting a set of tests covering the range of deformations expected by the material under

test [63].

Most of the developed constitutive relations for rubber-like materials represent the material deformation in terms of the elastic strain energy. This theory is based on the statistical mechanical approach presented in [93]. These are hyperelastic material models because the material behaviour is described by means of a potential energy function [6].

The elastic strain energy density W, representing the work that must be done on the unit volume of the material in the unstrained state to deform it to the current configuration, is written as

$$W = \frac{1}{2} N k \theta \left(\lambda_1^2 + \lambda_2^2 + \lambda_3^2 - 3 \right) \tag{2.1}$$

where N is the number of network chains per unit volume, k is Boltzmann's constant, θ is the absolute temperature, and λ_{1-3} are the components of a principal stretch state, defined as the ratio between the current and the original length.

Equation (2.1) can be expressed in the following polynomial form [13]:

$$W = \sum_{i,j=0}^{\infty} C_{ij} \left(I_1 - 3 \right)^i \left(I_2 - 3 \right)^j \tag{2.2}$$

where I_1 and I_2 are the first two invariants of the stretch tensor.

The Yeoh model, introduced in [105], can be obtained from Equation (2.2) by setting: $i = 1, 2, 3$ and $j = 0$:

$$W = C_{10} \left(I_1 - 3 \right) + C_{20} \left(I_1 - 3 \right)^2 + C_{30} \left(I_1 - 3 \right)^3 \tag{2.3}$$

The Yeoh model is one of the most widely used material models for rubber-like materials because it can capture different deformation states at moderate to large deformations for a wide variety of compounds [13]. Its main advantage over other constitutive relations lies in its coefficients being estimated using the data obtained from a simple uniaxial tension test [85] because only the first stretch invariant is considered.

2.1.1.2 Experimental compression test

The uniaxial compression experiments mentioned in Section 2.1.1.1 to obtain the material characteristic of the rubber part of the resilient mount are performed on a resilient mounting element designed by Vulkan Italia Srl for a medium-speed marine diesel engine of rated power of about 16 000 kW. The resilient mount tested in the experiment is shown in Figure 2.2 and Figure 2.3 shows the rubber damper placed inside the steel structure.

A flange (not shown in Figures 2.2 and 2.3) couples the resilient mount with the engine foot. For better engine alignment, the coupling can be adjusted in the vertical direction using a ring nut. The rubber part is a toroidal body coupled by a conical-shaped seat with the resilient mounting base [70].

The compression test on the resilient mounting element was performed at the Ship Noise and Vibration Laboratory of the University of Trieste.

The testing procedure is described in [71] and briefly summarized here.

In order to find the force-displacement curve of the resilient mount, the element was compressed applying an increasing force on the top surface. For every force increment, the corresponding displacement was measured 24 h after the application of the load, to take into

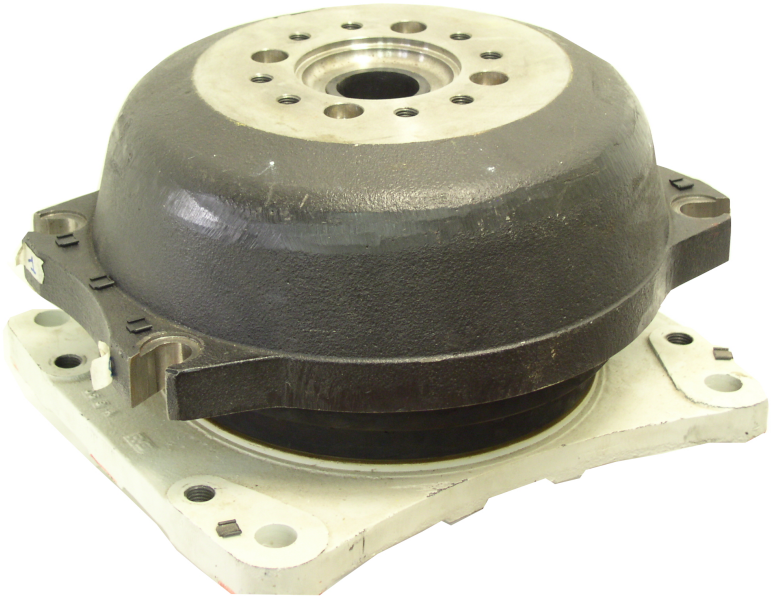

Figure 2.2: Conical resilient mounting element analyzed in the static compression test.

account for the rubber relaxation time. The temperature in the laboratory was kept constant at 20 °C.

The maximum static load for the resilient mounting element is 1.5×10^6 N, so the tests cover the entire design loading range. Generally, this element is used for a static load of 8×10^5 N.

The force-displacement curve obtained from the experimental test is shown in Figure 2.4.

Figure 2.3: Components of the conical resilient mount under test

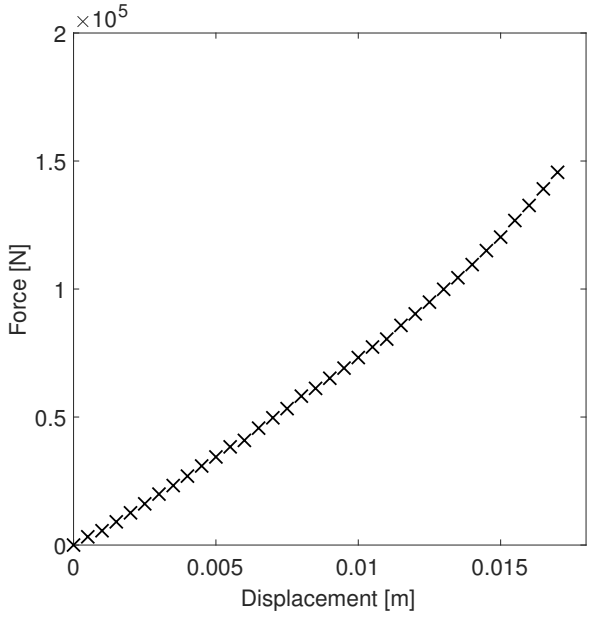

Figure 2.4: Experimental force-displacement curve, from [71]

2.1.1.3 Numerical simulation

The experimental compression test described in Section 2.1.1.2 is simulated using a Finite Element model, with an implicit time-integration solution.

The geometry of the finite element model is shown in Figures 2.5 and 2.6, representing a global view of the model and its midpoint cross-section, respectively.

The mesh is composed of 162 190 nodes and 142 328 8-noded hexahedral reduced-integration solid elements to avoid the problem of volumetric locking experienced when using fully-integrated elements in conditions close to the incompressibility limit. The characteristic length of the solid elements is in the interval $[1.371, 6.704] \times 10^{-3}$m. The optimal mesh size was determined by conducting a mesh convergence analysis.

The nodes on the bottom surface of the model are fully constrained, and the nodes of the inner surface of the flange are only allowed to translate in the vertical direction.

The load is applied fixing the vertical displacement of the nodes on the top surface of the flange for a set of increments.

The steel parts of the resilient mount (green and red parts of Figures 2.5 and 2.6) are modeled using a linear elastic model. Relevant material properties are listed in Table 2.1.

The rubber material (blue part of Figures 2.5 and 2.6) is represented in the numerical simulation using a general hyperelastic rubber model, implemented in LS-DYNA® by the card MAT_HYPERELASTIC_RUBBER [62]. Hyperelastic constants are input directly (N = 0), using the values of the table of designs defined in the response surface analysis. Other relevant material properties are listed in Table 2.2. The sets of Yeoh coefficients

(C_{10}, C_{20}, C_{30}) used in the definition of the material model are defined using the procedure presented in this work.

Contact is represented in the model using the LS-DYNA® contact algorithm designed for tying solid elements to solid elements in an implicit simulation. The algorithm is implemented using the card CONTACT_TIED_NODES_TO_SURFACE. The strongly objective formulation is implemented (IACC = 1), to transform correctly forces and moments under superposed rigid body motions within a single implicit step [61].

Table 2.1: Material properties of the steel parts of the finite element model of the conical resilient mount

Property	Value
Mass density	$7850\,\mathrm{kg/m^3}$
Young's modulus	$2.000 \times 10^{11}\,\mathrm{Pa}$
Poisson's ratio	0.3

Table 2.2: Material properties of the rubber part of the finite element model of the conical resilient mount

Property	Value
Mass density	$1050\,\mathrm{kg/m^3}$
Poisson's ratio	0.4998

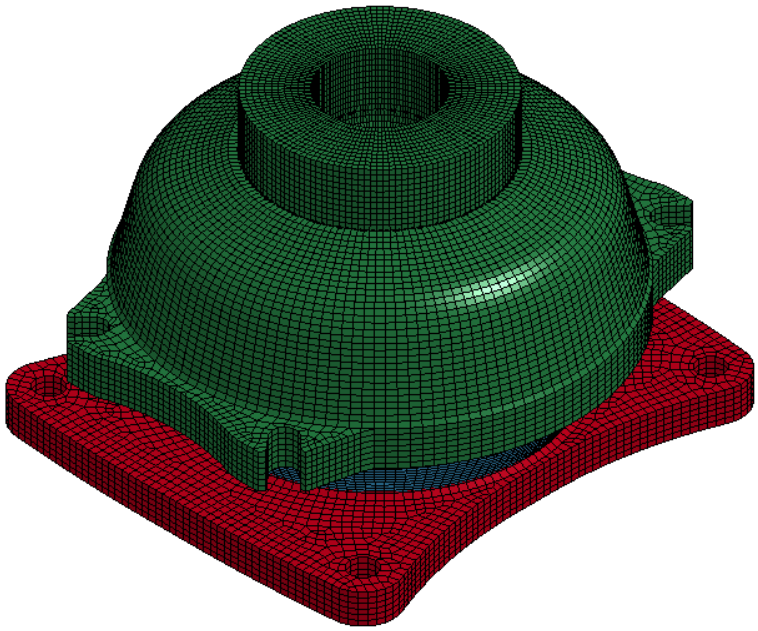

Figure 2.5: Mesh of the conical resilient mount assembly

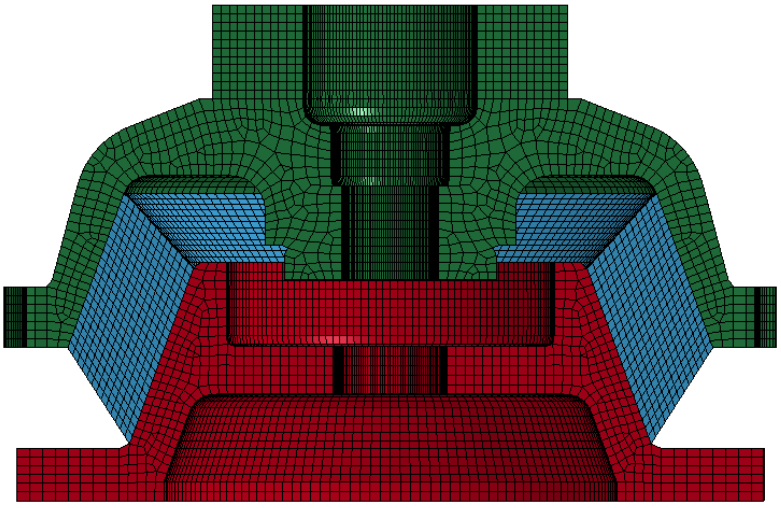

Figure 2.6: Cross-section of the conical resilient mount assembly mesh

2.1.1.4 Experimental design

The coefficients of the Yeoh model described in Section 2.1.1.1 for the rubber material of the numerical model of the resilient mount under test are estimated using Response Surface Methodology (RSM).

RSM is part of a group of statistical and mathematical techniques known as Design of Experiments (DOE), that can be used to investigate the effect of a group of independent variables (considered alone or in combination) on the behaviour of a system and to represent the behaviour of the system in a design space using a mathematical model, obtained by regression procedure. The graphical representation of the predictive mathematical model has led to the term Response Surface Methodology [72].

In the work [20], several statistical methods are compared for the design and analysis of computer experiments. For the case of small-scale problems, RSM techniques are a good choice, because they are reliable and easy to construct and understand.

RSM represents the relationship between the response and the input using the following general equation:

$$\xi = f\left(X_1, \ldots, X_k\right) + \varepsilon \tag{2.4}$$

where ξ is the response, f is the true response function, unknown to the experimenter, $X_1, \ldots, X_k$ are the independent variables (factors) of the experiment, k is the number of factors and ε (residual) accounts for the sources of variability that are not represented by f. It is assumed that ε is a statistical error, described by a normal distribution with mean zero

and variance σ^2 [72].

For this analysis, the independent variables $X_1, \ldots, X_k$ are the values of the Yeoh coefficients defined in the numerical model, η is the measure of performance describing the fit between the experimental force-displacement curve and the numerical simulation of the quasi-static behaviour of the resilient mount, that will be presented in Section 2.1.1.10. The predictive model obtained by the RSM analysis provides an estimate of the unknown function f, relating the values of the Yeoh coefficients to the global fitting performance of the numerical model.

The goal of the analysis is to find the optimal values of the Yeoh coefficients, i.e. the set of values providing the highest value of the performance measure function.

This can be done by following a five-stage procedure, described in [10]. The first stage consists in the determination of the factors of the experiment and their levels. In the second stage, the researcher selects the appropriate experimental design, creates the table of design and performs the experiments accordingly. Later, a mathematical model is created through the fit of a polynomial function. In the fourth stage, the model's fitness and the underlying assumptions are checked. Finally, the optimum values of the design variables are determined.

These stages are discussed in Sections 2.1.1.5 to 2.1.1.9, focusing on the present study.

2.1.1.5 Definition of the factors of the design

The first step of the analysis consists in the definition of the factors of the experiment and their levels. This choice defines the design space, where the response will be analyzed. The

choice of factors and the definition of their range is a crucial phase of the design, and it has an important effect on the accuracy and the success of the optimization process [5]. In fact, if the selected levels are too close, there will not be enough variation in the response to accurately fit the model. Vice versa, levels too far apart will give poor values of the response, that may not be different enough from each other [43].

As stated before, in this study the factors of the experiment are the values of the Yeoh coefficients of the numerical model that simulates the compression of the resilient mounting element.

The actual values of the variables X_i are converted into the coded variables x_i, introduced in Table 3.1, using the following relationship:

$$x_i = \frac{X_i - \frac{X_{max}+X_{min}}{2}}{\frac{X_{max}-X_{min}}{2}} \tag{2.5}$$

This way, it is possible to gauge the relative size of the effects, which leads to a better estimate of their importance in the design [67].

2.1.1.6 Choice of the experimental design

The goal of this stage of analysis is to create a predictive empirical model, called response surface model, of the response of the system, corresponding to an approximation of the unknown function f of Equation (2.4). Generally, f is represented using a first-order or second-order polynomial model [72].

In this study, the function f is represented using a quadratic model, having the form

$$\xi = \beta_0 + \sum_{i=1}^{k} \beta_i x_i + \sum_{i=1}^{k} \beta_{ii} x_i^2 + \sum_{1 \leq i \leq j}^{k} \beta_{ij} x_i x_j + \varepsilon \tag{2.6}$$

As stated by Myers et al. in [72], the quadratic model presented in Equation (2.6) is the most suitable model to represent the response behaviour of a large variety of experimental problems because it's flexible (as it can represent the behavior of a large group of functions) and easy to calculate (as the coefficients of the model can be estimated by least square regression).

The quadratic model is fitted using a Central Composite Design (CCD). This design, introduced by Box and Wilson in [12], is the most widely used in the field of RSM because of the low number of experiments needed to create the model and the fact that it can be obtained by expanding a factorial design [67].

CCD is composed of a full factorial or fractional factorial two-level design (having respectively $n_F = 2^k$ or $n_F = 2^{k-p}$ points), a set of $2k$ star points at a distance α (in coded values) from the center of the design and a center point (possibly replicated multiple times). The total number of runs of the design is, therefore, equal to $n_F + 2k + c_p$, where c_p is the number of replicates of the center points.

Each factor is evaluated at the levels $-\alpha$, -1, 0, $+1$, $+\alpha$.

In the special case of rotatable CCD (i.e. if the variance of the predicted response is the same at all points at the same distance from the design center), the value of α is given by the formula $\alpha = n_F^{1/4}$ [67].

2.1.1.7 Mathematical-statistical treatment of data

After acquiring the data related to each experimental point of the design selected in Section 2.1.1.6, it is necessary to fit a mathematical equation to describe the behaviour of the response according to the levels of the factors.

The coefficients of the predictive equation are estimated using the method of least squares (MLS). This method, implemented in the software for statistical analysis, minimizes the sum of squares of the residuals, introduced in Equation (2.4). In order to do so, it is necessary to make the assumption that the residuals follow a random distribution with zero mean and unknown variance σ^2 [5].

In this research activity, Design-Expert 10® is used to create the equation of the predictive model via MLS.

2.1.1.8 Evaluation of the fitted model

The fitting equation calculated using the procedure described in Section 2.1.1.7 may not be an accurate representation of the response determined experimentally.

Therefore, ANOVA is performed to evaluate the quality of the predictive model. The central idea of ANOVA, thoroughly described in [10], is to compare the variation due to the treatment (change in the combination of variable levels) with the variation due to random errors.

This comparison is performed by means of the Fisher distribution (F test). This way, it is possible to evaluate the significance of the regression used to foresee responses considering

the sources of experimental variance.

The F-values are calculated by constructing the ANOVA table of the design and compared to the tabled F-values at the desired confidence level. The outcome of this comparison can be expressed by means of the related P-value, describing the significance of every effect.

Further information about the overall predictive capability of the model can be acquired by the analysis of the coefficient of determination R^2, that measures the amount of the reduction in the variability of response obtained by using the regressor variables of the model [5]. Similarly, the coefficient Adjusted R^2 provides a statistic adjusted for the number of factors in the model [67].

Moreover, it is necessary to test the underlying assumptions of ANOVA, by analyzing the distribution of the residuals and the observed values. These assumptions, discussed in [67], are:

1. the residuals follow a normal distribution;

2. the values of the observations are independent;

3. the residuals are structureless.

In this research activity, these assumptions are verified through visual inspection of the distribution of the residuals. Because of the nature of the FE analysis, assumption $^{\#}2$ is implicitly true, as the result of every run of the finite element model is not affected by the order in which the runs are performed.

Finally, the fitting equation is validated by defining a set of validation points in the design space (not belonging to the table of the design), acquiring the experimental value of

the response in those points, and comparing it with the value predicted by the regression model [67].

2.1.1.9 Optimization

Finally, the critical points and global extrema of the predictive equation are determined, in order to find the optimal working condition of the experimental system. As the polynomial functions representing the response of the system are relatively easy to handle, minimum and maximum points are found using a combination of analytical, numerical and graphical techniques.

This stage represents a crucial part of this study, as the objective of the research is the determination of the optimal value of the coefficients of the Yeoh model. The optimal Yeoh coefficients are determined by calculating the value of the response equation over a fine grid of points, across the entire design space. Moreover, the analysis of the graphical representation of the response surface provides more information about the behaviour of the predictive model.

2.1.1.10 Performance measure

The experimental data acquired with the compression test are compared with the numerical results, obtained with the finite element model, by means of a performance measure.

The selected performance measure for the analysis is the Nash-Sutcliffe efficiency index. Introduced in [73], this coefficient is a normalized statistic that compares the relative magnitude of the residual variance to the experimental data variance [68].

It is defined as

$$E_f = 1 - \frac{\sum_{i=1}^{n} \left(y_i^{obs} - y_i^{sim}\right)^2}{\sum_{i=1}^{n} \left(y_i^{obs} - \overline{y^{obs}}\right)^2} \tag{2.7}$$

where y_i^{obs} and y_i^{sim} are the i-th values of the dependent variable y observed in the experiment and calculated by the model, respectively; $\overline{y^{obs}}$ is the mean of the observed data and n is the sample size.

The denominator of Equation (2.7) is the sum of the squared differences between the observed values and the mean observed value. It represents the total variation of the dependent variable y that can be explained by the predictive model.

The numerator of Equation (2.7) is the sum of the squared differences between the observed and the predicted values of the dependent variable y. This term represents the variation in the observed data that has not been explained by the predictive model.

E_f can assume values in the interval $(-\infty, 1]$, with higher values indicating better agreement. The paper [68] considers $E_f \in [0, 1]$ an acceptable level of performance for the predictive model. If $E_f < 0$, the sum of the squared differences between the observed and the predicted values of the dependent variable is greater than the sum of the squared differences between the observed values and the mean observed value. Therefore, the computed predictive model should be discarded and the mean of the observed values should be used as predictive model instead [55].

2.1.2. Dynamic characterization

2.1.2.1 Overview

The methodology for the dynamic characterization of resilient mounting elements is represented in Figure 2.7.

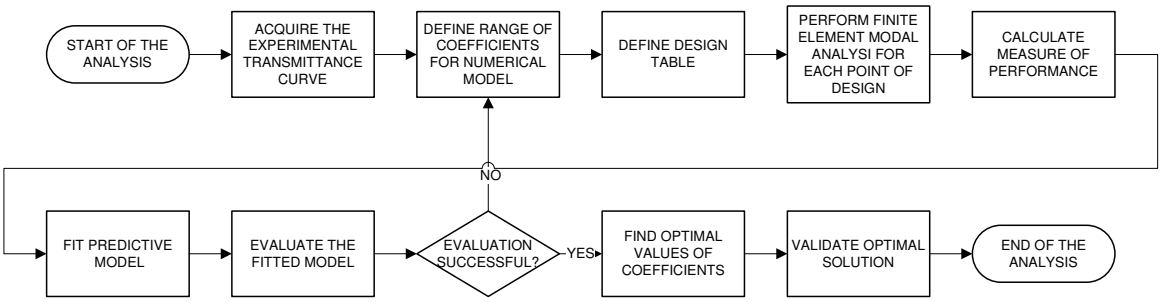

Figure 2.7: Visual representation of the methodology followed in this study for the dynamic characterization of resilient mounting elements

First, the experimental transmittance curve is acquired. The component under test is placed in a testing structure, designed to decouple the element from the structure frame, and subjected to a uniform level of excitation over a predefined frequency range. Vibration levels are measured on the top and bottom surfaces of the isolator. The ratio between the measured levels of excitation defines the experimental transmittance curve. The experimental test procedure is presented in Section 2.1.2.3.

Then, a finite-element model is built, in order to perform the modal analysis of the resilient mount. The results of the quasi-static characterization of the isolator under test are used to define the constitutive relationship for the rubber material of the isolator. For this work, the mechanical behaviour of the rubber material is represented using the Yeoh model, presented in [105]. The paper [35] discusses how the hyperelastic coefficients of the Yeoh

model were calculated. The numerical model is described in Section 2.1.2.5.

It is necessary to estimate the optimal value of the dynamic coefficients of the finite-element model. In this work, the dynamic behaviour of the resilient mount is estimated by varying the frequency-dependent damping ratios. To do this, a range of variation is assigned to each factor of the analysis. Using DOE, a set of designs, having different sets of the dynamic coefficients is created (design table). These sets of coefficients are tested in the numerical model.

For each run, a measure of performance is calculated (presented in Section 2.1.2.6), to estimate the fitting performance of the combination of factors of the simulation. In this work, the sum of the squared log-scaled differences between numerical and experimental data, presented in [91], is used.

With these data, a statistical predictive model is built, relating the values of the factors to the expected fitting performance. The predictive model so defined is evaluated performing a set of validation runs.

If the validation is successful, an optimization procedure is performed to calculate the values of the dynamic coefficients yielding the maximum value of the measure of performance. Then, the optimal set of dynamic coefficients is tested in the dynamic model.

2.1.2.2 The four-pole parametric representation of the dynamics of vibration isolators

Each component of a noise transfer path needs to be characterized with a relationship between the vibrations on the input and output surface of the element.

This is generally done through the use of the four-pole parameter model, presented in

[66], that defines a linear relation for the performance equations of an elastic system:

$$\begin{cases} F_1 = Z_{11}F_2 + Z_{12}V_2 \\ V_1 = Z_{21}F_2 + Z_{22}V_2 \end{cases} \tag{2.8}$$

or, in matrix notation:

$$\vec{F} = [Z]\vec{V} \tag{2.9}$$

In the system (2.8) force and velocity at the input point (denoted by the index 1) are expressed as a function of force and velocity at the output point (denoted by the index 2).

The representation of a vibration isolator can be reduced to the analysis of a massless spring, since the mass of the resilient mount is negligible when compared to the masses of the inertial elements composing the test rig (described in Section 2.1.2.3).

The total response of the resilient mounting element is calculated by considering 6 degrees of freedom (3 translational directions and 3 rotational directions), and representing the dynamics of the system along each direction using Equation (2.9).

Generally, the energy transmitted along the vertical direction is considerably higher than the other degrees of freedom [71]. For this reason, in this analysis, only the vertical component of the dynamics of the system is considered.

Following the procedure defined in the ISO Standard [28], the force at the receiving point (F_r) can be estimated using the formula

$$F_r \cong Z_{21}v_s = k_{21}u_s \tag{2.10}$$

where k_{21} is the transfer stiffness of the resilient mounting element and u_s is the displacement at the source point.

This equation is related to the transmittance function $\frac{a_2}{a_1}$ by the equation [71]

$$k_{21} \cong \frac{F_2}{u_1} = -(2\pi f)^2 m_2 \frac{u_2}{u_1} = -(2\pi f)^2 m_2 \left(\frac{a_2}{a_1}\right) \tag{2.11}$$

where m_2 is the mass of the receiving structure and u_1 and u_2 are the displacements at the two interfaces of the component.

Therefore, using this procedure, the ratio $\frac{a_2}{a_1}$, measured with the dynamic tests described in Section 2.1.2.3 can be used to estimate the isolator performance in a given frequency range.

2.1.2.3 Measurement of the transmissibility curve

I acquired the experimental data at the Ship Noise and Vibration Laboratory (NVL) of the University of Trieste (Italy) in 2018.

Two resilient mounts are tested: a simple cylindrical element, having a maximum static load of 36 kN, and an isolator with a more complex geometry, composed of a conical rubber ring constrained between two steel cups. The maximum static load for this element is 145 kN. The isolators are shown in Figure 2.8. The test rig developed to characterize the resilient mounts is shown in Figure 2.9.

The isolator under test, placed between the excitation mass and the blocking mass is excited with an electrodynamic shaker, which generates a uniform level of acceleration

(a) Cylindrical mount

(b) Conical mount

Figure 2.8: Resilient mounts tested in the activity (figures not in scale)

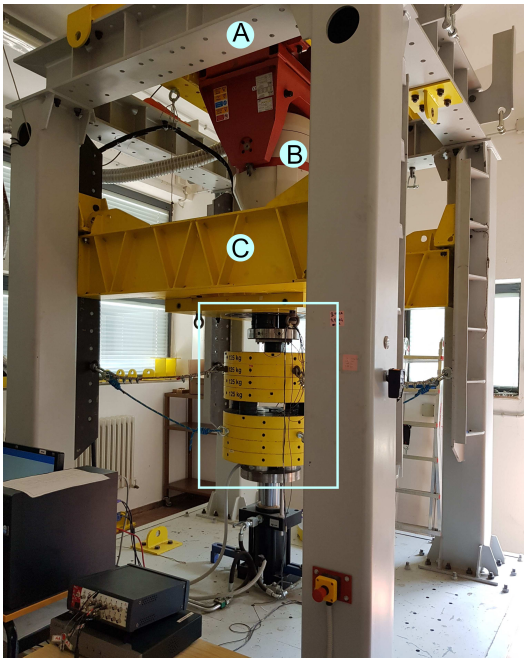

(a) Photograph of the test rig

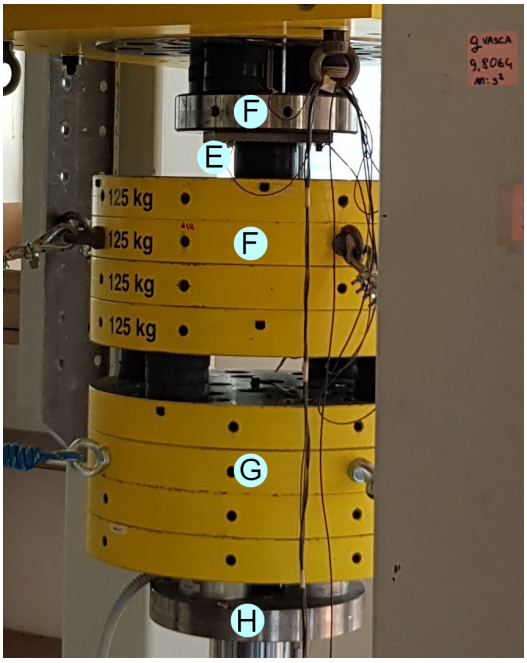

(b) Closeup on the masses of the test rig shown in (a)

Figure 2.9: Test rig for vibration testing in Ship Noise and Vibration Laboratory (NVL) of the University of Trieste. Elements of the test rig:

A. shaker support frame;
B. electrodynamic shaker;
C. pre-load support frame;
D. excitation mass;
E. test isolator;
F. blocking mass;
G. seismic mass;
H. cylinder for hydraulic preload.

on the excitation mass in the frequency range 50-1000 Hz.The excitation is regulated by a closed-loop control on the vertical acceleration levels measured on the excitation mass. A static preload is applied using a hydraulic piston.

Piezoelectric transducers are used to measure the levels of acceleration on the excitation and blocking mass. To validate the assumptions of this experimental procedure, acceleration levels are measured also at the rim of the excitation mass in the radial and transversal direction.

Further detail on the experimental procedure is given in [33].

2.1.2.4 Verification of the requirements for the experimental determination of the mechanical mobility

The standard [28] defines a set of conditions that have to be met in order to consider the measured data valid in the frequency range of analysis. These assumptions were checked as the experimental measurement of the dynamic properties of the isolators was performed.

2.1.2.4.1 Assumption of linearity

The test for linearity is needed to validate the assumption that the the amplitude of the vibration of the isolator is approximately proportional to the input excitation levels. The test is performed by exciting the system with excitation spectra of different amplitude (a difference of at least 10 dB is prescribed) and checking that the signals of the measured frequency response functions are within 1.5 dB between each other.

2.1.2.4.2 Low input vibrations

In order to avoid the presence of unwanted acceleration in directions other than that of the excitation, the acceleration of the excitation mass in the vertical direction has to be compared with the acceleration levels measured in other directions. This is done by measuring the acceleration levels on the outer surface of the excitation mass in the vertical, tangential and radial direction. In accordance with the ISO Standard, normal excitation is measured on the central axis of the excitation mass, and transverse excitation is measured on the lateral surface.

The ISO Standard prescribes a difference of at least 15 dB between the vibration levels measured in the direction of excitation ($L_{a,excitation}$) and the other directions ($L_{a,unwanted}$):

$$L_{a,excitation} - L_{a,unwanted} \geq 15\,\text{dB} \tag{2.12}$$

2.1.2.4.3 Analysis of resonance conditions using Operational Deflection Shapes (ODS)

Operational Deflection Shapes Analysis (ODS) is used to characterize the resonance conditions observed in the measurement of the transmissibility function. The acceleration signal measured on the axis of the excitation mass is used as a reference, and vibration levels are measured in 8 positions: 4 measurement points are placed on the circumference of the excitation mass, and 4 are placed on the circumference of the blocking mass. This way, it is possible to to calculate amplitude and phase of the relative displacement calculated in the 8 measurement point, and create a visual representation of the deflection of the system where an increase in the vibration levels is measured [26, 56].

2.1.2.5 Numerical analysis of the modal behaviour of the resilient mounting element

The experimental methodology discussed in Section 2.1.2.3 is represented in a numerical model for finite-element simulations. LS-DYNA® is used to perform the analysis.

The geometry of the isolators used in the analysis is shown in Figure 2.10. The optimal size of the mesh was estimated with a mesh convergence analysis.

As discussed in Section 2.1.2.3, a closed-loop control generates a uniform level of acceleration in the frequency range 50-1000 Hz. This condition is represented in the numerical simulation with a fixed boundary condition on the upper surface of the isolator and a base acceleration excitation. As the blocking mass moves coincidentally with the bottom part of the isolator, it needs to be represented in the numerical model.

Following the guidelines of the ISO Standard, the stiffness of the connection between the blocking mass and the frame of the test rig is assumed to be significantly lower than the isolator's. It was observed in the comparison of the measurements performed on the cylindrical mount with the results of the numerical simulation that both sets of data showed a resonance peak in the low-frequency range, but the position of the peak was significantly different between the two sets of data. This led to assume that the difference was caused by the effect of the stiffness of the resilient mount connecting the blocking mass to the rest of the structure. To correct the numerical model in order to take into account this effect, an additional point spring is added on the bottom of the blocking mass. The stiffness of this spring is calculated using a 1-degree-of-freedom approximation of the system under analysis, by matching the position of the peak measured experimentally (48 Hz).

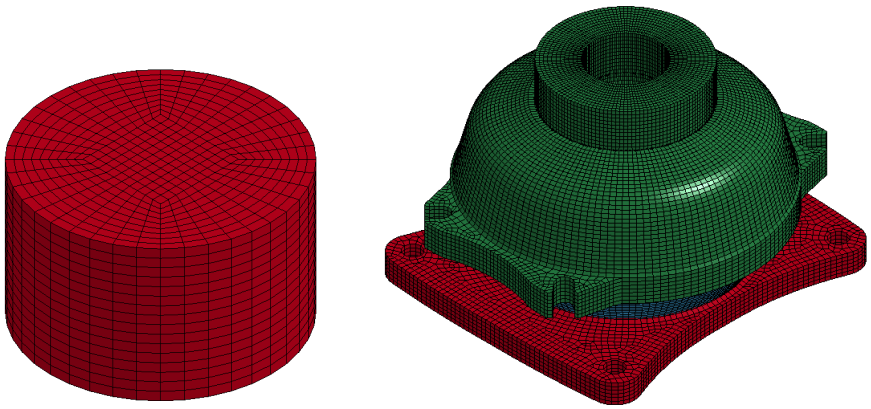

(a) Cylindrical mount (b) Conical mount

Figure 2.10: Geometry of the isolators under analysis

The blocking mass is expected to deform significantly less than the resilient mount. Therefore, it is modeled with a more coarse mesh.

The steel material is represented using a linear elastic constitutive relation, and a hyper-elastic Yeoh model is used to represent the rubber material, as described in Section 2.1.1.1.

The mechanical properties of the two resilient mounts are shown in Table 2.3.

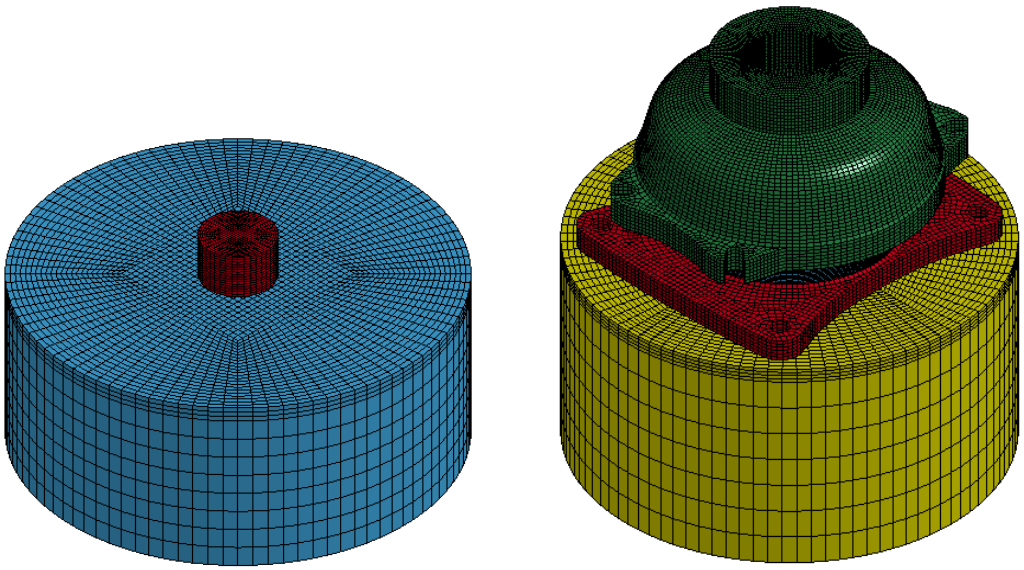

(a) Cylindrical mount (b) Conical mount

Figure 2.11: Geometry of the finite element model used in the modal analysis

Table 2.3: Material properties of the finite-element model for dynamic analysis

(a) Rubber - cylindrical mount

Property	Value
Mass density	$1050\,\mathrm{kg/m^3}$
Poisson's ratio	0.4998
Yeoh coefficients:	
C_{10}	2 504 000 Pa
C_{20}	101 700 Pa
C_{30}	2 695 000 Pa

(b) Rubber - conical mount

Property	Value
Mass density	$1050\,\mathrm{kg/m^3}$
Poisson's ratio	0.4998
Yeoh coefficients:	
C_{10}	846 480 Pa
C_{20}	79 350 Pa
C_{30}	250 000 Pa

(c) Steel

Property	Value
Mass density	$7850\,\mathrm{kg/m^3}$
Young's modulus	2.000×10^{11} Pa
Poisson's ratio	0.3

2.1.2.6 Evaluation of the fitting performance

In order to optimize the fit of the numerical simulation to the experimental data, it is necessary to define a measure of performance. This coefficient is used to build a statistical predictive model, relating the values of the factors of the analysis (the frequency-dependent modal damping ratios) to the expected fitting performance.

This is done by minimizing the square difference between the decibel-transformed experimental and numerical transmissibility functions:

$$\lambda_{\mathrm{dB}} = \sum_{m=1}^{M} \left| A_{\mathrm{dB}}\left(\omega_m\right) - X_{\mathrm{dB}}\left(\omega_m\right) \right|^2 \tag{2.13}$$

where $A_{\mathrm{dB}}\left(\omega_m\right)$ and $X_{\mathrm{dB}}\left(\omega_m\right)$ are the values of the measured and simulated frequency response functions, respectively, evaluated in the M frequency lines where the transmissibility functions are defined.

This measure of performance is selected because of the good results shown in [91] for the analysis of log-transformed response functions.

2.1.2.7 Analysis of the simulated transmissibility response function in relation to the preload applied to the resilient mount

A primary feature of rubber materials is the fact that their dynamic properties are a function of the state of stress of the material [38]: the magnitude of the stiffness and the damping characteristics of the material are both strongly related to the frequency at which the system

is excited [92].

For this reason, in this study, I analyze how the shape of the frequency response function simulated using the numerical model changes for different values of the static preload applied to the resilient mounting element. The preload ranges from 0 to the maximum design load. This provides an estimate of the variation of the dynamic properties of the isolator, highlighting the effect of the engine load on the position of the resonance frequency of the resilient mount.

2.2. Transfer path of underwater sound transmission

The mathematical formulation of the transfer path analysis of the underwater radiation of structure-borne noise generated by resiliently mounted on-board machinery is presented in Sections 2.2.1 to 2.2.4. The experimental setup for the measurement of underwater radiated noise is described in Section 2.2.5, and the experimental setup is presented in Section 2.2.6. The reliability of the sound pressure measurements is discussed in Section 2.2.7. The Finite Element model of the dynamic response of the test rig is presented in Section 2.2.8.

2.2.1. Transfer path analysis of the engine foundation

Using transfer path analysis, it is possible to represent the vibration levels at the receiving point as the combination of the source's velocity levels and the vibrational path's transfer components.

This method is used in [58] and [69] in the analysis of structure-borne noise produced

by marine diesel engines (Figure 2.12) to represent velocity levels on the top plate of the foundation ($L_{v,\mathrm{f}}$ [dB re: $1 \times 10^{-9}\,\mathrm{m\,s^{-1}}$]) as a composition of source velocity levels ($L_{v,\mathrm{s}}$ [dB re: $1 \times 10^{-9}\,\mathrm{m\,s^{-1}}$]), resilient mounting mechanical impedance levels ($L_{Z,21}$ [dB re: $1\,\mathrm{N\,s\,m^{-1}}$]), and foundation mobility levels ($L_{M,\mathrm{f}}$ [dB re: $1\,\mathrm{m\,s^{-1}\,N^{-1}}$]):

$$L_{v,\mathrm{f}} = L_{v,\mathrm{s}} + L_{Z,21} + L_{M,\mathrm{f}} \tag{2.14}$$

The quantities of Equation (2.14) are frequency-dependent (ω). In the rest of this Chapter, the relation of the spectral quantities with ω will be omitted.

In [69] the term $L_{M,\mathrm{f}}$ was calculated using the effective mobility of the foundation, defined in [80], in order to consider the energy transferred in all directions.

In Equation (2.14), Z_{21} is the resilient mount impedance function, defined by Equation (2.15):

$$Z_{2,1} = \frac{F_2}{V_1} \tag{2.15}$$

where F_2 is the force transmitted through the rubber mount to the receiving structure, and V_1 is the velocity measured on the top surface of the resilient mount. In this case, $F_2 = F_{\mathrm{f}}$ and $V_1 = V_{\mathrm{s}}$, where F_{f} is the force transmitted to the top plate of the foundation. M_f is the mobility function of the diesel engine foundation, which relates force levels on the top of the foundation and velocity levels on the top plate.

From $L_{v,\mathrm{f}}$, the velocity levels of the base plate $L_{v,\mathrm{b}}$ can be calculated by combining the transfer mobility function calculated between the foundation and the foundation plate and

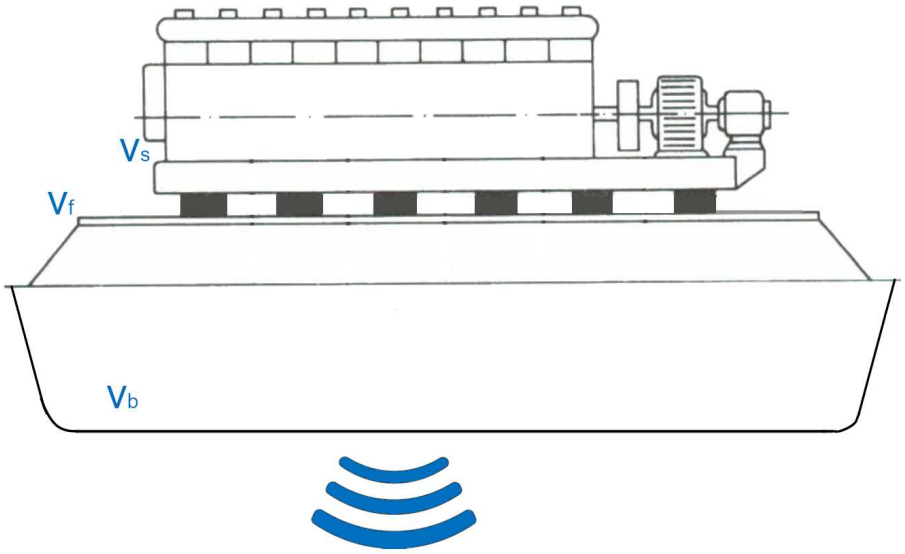

Figure 2.12: Velocity measurement points of engine (v_s), foundation (v_f), and base plate (v_b) (original image from [82])

the direct impedance function of the foundation. We have that:

$$v_b = v_f \cdot \frac{v_b}{v_f} = v_f \cdot \frac{v_b}{F_f} \cdot \frac{F_f}{v_f} \tag{2.16}$$

where v_b/F_f is the mechanical transfer mobility function calculated as the ratio between the velocity of the base plate v_b resulting from a force applied to the foundation F_f, and F_f/v_f is the mechanical impedance of the foundation that relates the amplitude of the force on top of the foundation to the velocity v_f measured at the same point where the force was applied.

Therefore, converting to levels:

$$L_{v,b} = L_{v,f} + L_{M,b,f} + L_{Z,f} \tag{2.17}$$

where $L_{M,b,f}$ is the transfer mechanical mobility level between the foundation plate (index

f) and the base plate (index b), and $L_{Z,\mathrm{f}}$ is the mechanical impedance level of the foundation of Equation (2.14).

Combining Equation (2.14) and Equation (2.17) we get:

$$L_{v,\mathrm{b}} = L_{v,\mathrm{s}} + L_{Z,21} + L_{M,\mathrm{f}} + L_{M,\mathrm{b,f}} + L_{Z,\mathrm{f}} \tag{2.18}$$

Equation (2.18) can be rewritten as

$$L_{v,\mathrm{b}} = L_{v,\mathrm{s}} + L_{Z,21} + L_{M,\mathrm{b,f}} \tag{2.19}$$

since

$$\frac{v_{\mathrm{f}}}{F_{\mathrm{f}}} \cdot \frac{F_{\mathrm{f}}}{v_{\mathrm{f}}} = 1 \tag{2.20}$$

In order to calculate the underwater sound pressure levels radiated from the vibrating base plate we need to add to Equation (2.19) the contribution of the radiation of the noise through the water medium. This is done by relating the velocity levels on the radiating surface to the radiating power of the source using the expression of the coefficient of sound radiation efficiency (Section 2.2.2).

2.2.2. Sound radiation efficiency

Oppenheimer and Dubowsky [77] define the sound radiation efficiency σ as the ratio between the power radiated from the structure under test and the amplitude of structural vibration on

the radiating surface:

$$\sigma = \frac{W}{\rho c S \overline{|v_{\mathrm{b}}|}^2 / 2} \tag{2.21}$$

where W is the power radiated from a structure with surface area S, density ρ and vibrating with the spatially-averaged mean-square velocity $\overline{|v_b|}^2$ [23].

Equation (2.21) can be expressed in logarithmic notation:

$$10 \log(\sigma) = L_W - L_{v,\mathrm{b}} - 10 \log\left(\frac{S}{S_{\mathrm{ref}}}\right) \tag{2.22}$$

where L_W is the sound power level in dB (re: 1×10^{-12} W), $L_{v,\mathrm{b}}$ is the velocity level of the surface, and S_{ref} is the reference surface (1 m^2).

2.2.3. Underwater acoustic power in the reverberant field

We can calculate the radiated sound pressure level L_p from the source sound power level L_W as follows [54]:

$$L_p = L_W - 20 \log(r) + \text{const.} \tag{2.23}$$

where the constant term is equal to

$$\text{const.} = 10 \log\left(\frac{W_{\mathrm{ref}} \rho c}{4\pi p_{\mathrm{ref}}^2}\right) \tag{2.24}$$

Equation (2.23) is found from the definition of sound intensity as a function of distance from the radiating source (r). For water, the reference values are $W_{\mathrm{ref}} = 6.76 \times 10^{-19}$ W/m^2,

$p_{\text{ref}} = 1 \times 10^{-6}\,\text{Pa}$, while density $\rho = 1000\,\text{kg/m}^3$ and sound speed $c = 1480\,\text{m s}^{-1}$. Therefore, the constant term of Equation (2.23) corresponds to

$$10\log\left(\frac{W_{\text{ref}}\rho c}{4\pi p_{\text{ref}}^2}\right) \approx -11\,\text{dB} \tag{2.25}$$

In the case of sound radiation in reverberant fields, the work [50] provides a formula to estimate the term W of Equation (2.21):

$$W = \frac{10^{\frac{SPL_{\text{rev}}}{10}} V}{1.58 \times 10^{20}\left(T_{60} - \frac{0.0373V}{A}\right)} \tag{2.26}$$

where SPL_{rev} is the sound pressure level of spatially averaged rms sound pressure due to reverberant field (re: $1 \times 10^{-6}\,\text{Pa}$), V is the volume of water in the tank, and A is the total surface area of tank boundaries. In this case, since all sound radiation happens in the reverberant field $\sigma \simeq \sigma_{\text{rev}}$.

2.2.4. Transfer path analysis of the underwater radiation of structure-borne noise

In order to estimate the sound pressure level at the receiving point underwater, we need to include the contribution of every component of the vibrational transfer path that connects the noise source to the underwater receiver.

Combining Equation (2.22) and Equation (2.23), we have:

$$L_p = L_{v,\text{b}} + 10\log(\sigma) + 10\log\frac{S}{S_{\text{ref}}} - 20\log(r) + \text{const.} \tag{2.27}$$

In order to include in this equation the noise levels generated by the source ($L_{v,\mathrm{s}}$ in Equation (2.14)), we need to relate $L_{v,\mathrm{b}}$ to the velocity levels measured on top of the foundation ($L_{v,\mathrm{f}}$ in Equation (2.14)).

Therefore, Equation (2.27) becomes:

$$L_p = L_{v,\mathrm{s}} + L_{Z,21} + L_{M,\mathrm{b,f}} + 10\log(\sigma) + 10\log\frac{S}{S_{\mathrm{ref}}} - 20\log(r) + \mathrm{const.} \tag{2.28}$$

The term $20\log(r)$ represents only sound propagation losses due to geometric spreading. By setting $r = 1$ m we obtain the underwater radiated noise level @ 1 m.

Equation (2.28) allows the designer to calculate the pressure levels measured by the underwater receiver as a composition of the velocity levels at the source (in this case, the marine diesel engine) and the transfer functions of the components of the transfer path. Each component of the transfer path is characterized separately, and then its contribution is added to the global equation of the transfer path.

2.2.5. Experimental setup

I developed an experimental setup to measure structural vibrations, transfer functions, and underwater sound pressure simultaneously and evaluate the terms of Equation (2.28). The experiments were performed in the deep tank of the Fluids & Hydraulics Laboratory, Faculty of Engineering and Applied Science, Memorial University of Newfoundland (Canada).

Figure 2.13 shows the mock-up designed and built to perform the vibration and underwater noise tests. The model reproduces the typical geometry of the foundation of a small

four-stroke diesel engine. Figure 2.14 shows the mock-up dimensions. The geometry of the foundations is made of four structural modules welded to a plate (1.40 m × 1.00 m, thickness 0.01 m), which hereinafter is referred to as the base plate. As shown in Figure 2.13, the mock-up is kept suspended using the overhead crane of the deep tank. Lifting slings are used to hang the metal structure on the crane hook. A loose rope prevents the axial rotation of the plate structure about the hanging point. During the tests, the base plate was kept in contact with the water so that the whole plate's surface was contributing to radiating noise. The deep tank is 3.65 m × 3.65 m × 3.65 m and is filled with fresh water, at a temperature of 14.6 °C.

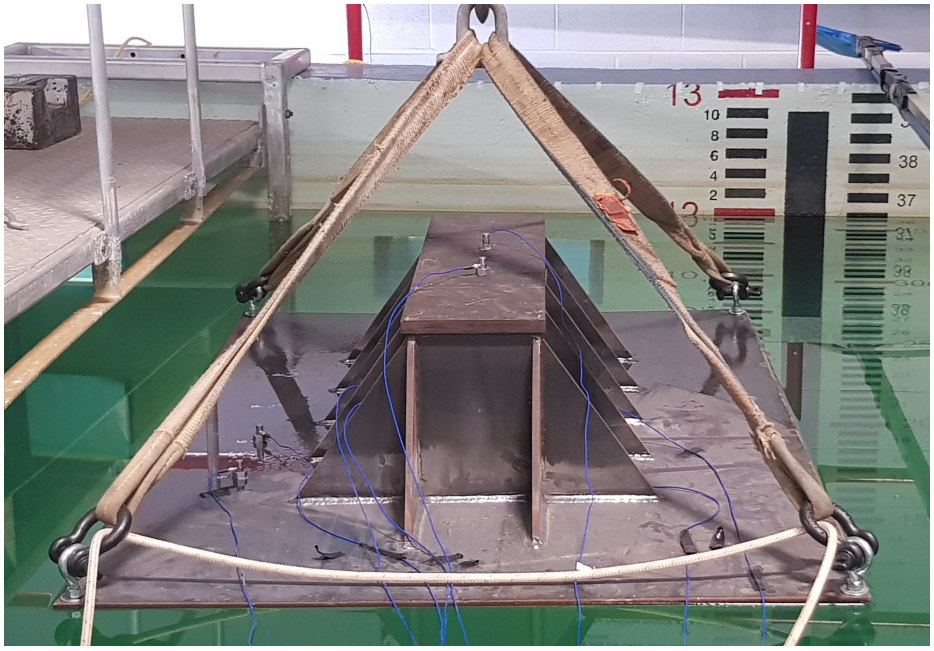

Figure 2.13: Plate and foundation used for the experimental tests of transfer path analysis suspended on water level

The transfer functions of Equation (2.28) are measured by applying input forces using an instrumented hammer and measuring the structural response using an array of accelerom-

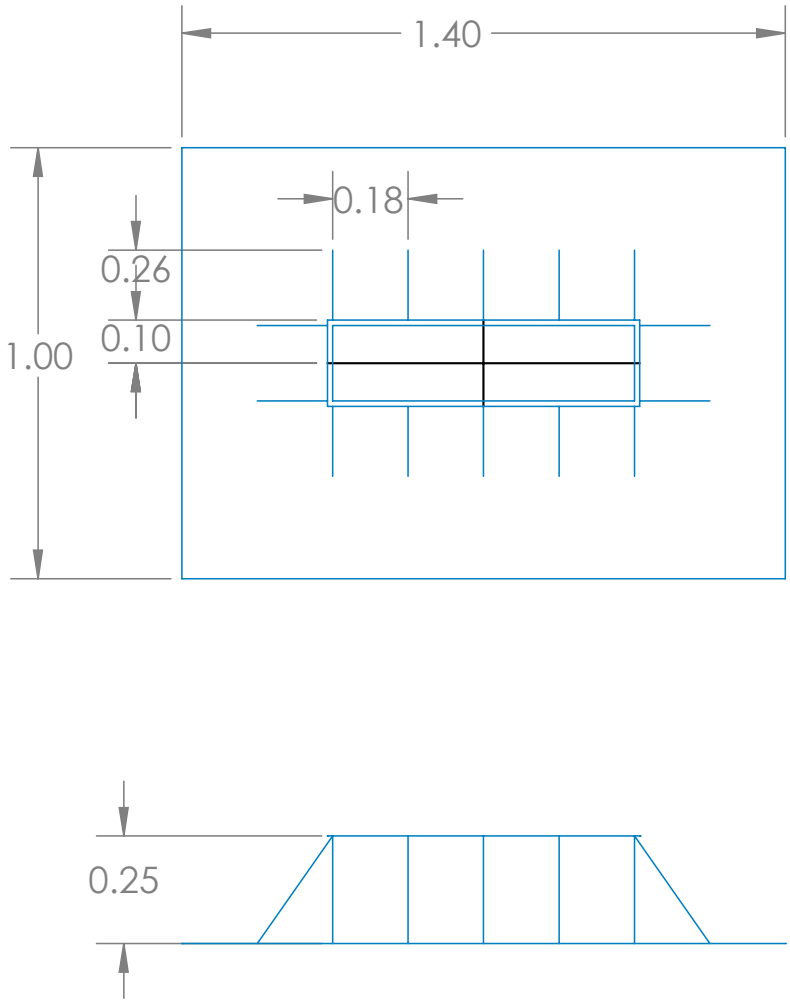

Figure 2.14: Geometry of the foundation mock-up (dimensions in meters)

eters placed on the test structure. The position of the accelerometers on the foundation mock-up model is shown in Figure 2.15. Underwater sound is measured with two hydrophones placed in the deep tank at the half-depth point. The absorption coefficient of the water tank used in this study was previously estimated in [46].

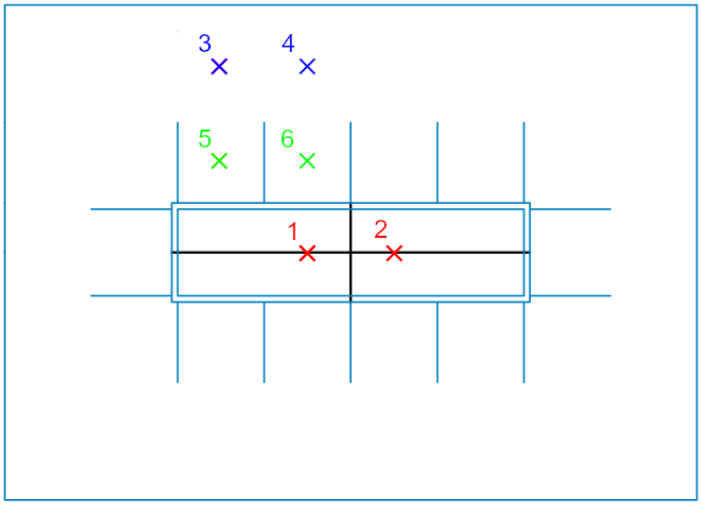

Figure 2.15: Foundation mock-up: measurement points of the acceleration signals.
1,2: points on the top plate, on the symmetry axis; 3,4: points on the base plate, 0.49 m distance from the symmetry axis; 5,6: points on the base plate, 0.23 m distance from the symmetry axis.

2.2.6. Description of the measurement system and signal processing

The structure under test is excited using a modal hammer PCB ICP® 086C03. Vibrations are acquired using uniaxial accelerometers PCB ICP® 352C33, and sound pressure is measured using Ocean Sonics icListen HF hydrophones. Signals are sampled at 8 kHz. Measurements were repeated three times for every testing condition, and the resulting frequency response functions (FRFs) were averaged. The consistency of FRFs across the performed tests was checked by calculating the FRFs' coherence, defined as

$$\gamma^2(f) = \frac{G_{x,y}(f)\, G^*_{x,y}(f)}{G_{x,x}(f)\, G_{y,y}(f)} \tag{2.29}$$

where $G_{x,x}(f)$ and $G_{x,y}(f)$ are the average auto-spectra of signals x and y, respectively, and $G_{x,y}(f)$ is the averaged cross-spectrum between x and y.

A Matlab script isolates the part of the force and acceleration signals in the proximity of the impact moment. The corresponding sections of the audio signal are extracted by taking the interval in the proximity of the peaks of the sound pressure signal. 200 samples are taken before the peak of the impact, and an interval of 1 s after. Figure 2.16 shows the parts of the sound pressure signal that are processed in the analysis, highlighted in blue.

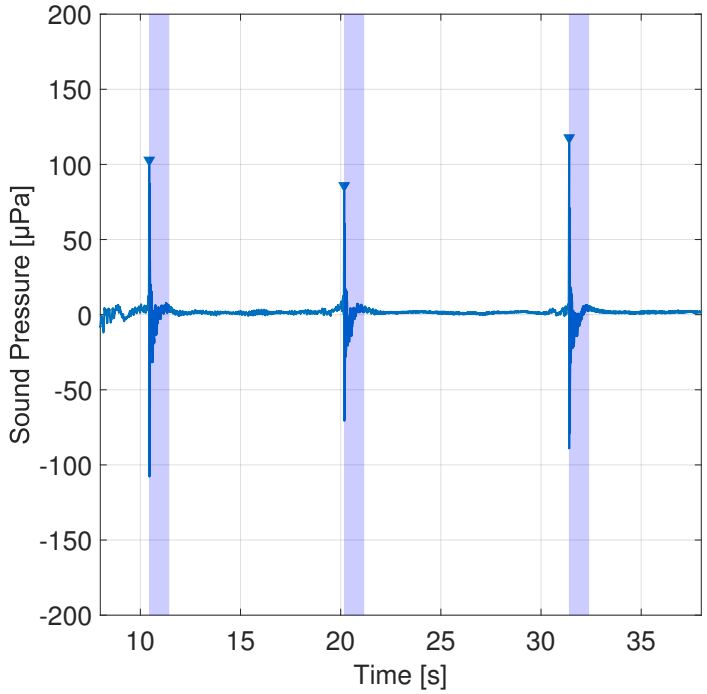

Figure 2.16: Selected intervals of the sound pressure signal, highlighted in blue

2.2.7. Reliability of sound pressure measurements in the reverberant field

The assumption of isotropic and reverberated field is valid only if the modal density in each frequency band satisfies an analytical criterion. The works [22, 48] provide comparable

formulations of this condition.

The ITTC guidelines [48] estimate the number of modes (N) in a frequency band of 1/3 octave bandwidth using the formula

$$N = \frac{\pi f^3 V}{c_0^3} \tag{2.30}$$

where f is the center frequency of each band, c_0 is the sound speed in the acoustic medium, and V is the tank's volume. The requirement of at least one mode for each frequency band yields a frequency threshold defined as

$$f \geq \sqrt{\frac{c_0^3 T_{60}}{4V \ln(10)}} \tag{2.31}$$

where T_{60} is the reverberation time in the tank.

Similarly, the work [22] states that in order to have at least N modes in the 3-dB bandwidth of one mode, f must satisfy the following condition:

$$N \frac{c_0^3}{4\pi f^2 V} \leq \frac{6}{\pi \log_{10}(e) T_{60}} \tag{2.32}$$

We take $N = 10$. The work [46] estimates an average value of 0.32 s for T_{60} for the tank used in this research activity. From Equation (2.32), the corresponding value of the threshold frequency is $f \geq 2.012 \times 10^3$ Hz.

2.2.8. Numerical model to represent the dynamic response of the plate and the foundation

A numerical simulation of a steel plate submerged in a water tank is conducted for the configuration shown in Figure 2.17. It involved creating the finite element model using Comsol Multiphysics® to model the underwater radiated sound of the plate. The simulation results were then analyzed to determine the sound pressure levels generated under impact excitation. The excitation is a unity impulse force applied to the center of the plate (plate model) or the center of the top surface of the foundation (foundation model).

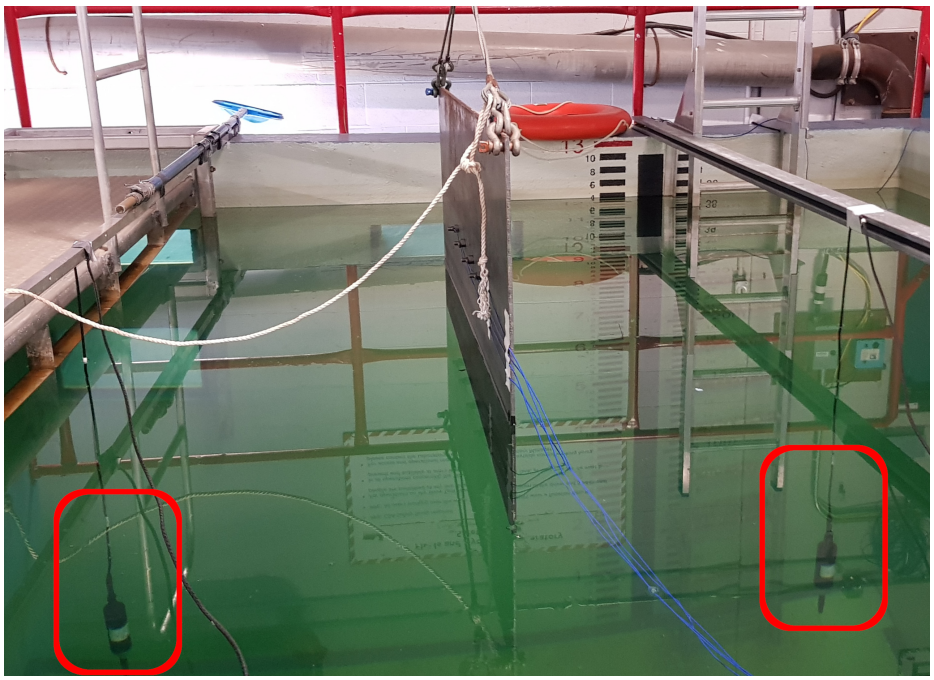

Figure 2.17: Vertical plate - experimental setup; hydrophones highlighted in red

A coupled acoustic-structural analysis of fluid with the steel structure was performed. The frequency-domain acoustical simulation allowed for the analysis of the response of the structure to different frequencies of acoustic waves. The Comsol Acoustic-Structure

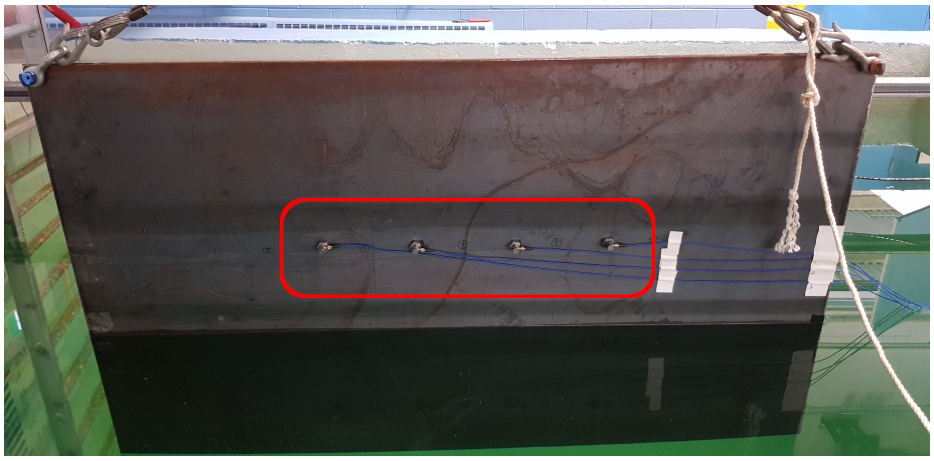

Figure 2.18: Vertical plate - accelerometers arrangement highlighted in red

Table 2.4: Material properties of the finite-element model for underwater sound radiation

(a) Steel

Property	Value
Mass density	$7850\,\mathrm{kg/m^3}$
Young's modulus	$2.000 \times 10^{11}\,\mathrm{Pa}$
Poisson's ratio	0.3

(b) Water

Property	Value
Mass density	$1000\,\mathrm{kg/m^3}$
Speed of sound	$1480\,\mathrm{m\,s^{-1}}$

Boundary coupling model is used, which provides a set of elements for modelling the fluid medium and interface conditions to couple these acoustic elements to a structure model [39].

The material properties used to define water and steel are presented in Table 2.4.

The water domain in the tank is represented using tetrahedral elements, with a maximum element size of 0.2 m. This mesh was used in [46] using the ray-tracing method to estimate the absorption coefficient of the water tank from estimating the tank's reverberation time. The steel structure is represented using tetrahedral elements as well, with a maximum element size of 0.1 m. The optimal size of the mesh elements was determined with a mesh sensitivity analysis. The mesh of the model in the two testing conditions is shown in

Table 2.5: Frequency-dependent overall absorption coefficient of the water tank [46]

f	α	f	α
0	0	1600	0.1112
400	0.025	2000	0.1256
500	0.03	2500	0.0827
630	0.0613	3150	0.0802
800	0.0654	4000	0.1036
1000	0.0703	5000	0.1135
1250	0.069		

Figures 2.19 and 2.20.

Sound pressure is measured in 10 points placed around the position of each hydrophone in the experimental setup. Sound pressure levels are calculated and averaged across the 10 measurement points. This way, it is possible to avoid the effect of acoustic anti-nodes in estimating the sound pressure level [106].

The frequency-dependent absorption coefficients of the water tank (α) were calculated in [46] in the frequency range 0-5000 Hz, and are presented in Table 2.5. These are overall values that include the contribution of the lateral walls, the bottom surface of the tank, and the air-water interface surface.

Before performing the coupled acoustic-structure analysis, it was necessary to determine the damping of the steel plate. Using the numerical model of the plate's dynamic response, the structure's damping values are estimated across different frequency ranges. The simulation is developed for the plate in the air for several values of damping. The isotropic loss factor (η) is selected to describe the structural damping of the plate. The loss factor is a way to describe the damping of a material, which is a measure of its ability to dissipate

energy when subjected to mechanical stress. It is a relative measure of damping capacity and is proportional to the damping loss factor [17, 42]. Also, it is important to use a global damping value for the simulation to make realistic predictions of the damping behavior of structures [107].

The optimal loss factor values are found by fitting the numerical accelerance transfer function curves to the experimental behaviour. The values of η are used in the foundation's FE model to estimate the mock-up structure's radiation efficiency.

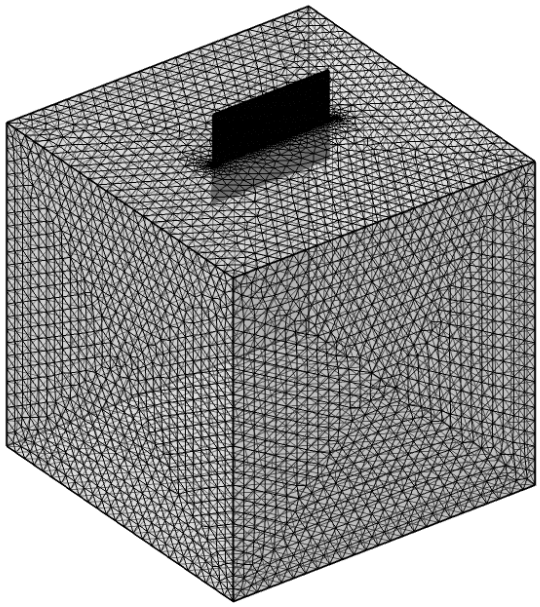

Figure 2.19: Mesh of the finite element model of the plate immersed in water and the deep tank water domain

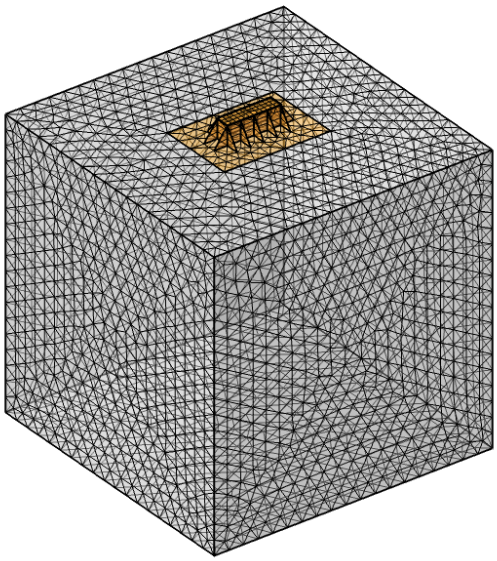

Figure 2.20: Mesh of the finite element model of the foundation mock-up suspended at water level and the deep tank water domain

Chapter 3

Results

Section 3.1.1 was adapted from the paper [35], Section 3.1.2 was adapted from the papers [32, 33, 34], Section 3.2 was adapted from the paper [31].

3.1. Characterization of the resilient mount

3.1.1. Static characterization

The results presented in this Section refer to the conical resilient mount shown in Figure 2.2.

3.1.1.1 Definition of the factors of the design

The factors of the experimental design and the corresponding coded values are shown in Table 3.1. The range of each factor was estimated with preliminary test experiments. The selection of variable levels is based on the results of previous studies on similar rubber materials [9, 71, 84].

Table 3.1: Factors of the experimental design for the static characterization of the resilient mount

Factor	Units	Range and coded levels			Coded variable
		−1	0	+1	
C_{10}	Pa	700 000	850 000	1 000 000	A
C_{20}	Pa	0	125 000	250 000	B
C_{30}	Pa	0	125 000	250 000	C

3.1.1.2 Choice of the experimental design

For the reasons stated in Section 2.1.1.6, the selected design is a three-factor rotatable central composite design (CCD) [67], having 8 factorial points (labeled #01–08 in Table 3.2, corresponding to the points of a 2^3 factorial design), 6 star points (#09–14) and one center point (#15). Only one center point is needed thanks to the deterministic nature of this computer experiment.

This design is represented in Figure 3.1.

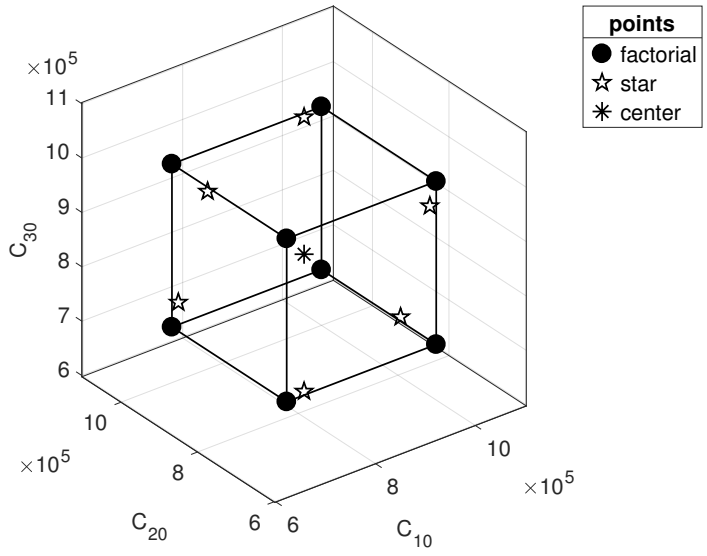

Figure 3.1: Points of the design of the static characterization of the resilient mount

The value of α is determined using the formula presented in Section 2.1.1.6.

Table 3.2 summarizes the outcome of the simulations performed using the numerical model described in Section 2.1.1.3, using the sets of Yeoh coefficients defined by the DOE procedure. The computed Nash-Sutcliffe efficiency results are calculated using Equation (2.7). The runs are sorted in standard order.

A graphical comparison between the experimental force-displacement curve and the results of the FE simulation is shown in Figure 3.2 for every run of the design. The values of the Nash-Sutcliffe efficiency are calculated by using Equation (2.7), comparing the numerical and experimental values of the force at every deformation step.

Table 3.2: Table of designs and results of the FEM analysis of the static characterization of the resilient mount

#	C_{10} [Pa]	C_{20} [Pa]	C_{30} [Pa]	E_f
01	700 000	0	0	0.814 637 143
02	1 000 000	0	0	0.966 270 463
03	700 000	250 000	0	0.945 452 823
04	1 000 000	250 000	0	0.871 025 476
05	700 000	0	250 000	0.878 633 680
06	1 000 000	0	250 000	0.939 516 197
07	700 000	250 000	250 000	0.969 810 594
08	1 000 000	250 000	250 000	0.813 008 913
09	597 731.0754	125 000	125 000	0.757 775 064
10	1 102 268.9254	125 000	125 000	0.746 775 452
11	850 000	−85 224.103 81	125 000	0.970 590 330
12	850 000	335 224.103 81	125 000	0.970 611 059
13	850 000	125 000	−85 224.103 81	0.993 491 963
14	850 000	125 000	335 224.103 81	0.994 788 807
15	850 000	125 000	125 000	0.999 667 319

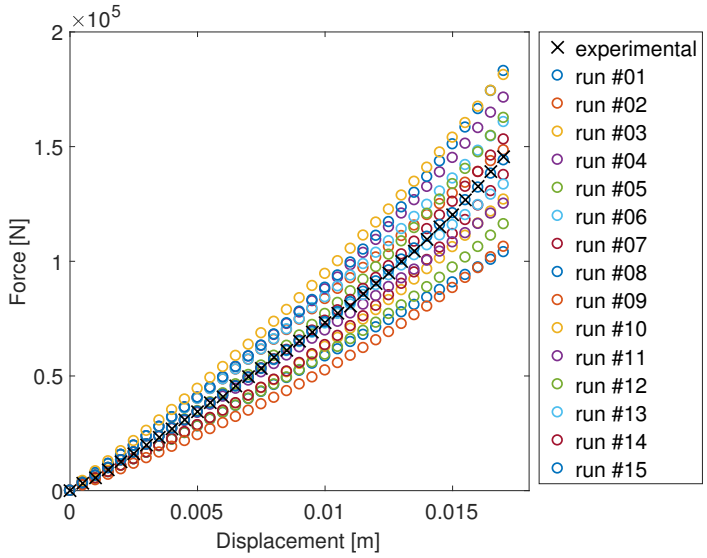

Figure 3.2: Comparison of the experimental force-displacement curve with the numerical simulations of the runs of the design

3.1.1.3 Mathematical-statistical treatment of data

A quadratic model is fitted to the points of the design. The relevant effects are selected with a backward selection procedure (i.e. progressively removing the non-relevant effects, starting from the full quadratic model).

Design-Expert 10® is used to calculate the effects and create the ANOVA table (Table 3.3). Only the effects significant at a 95% confidence level are included in the model, but the terms B and C (corresponding to the factors C_{20} and C_{30}, respectively) must be considered because their higher-order effects are significant (hierarchy principle in the selection of the relevant effects, [67]).

The response surface equation created by Design-Expert® using the coded values of the

Table 3.3: ANOVA table

Source	Sum of squares	DF	Mean square	F value	Prob >F
Model	0.109 202 613	9	0.012 133 624	5160.665 737	$2.238\,37 \times 10^{-9}$
A-C_{10}	0.000 101 396	1	0.000 101 396	43.125 745 06	0.001 227 993
B-C_{20}	$5.544\,91 \times 10^{-9}$	1	$5.544\,91 \times 10^{-9}$	0.002 358 36	0.963 147 741
C-C_{30}	$2.433\,17 \times 10^{-6}$	1	$2.433\,17 \times 10^{-6}$	1.034 875 574	0.355 687 198
AB	0.024 613 688	1	0.024 613 688	10 468.679 52	$1.690\,95 \times 10^{-9}$
AC	0.003 746 539	1	0.003 746 539	1593.475 831	$1.860\,05 \times 10^{-7}$
BC	0.000 628 37	1	0.000 628 37	267.257 991 6	$1.562\,15 \times 10^{-5}$
A^2	0.046 355 777	1	0.046 355 777	19 716.012 06	$3.475\,52 \times 10^{-10}$
B^2	0.000 645 055	1	0.000 645 055	274.354 558 9	$1.464\,57 \times 10^{-5}$
C^2	$2.423\,02 \times 10^{-5}$	1	$2.423\,02 \times 10^{-5}$	10.305 559 69	0.023 722 726
Residual	$1.175\,59 \times 10^{-5}$	5	$2.351\,17 \times 10^{-6}$		
Cor Total	0.109 214 369	14			

factors is the following:

$$
\begin{aligned}
E_f = {} & 0.999\,701\,073\,356\,79 - 2.724\,804\,595\,612\,73 \times 10^{-3}\,\mathrm{A} + \\
& + 2.014\,986\,308\,583\,68 \times 10^{-5}\,\mathrm{B} + 4.220\,958\,923\,416\,56 \times 10^{-4}\,\mathrm{C} - \\
& - 0.055\,468\,108\,146\,49\,\mathrm{AB} - 0.021\,640\,642\,053\,02\,\mathrm{AC} - \\
& - 8.862\,632\,710\,735\,19 \times 10^{-3}\,\mathrm{BC} - 0.087\,513\,013\,539\,31\,\mathrm{A}^2 - \\
& - 0.010\,323\,315\,302\,88\,\mathrm{B}^2 - 2.000\,777\,952\,844\,32 \times 10^{-3}\,\mathrm{C}^2
\end{aligned}
\tag{3.1}
$$

The corresponding model equation, substituting in Equation (3.1) the expression for the

actual factor levels (Equation (2.5)), is

$$
\begin{aligned}
E_f = {} & -2.253\,577\,024\,882\,92 + 7.107\,987\,326\,996\,32 \times 10^{-6}\, C_{10} + \\
& + 2.750\,789\,541\,410\,79 \times 10^{-6}\, C_{20} + +1.087\,332\,715\,807\,09 \times 10^{-6}\, C_{30} - \\
& - 2.958\,299\,101\,146\,03 \times 10^{-12}\, C_{10}\, C_{20} - 1.154\,167\,576\,161\,13 \times 10^{-12}\, C_{10}\, C_{30} - \\
& - 5.672\,084\,934\,870\,91 \times 10^{-13}\, C_{20}\, C_{30} - 3.889\,467\,268\,413\,93 \times 10^{-12}\, C_{10}^2 - \\
& - 6.606\,921\,793\,843\,77 \times 10^{-13}\, C_{20}^2 - 1.280\,497\,889\,820\,32 \times 10^{-13}\, C_{30}^2
\end{aligned}
\tag{3.2}
$$

3.1.1.4 Evaluation of the fitted model

The first step in the evaluation of the fitted model is the analysis of the F-values of the model and of each relevant effect, calculated in the ANOVA table.

As reported by Design-Expert®, the computed P values show that the model produced in the analysis is significant and the Model F-value of 5160.665 737 implies that there is only a 0.01% chance that an F-value this large could occur due to noise.

It can be seen that the effects related to the coefficient C_{10} have the highest F values. This implies that the Yeoh coefficient C_{10}, corresponding to the coded variable A is the most important factor in this analysis.

For the same reason, the coefficient C_{30} is the least important coefficient of this analysis, being related to the lowest F-values.

Furthermore, Model's R^2, Adjusted R^2 and Predicted R^2 coefficients are respectively

0.999 892 359 671 48, 0.999 698 607 080 14 and 0.998 976 059 434 48. The R^2 coefficient expresses a satisfactory match between the quadratic model and the experimental data. The values of Adjusted R^2 and Prediction R^2 are in good agreement.

The next step in the evaluation of the regression model is the check of the assumptions of ANOVA, performed by examining the distribution of the residuals.

Residuals are plotted in their studentized form, because it is more effective than the ordinal or standardized form in showing trends [67]. Studentized residuals are calculated with the equation

$$r_{ij} = \frac{\varepsilon_{ij}}{MS_E \left(1 - \text{Leverage}_{ij}\right)} \tag{3.3}$$

where MS_E is the error sum of squares and Leverage_{ij} is a measure of the influence of the ij-th observation on the model [67].

Figure 3.3 shows the normal plot of the residuals. The fact that the plot resembles a straight line demonstrates that the residuals are normally distributed, thus validating assumption #1 of ANOVA.

To validate assumption #3 of ANOVA, residuals are plotted against the predicted values (in Figure 3.4) and the levels of the factors (in Figure 3.5). Figure 3.4 doesn't show any pattern in the distribution of the residuals. Figure 3.5 shows that the variance of the residuals is roughly the same for each level of the factors of the design.

This proves that the residuals are structureless, as they are not related to any other variable.

Lastly, the predictive capability of the model is checked, using a set of validation points.

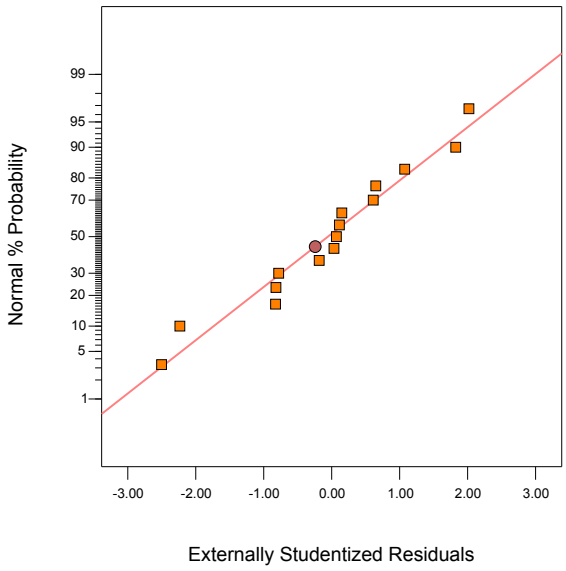

Figure 3.3: Normal plot of the residuals

Four additional sets of Yeoh coefficients, belonging to the design space, are created. As done before, the results of the numerical simulation of these four new points are matched with the experimental force-displacement curve, as described in Section 2.1.1.10. The Nash-Sutcliffe efficiency index for those points is then compared with the corresponding value calculated by the predictive model, expressed by means of a confidence interval.

Table 3.4 collects the results of the validation analysis. It can be seen that the E_f value of each one of the validation points falls inside the corresponding 95% confidence interval predicted by the statistical model. This proves that Equation (2.6) can provide a reliable prediction of the behaviour of the system.

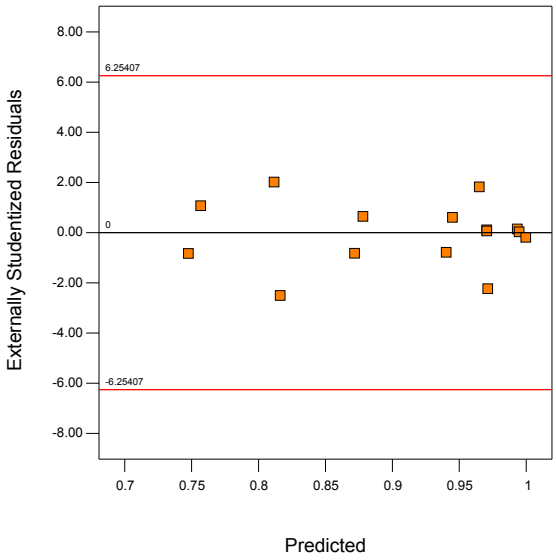

Figure 3.4: Residuals vs. Predicted values

Table 3.4: Validation points

#	C_{10}	C_{20}	C_{30}	95% confidence interval		E_f
				Low boundary	High boundary	
16	775 000	62 500	187 500	0.966 935 309	0.973 192 619	0.970 593 423
17	925 000	62 500	62 500	0.987 091 146	0.993 348 456	0.990 447 419
18	775 000	187 500	62 500	0.983 447 096	0.989 704 406	0.986 901 682
19	925 000	187 500	187 500	0.948 979 016	0.955 236 327	0.951 743 56

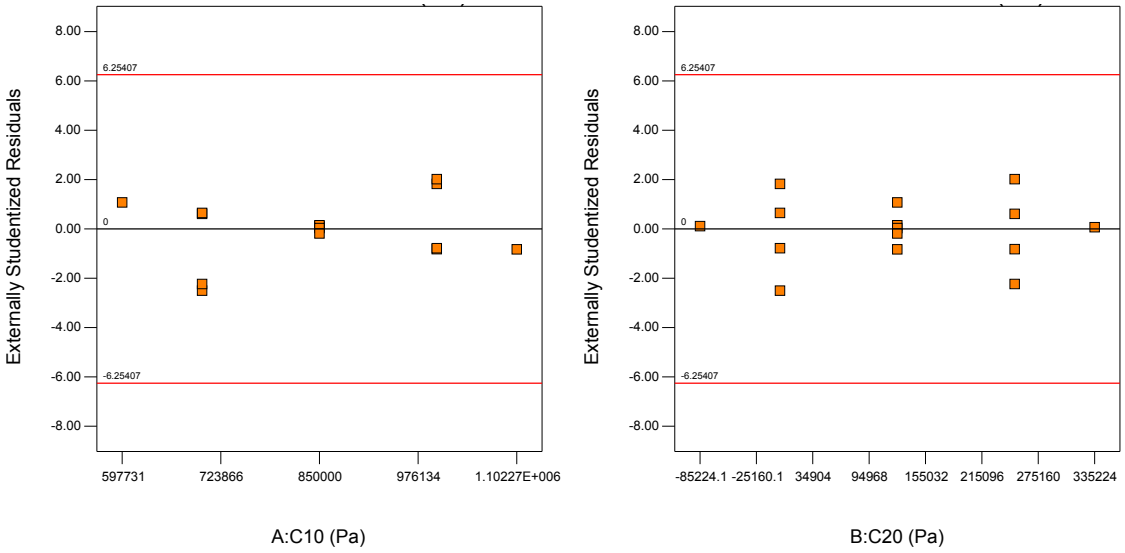

(a) C_{10}

(b) C_{20}

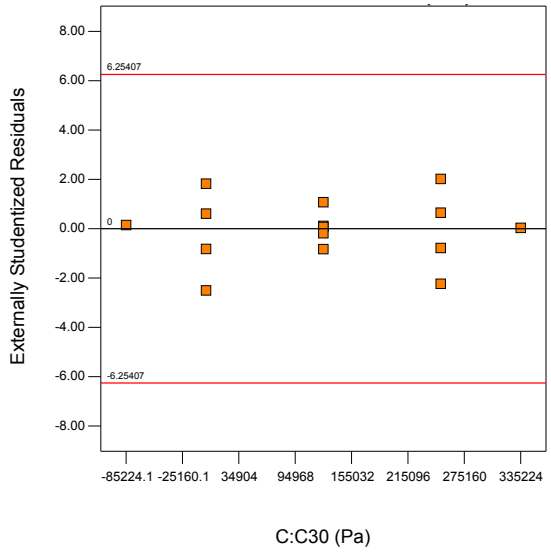

(c) C_{30}

Figure 3.5: Residuals vs. Factors of the design

3.1.1.5 Optimization

In order to gain a better understanding of the results, the response surface defined by Equation (3.2) is plotted in Figure 3.6. Each surface corresponds to a different value of the coefficient C_{30}. It can be seen that, for each value of C_{30}, the highest values of the predicted Nash-Sutcliffe efficiency lie on a ridge.

As demonstrated in Section 3.1.1.3, C_{30} is the factor having the least importance in the process, as Figure 3.6 shows that values close to the optimal response can be obtained for each value of C_{30}.

The overall optimal values of the Yeoh coefficients for this model are found using a numerical procedure. The values of the response surface function are calculated over a grid of points and the region of the local maximum is found by graphic inspection of Figure 3.6. The grid is then refined close to the optimal point, in order to better assess its position. The results are shown in Table 3.5. The Nash-Sutcliffe efficiency index for this point, calculated using the same procedure as before, falls inside the 95% confidence interval estimated by the predictive model.

Furthermore, Figure 3.7 represents graphically the predictive model defined by Equation (3.2) using a slice plot. The slice planes are placed at the optimal values of the coefficients C_{10} and C_{20}. Clearly, C_{10} is the most important factor of this analysis, as the plot shows that, setting C_{10} at the optimal value, the values of E_f are close to the optimum for every choice of C_{20} and C_{30}.

In Figure 3.8 the experimental force-displacement curve of the resilient mounting ele-

ment is compared with the simulated behaviour of the numerical model having the Yeoh coefficients shown in Table 3.5.

The high value of the Nash-Sutcliffe efficiency index (Table 3.5) and the close fit between the deformation of the resilient mounting element measured experimentally and simulated with the finite element model over the entire loading range (Figure 3.8) show the accurate results achieved with the optimization technique.

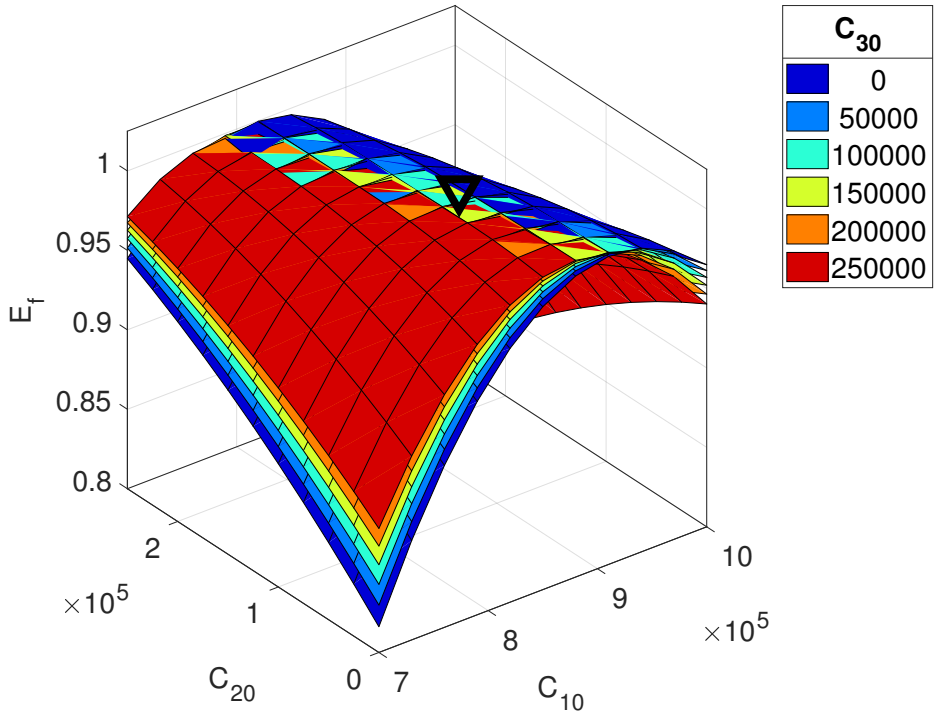

Figure 3.6: Response surface plot of Equation (3.2), parametrized by C_{30} (the position of the optimum point is marked with a ▽)

Table 3.5: Optimal point

#	C_{10}	C_{20}	C_{30}	95% confidence interval		E_f
				Low boundary	High boundary	
20	846 480	79 350	250 000	0.997 184 715 944 69	1.002 861 394 710 4	0.999 829 312 127 991

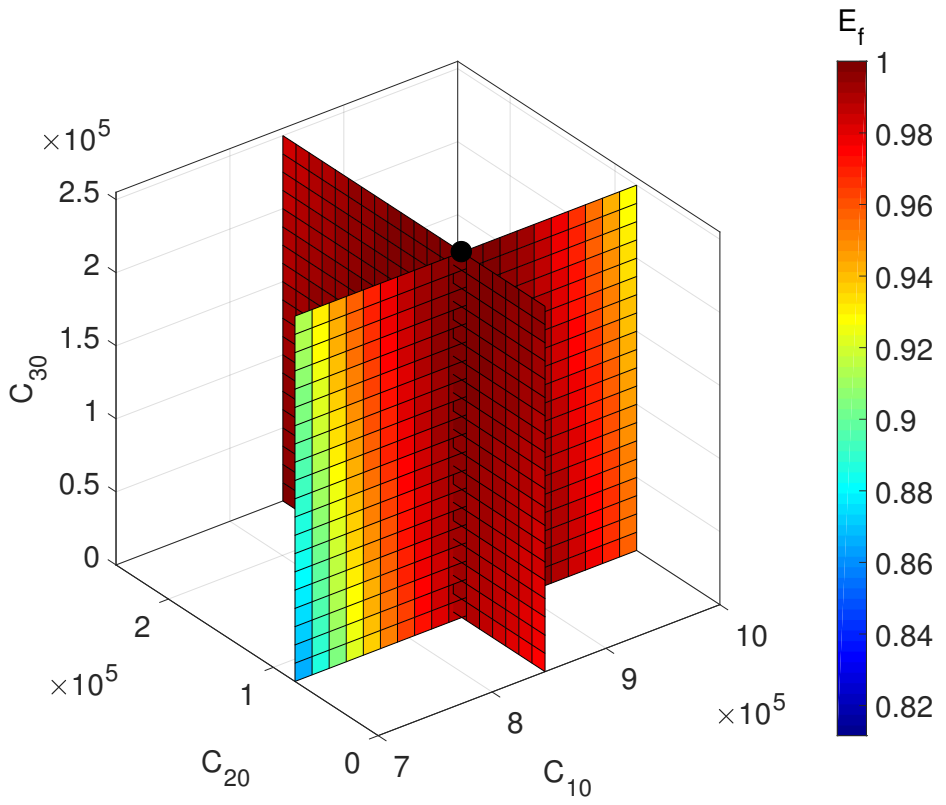

Figure 3.7: Slice plot of Equation (3.2) (the position of the optimum point is marked with a •)

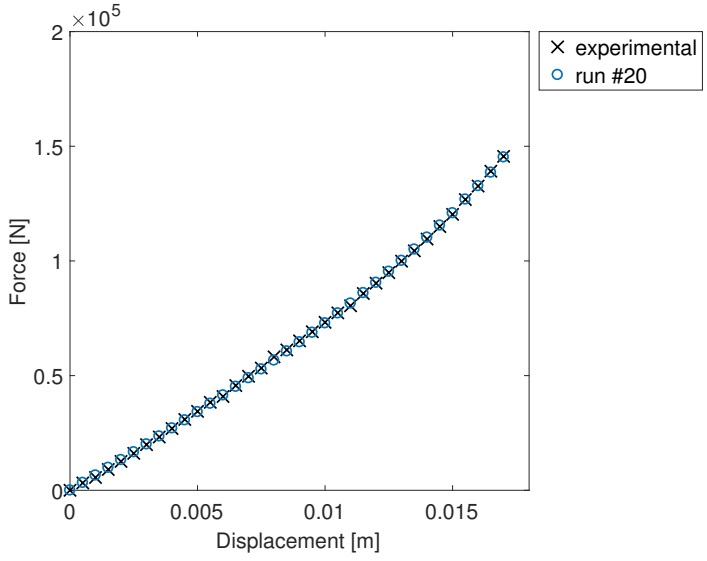

Figure 3.8: Comparison of the experimental force-displacement curve with the optimal numerical simulation

3.1.1.6 Contour plot

The distribution of I_1 in the rubber damper simulated with the numerical model is plotted in Figure 3.9 for a vertical displacement of $\Delta z = 1 \times 10^{-2}$ m. I_1 is an essential quantity for this analysis, as the constitutive relation of the Yeoh model (Equation (2.3)) expresses the elastic strain energy W as a function of I_1.

For this reason, the plot gives the designer a better understanding of the parts of the resilient mounting element where most of the elastic energy is stored in the static deformation of the element.

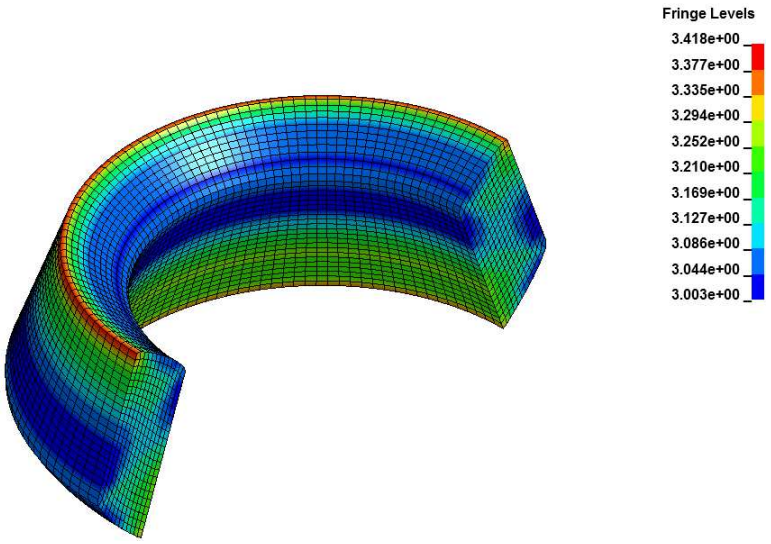

Figure 3.9: Contour plot of I_1 in the rubber damper, cutaway representation ($\Delta z = 1 \times 10^{-2}$ m)

3.1.2. Dynamic characterization

3.1.2.1 Validation of the requirements for the experimental measurement of the dynamic properties of the isolators

The requirements of the ISO Standard [28] were validated. The results of the experimental analysis of the cylindrical resilient mount are presented in this Section.

The results of the assumption of linearity in the dynamics of the system, discussed in **??** 2.1.2.4.1, are shown in Figure 3.10. The Figure shows the dynamic transfer stiffness ($K(\omega)$) measured for 3 levels of excitation (100, 110, and 120 dB, respectively).

The test shows that the experimental results are compatible with the linearity assumption, respecting the criteria defined in [28] for the frequency range of interest (100-1000 Hz).

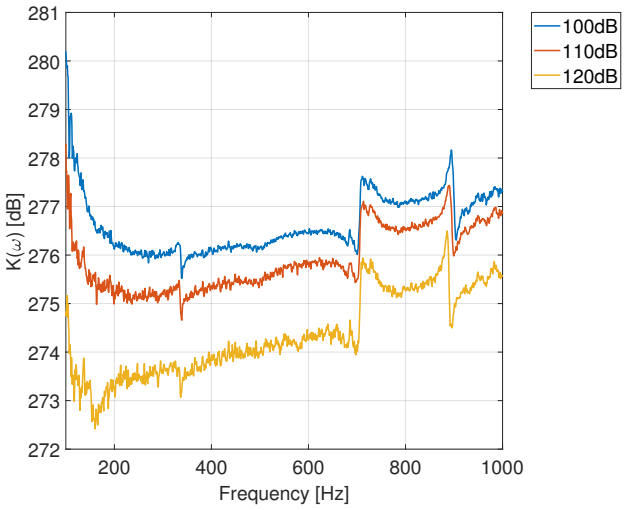

Figure 3.10: Experimental FRF measured for three excitation levels

The requirement of low input vibrations in unwanted directions, discussed in **??** 2.1.2.4.2, is then successfully verified. The acceleration levels in the direction of excitation (z) and

tangential and vertical directions (x and y, respectively) are plotted in Figure 3.11. The dashed line denotes the threshold set in the ISO Standard, calculated with Equation (2.12).

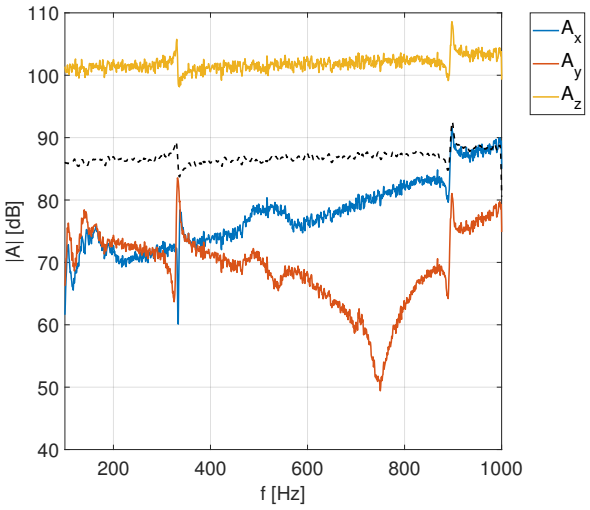

Figure 3.11: Spectra of the acceleration signals measured in the radial (x), tangential (y) and vertical (z) directions; dashed line represents threshold levels

3.1.2.2 Experimental transmissibility curves

The transmissibility curves acquired for the two vibration isolators are shown in Figure 3.12. The transmissibility curve of the conical resilient mount (Figure 3.12b) shows an internal condition of resonance at 540 Hz. In order to accurately characterize the dynamic behaviour of the isolator in the Transfer Path Analysis, this critical point needs to be accurately represented. On the contrary, the cylindrical element shows no significant conditions of resonance in the frequency range under investigation.

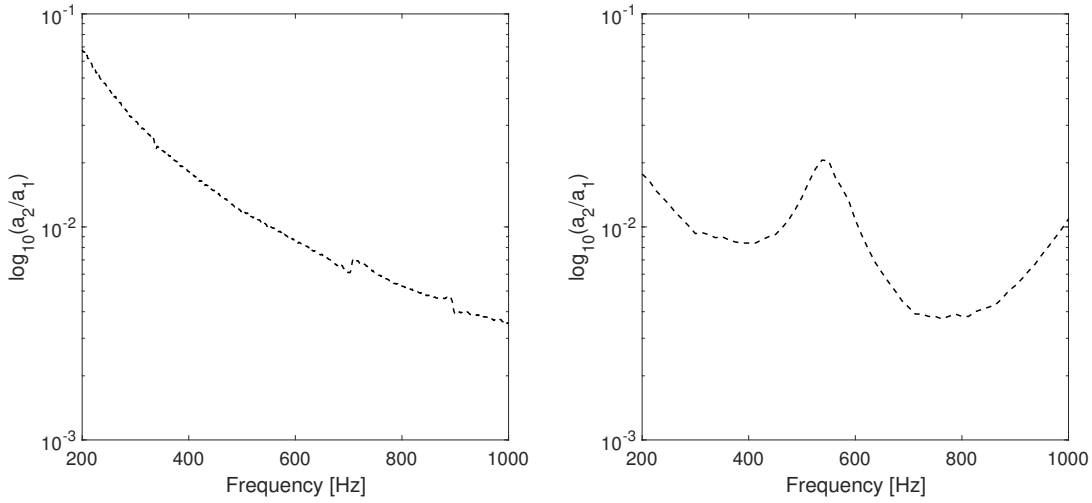

(a) Cylindrical mount (b) Conical mount

Figure 3.12: Experimental transmittance curves

3.1.2.3 Analysis of the resonance conditions using ODS

An ODS analysis is performed to determine the nature of possible conditions of resonance highlighted in the spectra of the transmissibility FRF. The modal shape of the system under analysis can be evaluated by comparing amplitude and phase of a reference signal with the acceleration signals measured in different points of the system. The reference signal is measured on the central axis of the excitation mass. The measurement points (marked with Point 1–8 in Figure 3.13) are located on the lateral surface of the excitation mass and the blocking mass. Acceleration signals of the measurement points are acquired using triaxial accelerometers, and the results are processed using the dedicated library of the MATLAB Abravibe toolbox [14]. The tests are performed exciting the system with the acceleration spectra used for the measurement of the transmissibility FRF. Using this analysis, it is possible to discern between the resonance conditions of the isolator under analysis, and the

potential resonance conditions of the experimental test rig.

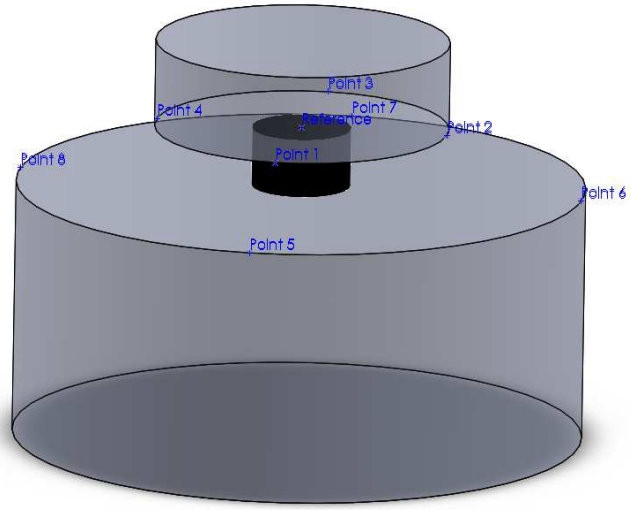

Figure 3.13: Position of the reference point and the 8 measurement points (1–8) on excitation and blocking mass

Measured spectra for the ODS analysis of the cylindrical resilient mount are shown in Figure 3.14. The plot shows an increase in the acceleration spectra at 332 Hz. Since this condition is not visible in the spectrum of the transmissibility response function (Figure 3.12a), it is analyzed visually by comparing the phases of the acceleration signals acquired in the measurement points. The results of the ODS analysis for this point are presented in Figure 3.15, which shows the motion of the measurement points at the selected frequency. This way, it is easy to conclude that the motion detected in the analysis of the spectra of the measurement points is caused by the wobbling motion of the excitation mass. It does not represent a resonance condition of the resilient mount, because the blocking mass appears to be still.

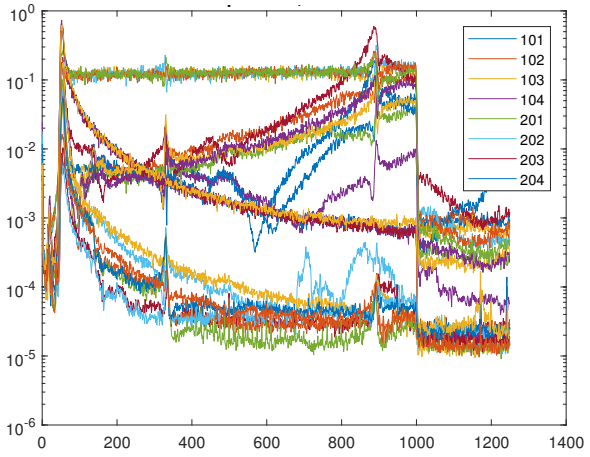

Figure 3.14: ODS: spectra of the FRF in the measurement points

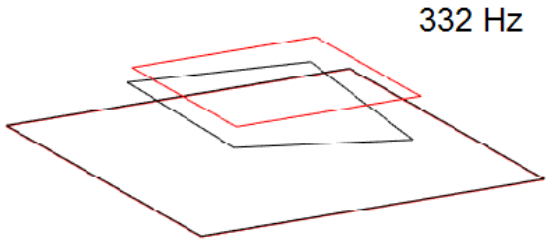

Figure 3.15: ODS: diagnostics of the peak highlighted in the FRF spectra: red lines show the original position of the measurement points, and the deformed configuration is drawn with black lines

3.1.2.4 Definition of the experimental design and results of the dynamic simulations

Eight numerical factors are used to create the experimental design. The factors are the values of the modal damping ratio, at the frequency lines 0, 200, 400, 600, 800, 1000, 1200, and 1400 Hz. This allowed for the analysis of the entire frequency range measured in the experimental tests.

These values are tested in the finite-element model of the dynamic behaviour of the isolators, described in Section 2.1.2.5. Each value is varied in the range 1-5%. A Latin Hypercube Design [65] is used to define the values of the factors for each run of the design.

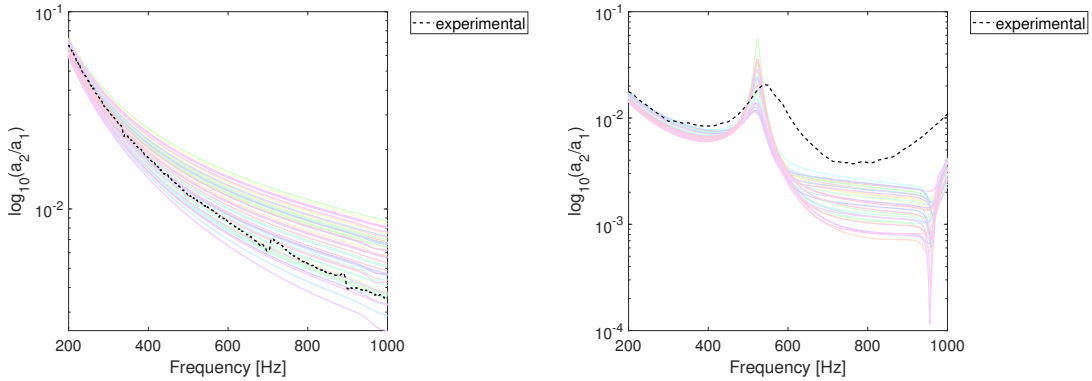

(a) Cylindrical mount (b) Conical mount

Figure 3.16: FRF of the numerical simulations of each point of the design table (transparent lines), compared to the experimental results (black dashed line)

The factors of the experiment, alongside the symbols for the coded variables, are presented in Table 3.6.

Table 3.6: Factors of the experimental design of the frequency-dependent damping ratios

Factor	Units	Frequency line [Hz]	Range and coded levels −1	0	+1	Coded variable
ζ_1	%	0	1	5.5	10	A
ζ_2	%	200	1	5.5	10	B
ζ_3	%	400	1	5.5	10	C
ζ_4	%	600	1	5.5	10	D
ζ_5	%	800	1	5.5	10	E
ζ_6	%	1000	1	5.5	10	F
ζ_7	%	1200	1	5.5	10	G
ζ_8	%	1400	1	5.5	10	H

The table of design for the cylindrical and conical isolators are shown in Tables 3.7 and 3.8 respectively. The value of the modal damping ratio for the i-th frequency line is represented with the symbol ζ_i. Figure 3.16 shows the transmissibility response functions simulated for each point of the two experimental designs.

The procedure I followed to validate the predictive model produced by ANOVA is

analogous to what was done in [35] for the ANOVA of the Yeoh coefficients of the rubber material.

Table 3.7: Cylindrical mount: design table

#	ζ_1 [%]	ζ_2 [%]	ζ_3 [%]	ζ_4 [%]	ζ_5 [%]	ζ_6 [%]	ζ_7 [%]	ζ_8 [%]
01	7.628	5.196	2.660	8.121	7.753	6.765	3.687	3.479
02	3.515	8.453	4.359	4.314	1.871	3.39	9.346	3.789
03	3.317	7.441	8.295	2.925	9.384	2.508	1.574	3.958
04	7.963	5.584	3.322	4.162	5.885	8.588	6.882	6.208
05	9.508	2.61	5.489	4.904	2.862	7.412	3.964	3.670
06	2.481	5.962	8.045	1.735	3.167	3.718	2.464	9.728
07	4.933	9.606	5.127	6.641	7.949	1.578	4.864	7.383
08	1.577	9.941	8.761	9.608	6.146	4.796	4.097	8.288
09	9.250	7.491	7.409	8.984	5.000	5.064	8.814	2.958
10	8.251	2.827	1.641	4.594	3.358	6.027	3.721	2.412
11	7.466	8.874	9.577	7.879	7.360	8.937	1.460	1.286
12	8.129	2.372	6.574	1.360	1.329	9.890	2.063	6.815
13	6.253	7.888	2.309	8.671	6.882	3.925	1.733	6.619
14	4.325	1.399	1.836	5.199	9.771	3.236	7.225	4.665
15	2.269	6.938	1.425	5.133	5.818	9.641	5.585	1.075
16	8.863	1.860	1.041	8.482	3.574	7.810	5.916	2.445
17	8.996	9.448	3.758	5.649	8.684	9.332	6.210	5.945
18	7.806	2.673	6.313	3.595	2.085	7.090	5.079	8.508
19	4.529	2.102	8.954	7.086	1.565	7.286	3.017	7.805
20	5.68	3.830	6.926	3.811	5.208	4.126	1.359	9.961
21	7.058	6.995	6.755	2.641	5.522	1.261	7.470	8.661
22	3.536	3.135	2.542	5.86	8.325	6.441	3.291	5.398
23	2.134	9.753	2.954	1.598	8.087	8.19	5.436	4.075
24	3.875	1.210	7.155	6.169	6.286	7.652	4.459	2.203
25	4.153	5.015	3.700	1.032	2.746	1.795	5.826	6.529

#	ζ_1 [%]	ζ_2 [%]	ζ_3 [%]	ζ_4 [%]	ζ_5 [%]	ζ_6 [%]	ζ_7 [%]	ζ_8 [%]
26	1.958	6.455	5.843	2.027	2.515	2.663	2.367	3.049
27	2.908	4.266	2.004	3.090	4.401	8.347	2.855	2.040
28	6.192	1.667	5.278	3.169	4.816	5.404	6.251	7.989
29	1.259	6.283	9.828	7.510	9.842	4.317	9.542	5.677
30	4.969	3.286	4.533	3.900	9.523	3.591	2.636	7.567
31	7.127	6.050	1.272	7.132	3.150	3.153	8.395	1.900
32	8.562	4.099	3.112	6.557	9.111	9.591	8.629	5.040
33	6.430	8.591	6.116	5.437	7.110	4.748	7.496	6.300
34	5.562	8.967	7.746	9.692	6.715	2.345	6.599	9.267
35	8.404	8.237	3.344	2.507	8.852	6.088	2.198	9.569
36	3.905	7.227	5.561	9.310	8.486	1.375	9.101	4.281
37	4.643	4.756	6.968	8.880	6.550	6.394	8.040	4.497
38	1.870	6.731	8.004	6.343	1.010	4.452	7.775	1.647
39	6.926	1.933	7.584	1.501	4.037	8.407	6.979	7.206
40	1.088	4.055	2.253	4.775	4.644	2.895	4.721	3.269
41	3.143	4.862	9.172	9.878	7.545	5.253	8.352	9.448
42	9.741	4.452	3.928	8.328	2.385	6.746	8.967	4.820
43	9.404	3.529	5.917	3.514	7.279	2.049	1.066	5.182
44	9.932	3.437	9.809	7.789	4.428	5.559	6.472	2.698
45	1.361	7.827	9.338	2.420	1.392	8.814	4.377	1.429
46	2.643	9.186	8.505	6.927	2.053	2.140	5.269	8.094
47	5.149	8.165	4.717	9.175	4.169	7.939	9.856	8.809
48	5.994	1.126	8.609	6.038	5.417	9.137	7.914	5.817
49	5.491	5.324	4.941	2.108	3.747	5.778	9.766	8.958
50	6.610	5.830	4.195	7.468	8.942	1.019	3.467	6.993

Table 3.8: Conical mount: design table

#	ζ_1 [%]	ζ_2 [%]	ζ_3 [%]	ζ_4 [%]	ζ_5 [%]	ζ_6 [%]	ζ_7 [%]	ζ_8 [%]
01	4.900	1.131	3.722	4.734	1.638	4.771	2.306	3.994
02	3.982	3.557	2.683	2.691	4.427	3.649	2.880	3.223
03	1.065	2.432	3.905	2.268	4.677	2.180	3.388	1.450
04	3.593	2.211	1.957	1.745	3.268	1.467	4.33	2.333
05	3.704	2.366	1.067	2.789	3.621	4.540	2.057	2.471
06	3.417	1.727	2.920	2.503	1.514	3.596	3.332	4.758
07	3.104	4.988	2.010	1.590	3.199	4.943	4.672	4.040
08	1.590	4.817	4.605	2.983	4.120	1.327	1.275	4.38
09	4.100	4.749	4.411	1.414	2.407	3.433	3.032	3.445
10	1.726	4.136	2.553	3.761	4.981	2.251	2.484	1.882
11	2.334	1.795	1.196	1.049	1.232	4.406	1.897	4.374
12	4.390	3.000	3.514	3.513	2.299	1.877	1.872	2.174
13	4.316	1.996	4.326	4.351	2.718	2.846	3.823	1.525
14	2.450	1.099	4.853	2.031	1.084	2.684	4.909	1.846
15	1.853	2.693	1.296	3.082	3.700	4.369	1.402	3.508
16	3.254	4.109	2.797	3.448	3.074	3.905	3.954	3.030

#	ζ_1 [%]	ζ_2 [%]	ζ_3 [%]	ζ_4 [%]	ζ_5 [%]	ζ_6 [%]	ζ_7 [%]	ζ_8 [%]
17	4.824	3.874	3.209	1.231	2.952	2.050	1.657	3.772
18	4.644	3.409	3.775	3.148	4.174	2.393	4.763	4.928
19	3.173	3.081	4.000	4.047	4.604	1.501	4.095	4.526
20	2.078	2.527	3.377	1.908	3.976	3.759	2.609	2.709
21	4.140	3.195	4.234	4.399	2.238	3.324	3.597	4.722
22	2.652	4.445	2.471	4.992	2.585	1.875	2.831	1.336
23	4.567	4.619	3.122	4.506	3.779	1.682	4.214	1.177
24	1.148	3.744	1.549	3.313	1.471	3.099	2.134	1.646
25	2.763	4.364	1.486	2.406	1.282	4.723	1.244	3.339
26	3.821	3.926	4.949	4.157	1.788	3.209	3.176	2.575
27	1.333	1.470	2.139	2.146	2.772	1.113	4.480	4.142
28	2.175	3.270	3.306	4.855	4.772	1.157	1.520	2.798
29	1.387	2.768	4.704	3.943	3.463	4.156	2.729	2.001
30	1.912	1.255	1.724	3.673	2.086	2.932	3.687	2.975
31	2.578	1.564	1.820	1.758	1.935	2.583	1.000	3.647
32	2.908	2.097	2.255	1.271	4.334	4.021	4.581	1.041

3.1.2.5 Optimal values

In Figure 3.17 the experimental transmissibility curves of the two resilient mounting elements under test are compared with the numerical transmissibility curves obtained using the optimal values of the modal damping ratios. These values were determined by minimizing the square difference between the decibel-transformed experimental and numerical transmissibility functions following the procedure described in Section 2.1.2.6. In the case of the conical mount, the frequency range used in the analysis was restricted to 400–700 Hz, in order to accurately represent the internal resonance condition of the isolator. This operation is performed in an interval (400–700 Hz) of the entire frequency range analyzed in the simulations (0–1400 Hz). Nonetheless, the dynamic behaviour of the numerical model in proximity to the internal resonance mode is affected by all the values of the damping ratio that were defined across the entire frequency range of the simulations.

The experimental transmissibility curve of the conical isolator is not able to reproduce accurately the trend of the experimental values in the high-frequency range, probably due to the presence of a second internal condition of resonance of the isolator measured at 1325 Hz. The position of this second resonance peak falls outside the validation range defined by the ISO Standard, described in Section 3.1.2.1, and wasn't considered in the numerical analysis. However, position and amplitude of the transmissibility curve in the resonance condition match the experimental results adequately.

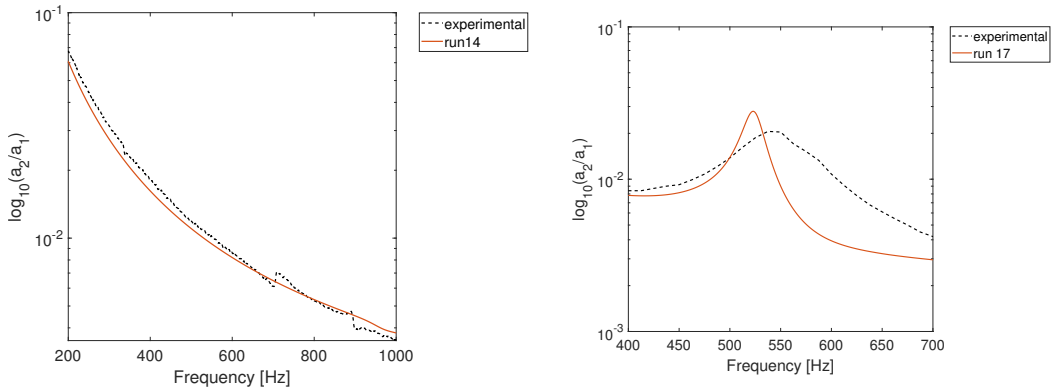

(a) Cylindrical mount (b) Conical mount

Figure 3.17: FRFs of the optimized model

3.1.2.6 Influence of static preload on the transmissibility response function

As discussed in Section 2.1.2.7, an important feature of rubber materials is the fact that their dynamic properties are a function of the state of stress of the material. For this reason, to examine the influence of the static state of stress, the dynamic behaviour of the resilient mounts under test was analyzed using different values of the vertical preload applied on the bottom surface of the blocking mass. The results for the conic resilient mount are presented here in order to analyze the variation in the position of the resonance peak. Figures 3.18 and 3.19 show the change in the shape of the simulated transmissibility curve when the preload applied on the resilient mount is gradually increased. The transmissibility is plotted for preload ranging from 0 N to the maximum static load (145 kN). The frequency response function is evaluated for 8 values of the static preload in this range. A significant shift (60 Hz) in the position of the resonance peak is observed, highlighting the importance of the static state of stress on the dynamic properties of rubber-isolating elements. As it was

expected, the isolator gets stiffer as the applied preload increases as the resonance peaks shift to higher frequencies.

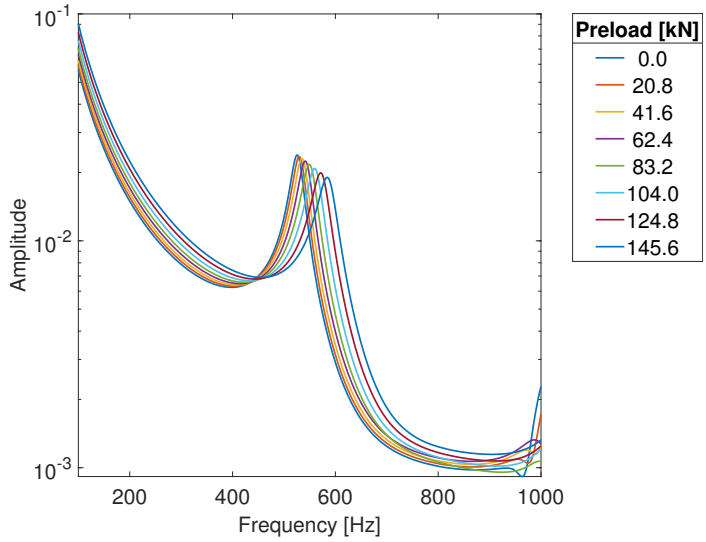

Figure 3.18: Conical mount: simulation of the transmissibility function for different values of the preload

3.2. Transfer path of underwater sound transmission

In this section, I present the outcome of the numerical simulations performed to simulate the radiated underwater noise from the vibrating structure (Figure 2.20), and the results of the experimental tests performed to estimate the value of each term of Equation (2.28).

3.2.1. Prediction of sound pressure levels at the underwater receiving point using a FE model

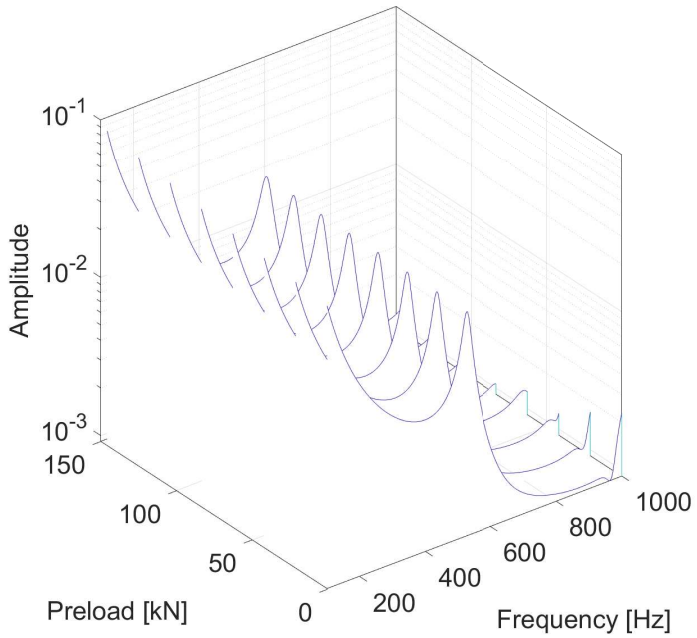

Figure 3.19: Conical mount: waterfall plot of the simulated transmissibility function for different values of the preload

3.2.1.1 Estimation of the isotropic loss factor

The numerical model of the plate test was used to estimate the isotropic loss factor of the vibrating structure (Section 2.2.8).

The optimal value of the damping coefficient of the steel material (η) is estimated with a set of numerical simulations. I measured the frequency response of the steel plate as shown in Figure 3.20. Two frequency ranges are defined: low-frequency range (0-500 Hz), and high-frequency range (500-4000 Hz). In these two regions, the optimal value of η is found by minimizing the mean-square difference between the numerical and experimental accelerance transmission functions over the range of interest. The best match between the numerical and experimental transmittance function is found for $\eta = 0.5\%$ in the low-frequency range

and $\eta = 0.1\%$ in the high-frequency range.

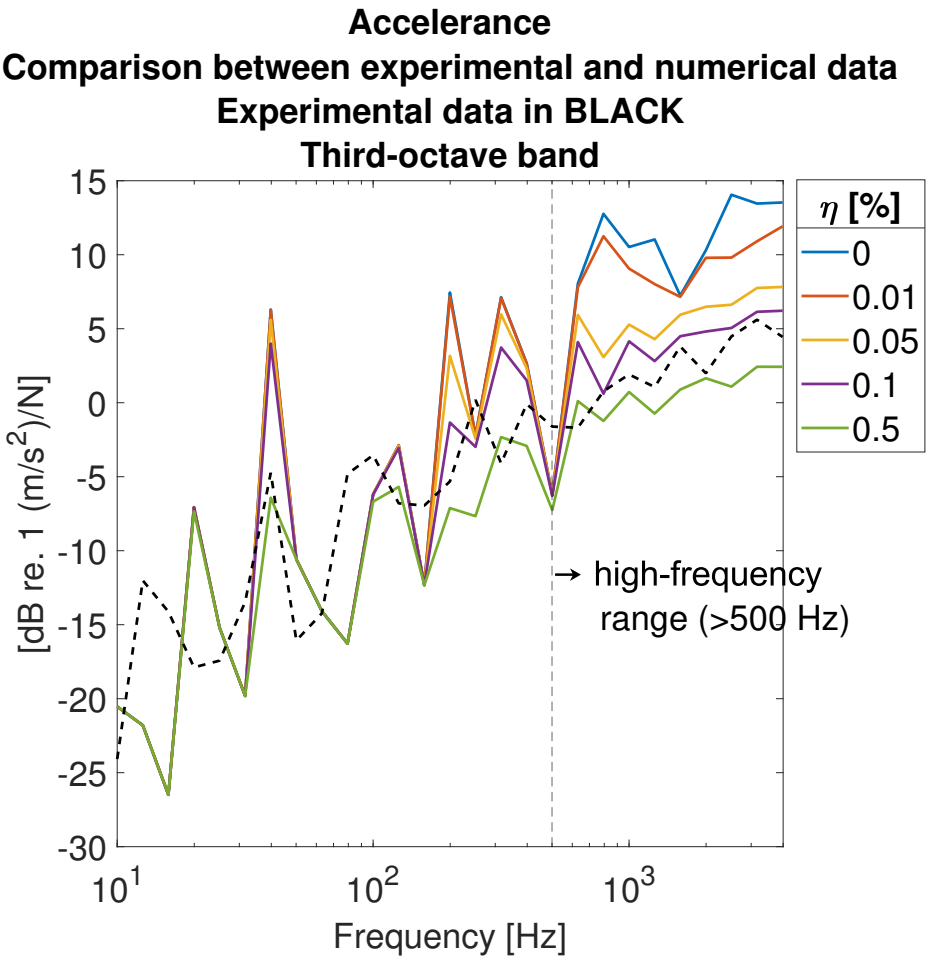

Figure 3.20: Plate structure: comparison of experimental data (dashed line) and numerical values of the accelerance transfer function, for different values of the absorption coefficient η

The comparison between the levels of accelerance and radiated average sound pressure measured in the experiment and estimated with the FE model (Figure 3.20 and Figure 3.21) shows good agreement.

3.2.1.2 Numerical model of the URN of the foundation mock-up model

The values of η were used in the numerical model for the acoustic response of the foundation mock-up (discussed in Section 2.2.8). Sound pressure levels measured experimentally and estimated with the numerical model, using the values of η calculated before, are plotted in Figures 3.21 and 3.22, in narrowband and third-octave band representation. The reason for the discrepancy in the low-frequency range is discussed in Section 2.2.7. However, simulated results closely match experimental data starting from 500 Hz.

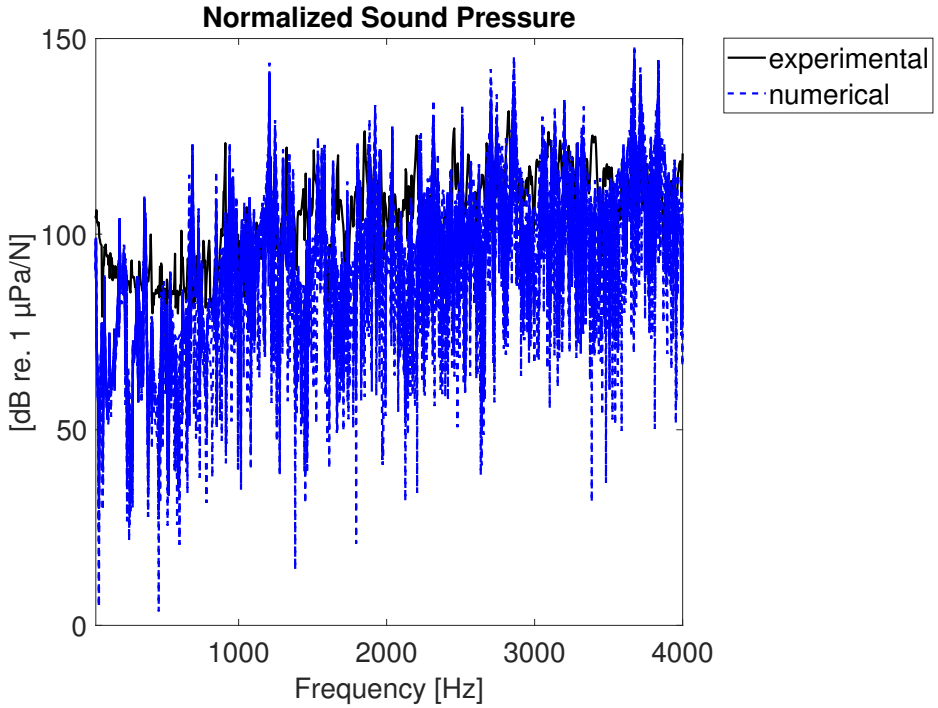

Figure 3.21: Foundation mock-up: comparison of sound pressure values, narrowband representation

3.2.2. Transfer path analysis of the underwater sound radiation

I present hereafter the results of the experimental tests performed to characterize each term of Equation (2.28).

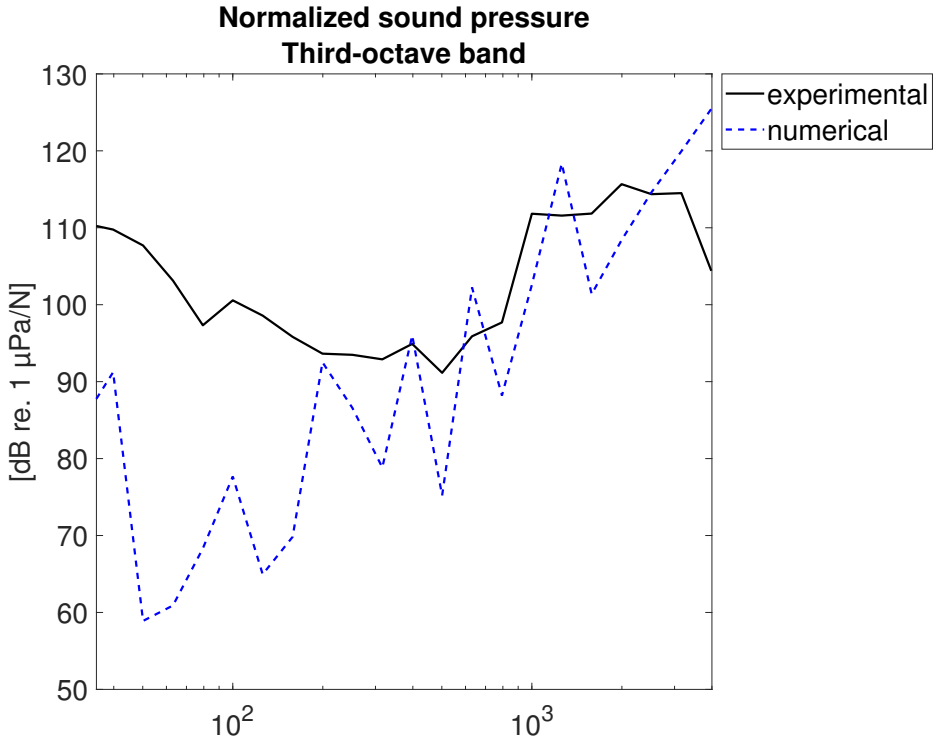

Figure 3.22: Foundation mock-up: comparison of sound pressure values, third-octave data representation

3.2.2.1 Foundation mobility functions

Figure 3.23 shows the driven-point mobility function of the top plate of the foundation. For each measuring point (1 and 2, Figure 2.15), it was obtained by measuring the structural velocity at the point of application of the input impact force. Figures 3.24 and 3.25 show the transfer mobility functions measured as the ratios of the velocity at points 3, 4, 5, and 6, induced by an impact applied at points 1, and 2 (Figure 2.15).

An example of the coherence (Equation (2.29)) measured in the experimental tests is the plot of the coherence of the acceleration signal of point 1, shown in Figure 3.26. Coherence values range between 0 and 1, where 1 indicates perfect repeatability.

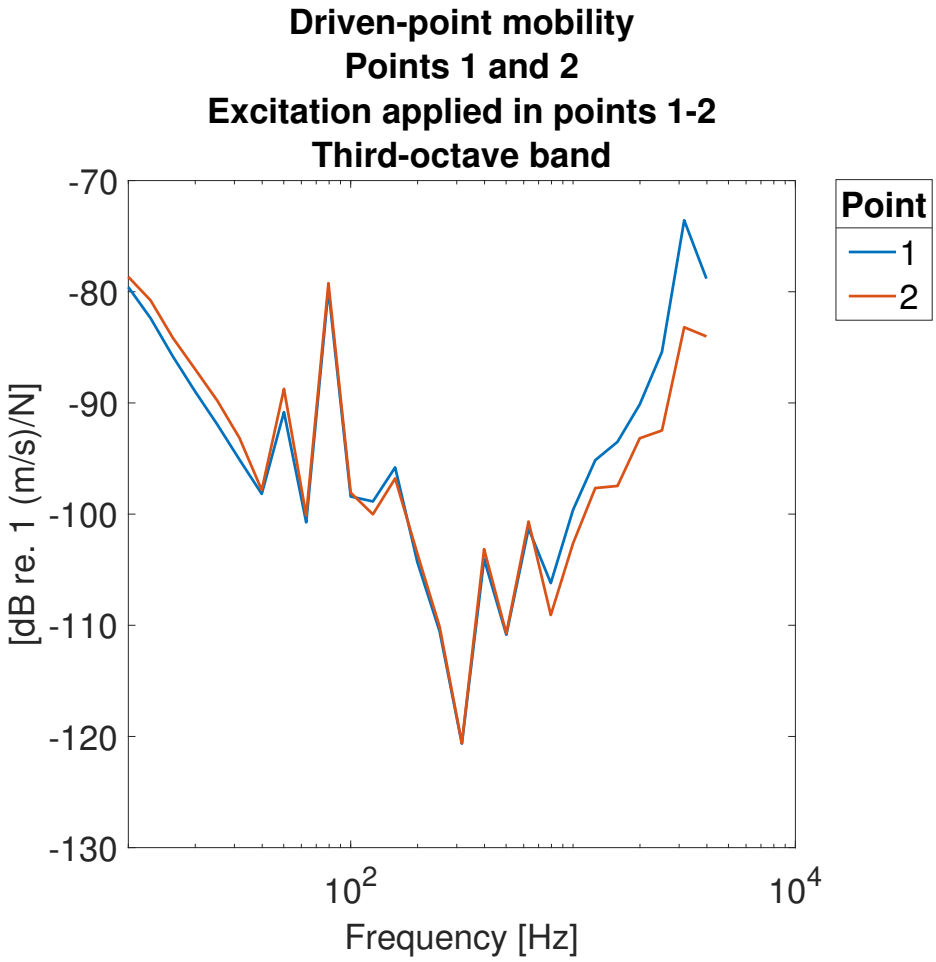

Figure 3.23: Foundation mock-up: mobility levels on top of the foundation, positions 1,2, third-octave band data

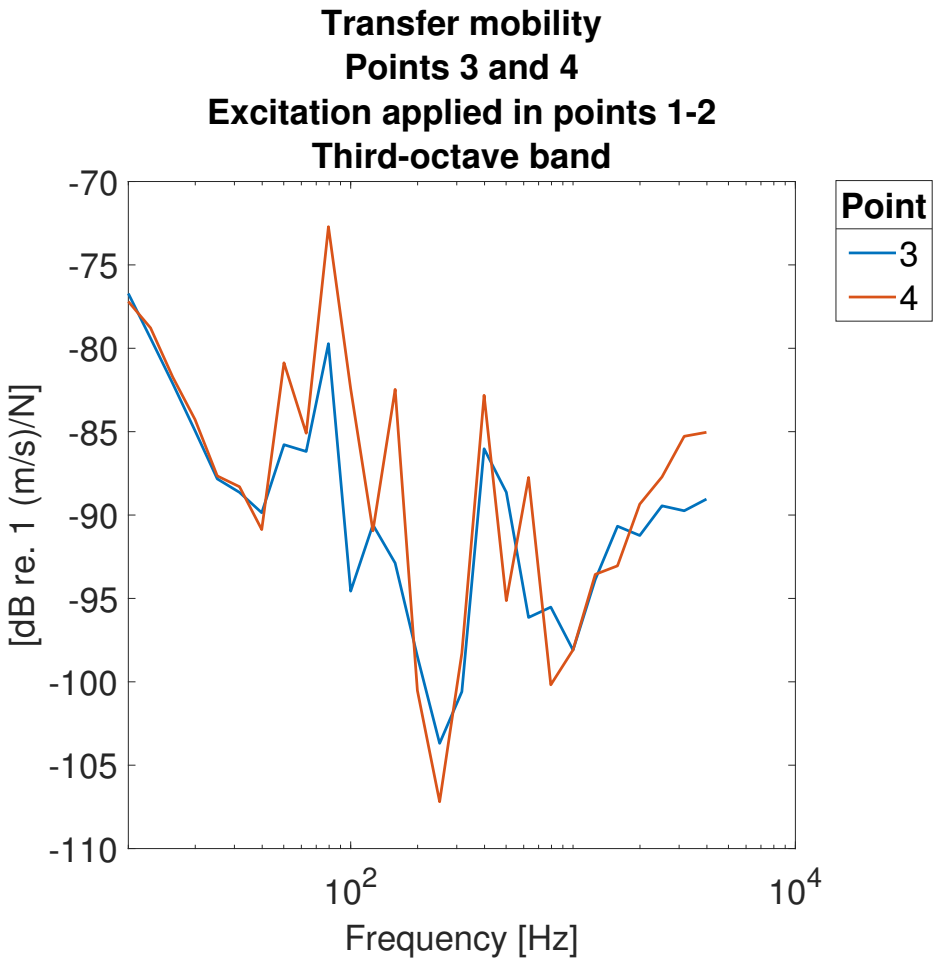

Figure 3.24: Foundation mock-up: mobility levels on the base plate, positions 3,4, third-octave band data

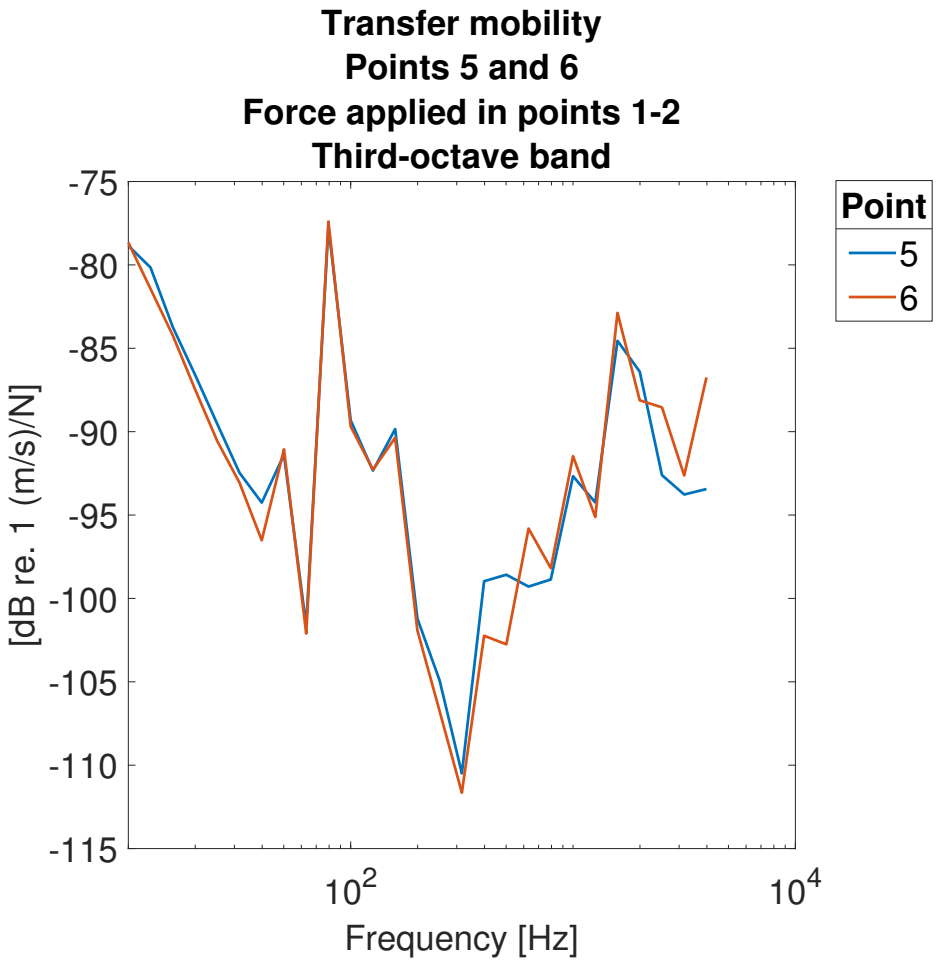

Figure 3.25: Foundation mock-up: mobility levels on the base plate, positions 5,6, third-octave band data

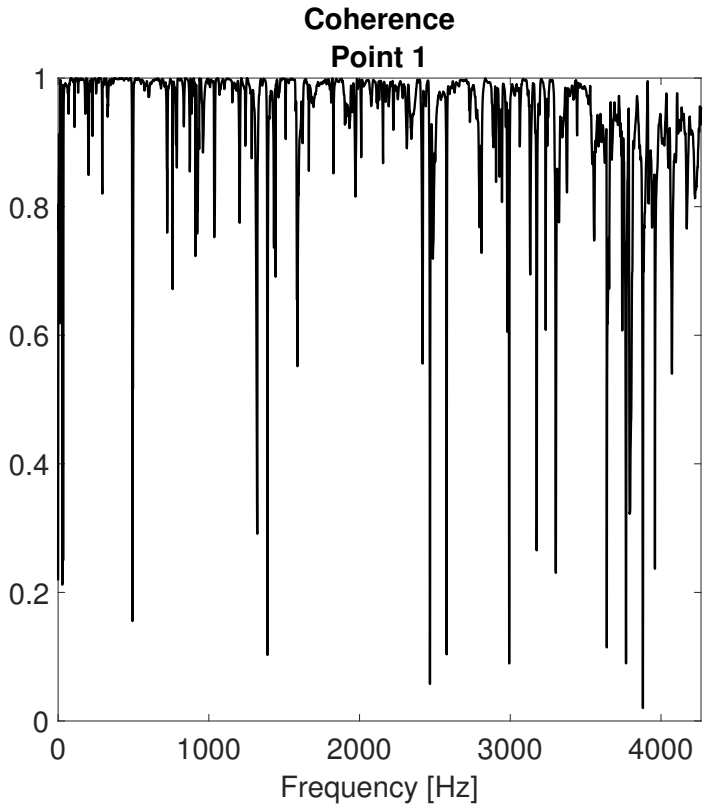

Figure 3.26: Foundation mock-up: coherence of the acceleration signal of point 1

3.2.2.2 Sound radiation efficiency

The spectra of the sound pressure signals measured in the 3 impact tests by hydrophones 1 and 2 are shown in Figures 3.27 and 3.28 respectively, as described in Section 2.2.6. Results are presented in a third-octave band representation. Background noise levels are plotted with a black line. Figure 3.29 shows the sound power (W) calculated from the sound pressure signals and the base plate velocity (Figure 3.30) according to Equation (2.26). Figure 3.31 shows the radiation efficiency (σ) of the foundation base plate obtained according to Equation (2.21). The values of σ_{rev} calculated this way can be used in Equation (2.28).

Despite the more complex geometry of the radiating structure, and the use of an impulse force instead of a steady-state excitation, the values of σ_{rev} are consistent with the results of the works of Pan [78] and Wang et al. [99], who developed an analytical model to represent the underwater sound radiation of vibrating plates. The value of σ_{rev} depends on the geometry and material of the radiating structure. Each case study requires the estimation of σ_{rev}. As shown in Section 3.2.1.2, numerical models are valuable for this type of analysis because they provide a preliminary estimation of sound pressure levels at the receiver and an estimation of the sound radiation efficiency in the underwater environment. Therefore, also in this case they can be used to assess the effectiveness of alternative design solutions in mitigating URN.

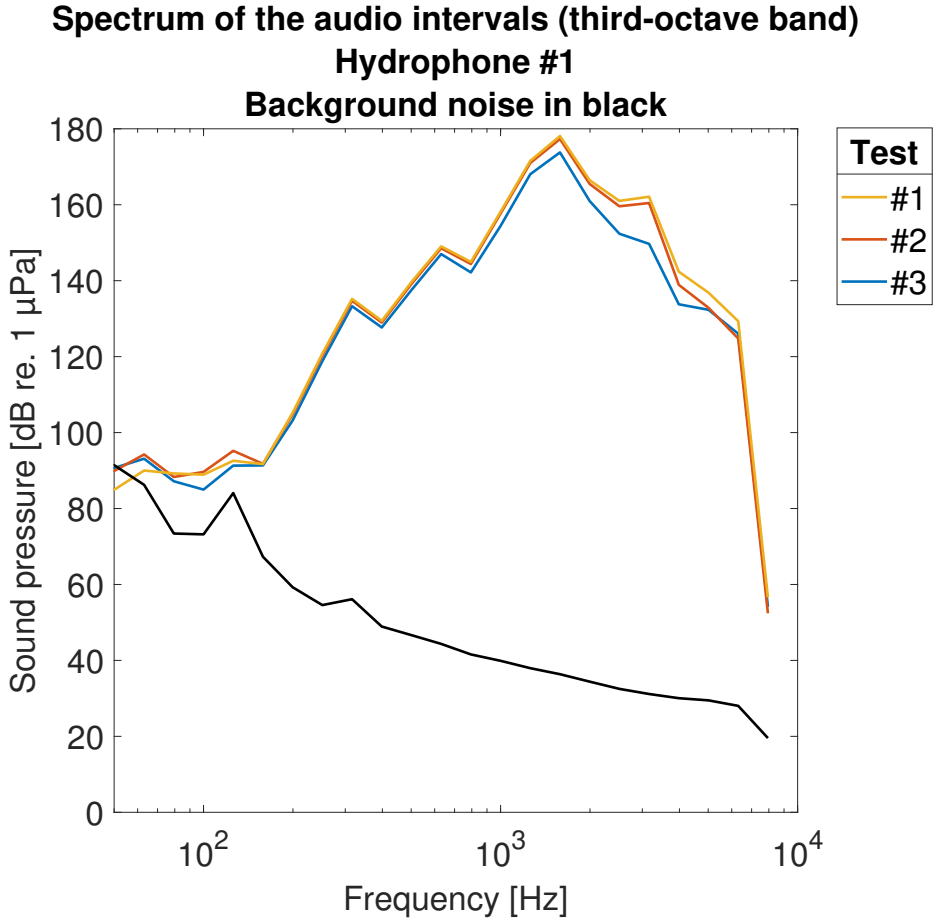

Figure 3.27: Foundation mock-up: spectrum of audio intervals and background noise (third-octave band representation, hydrophone #1)

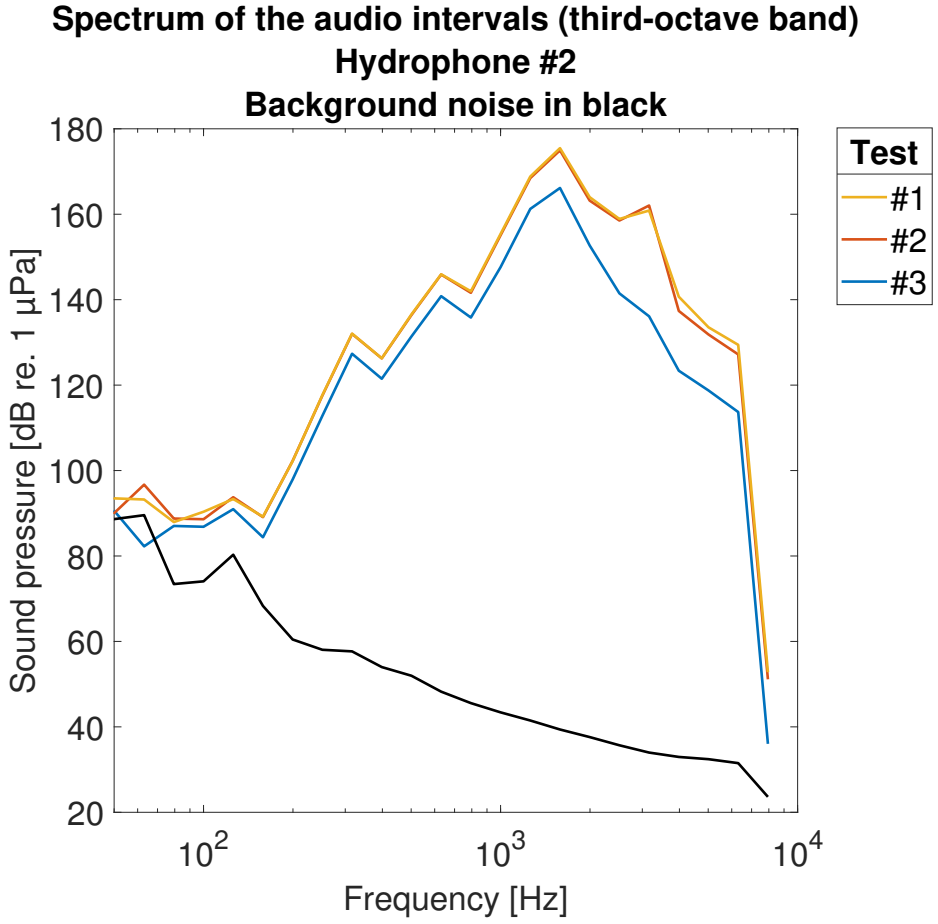

Figure 3.28: Foundation mock-up: spectrum of audio intervals and background noise (third-octave band representation, hydrophone #2)

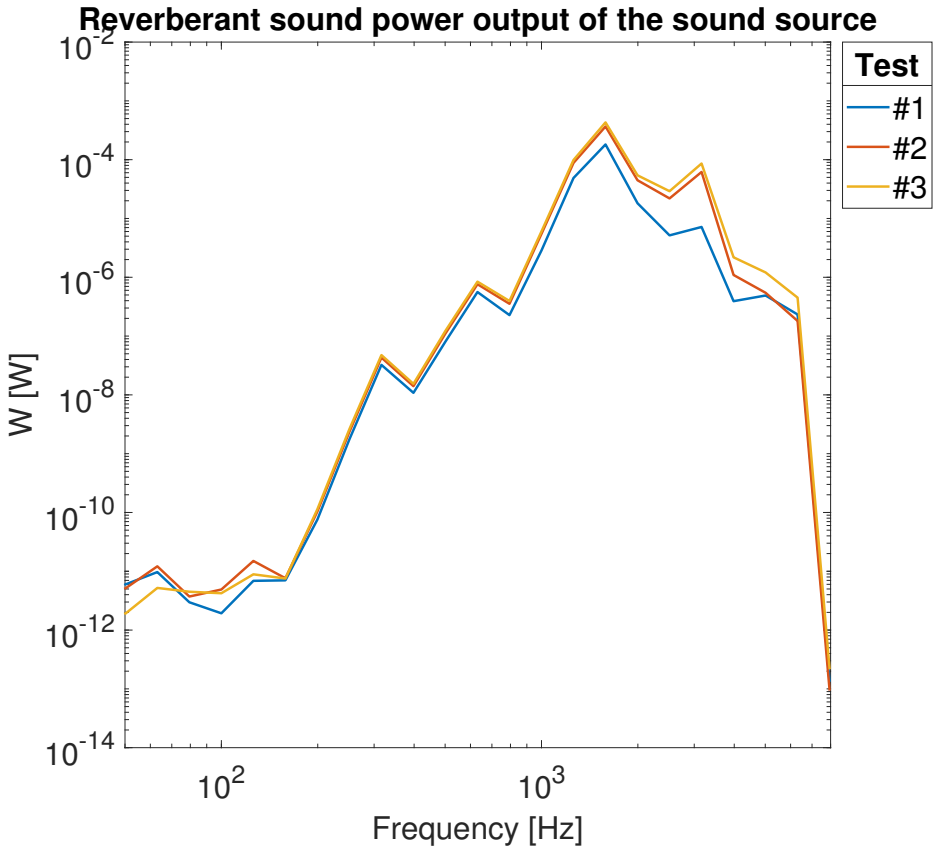

Figure 3.29: Foundation mock-up: reverberant sound power (W)

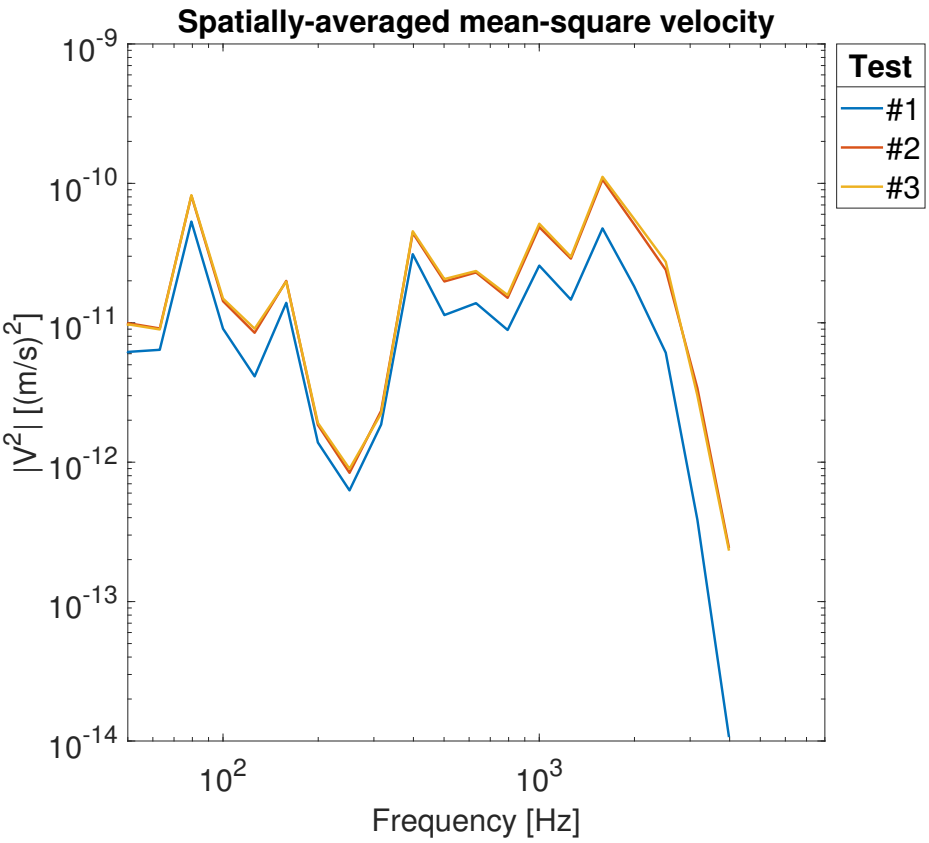

Figure 3.30: Foundation mock-up: spatially-averaged mean-square velocity ($\overline{|v_b|}^2$)

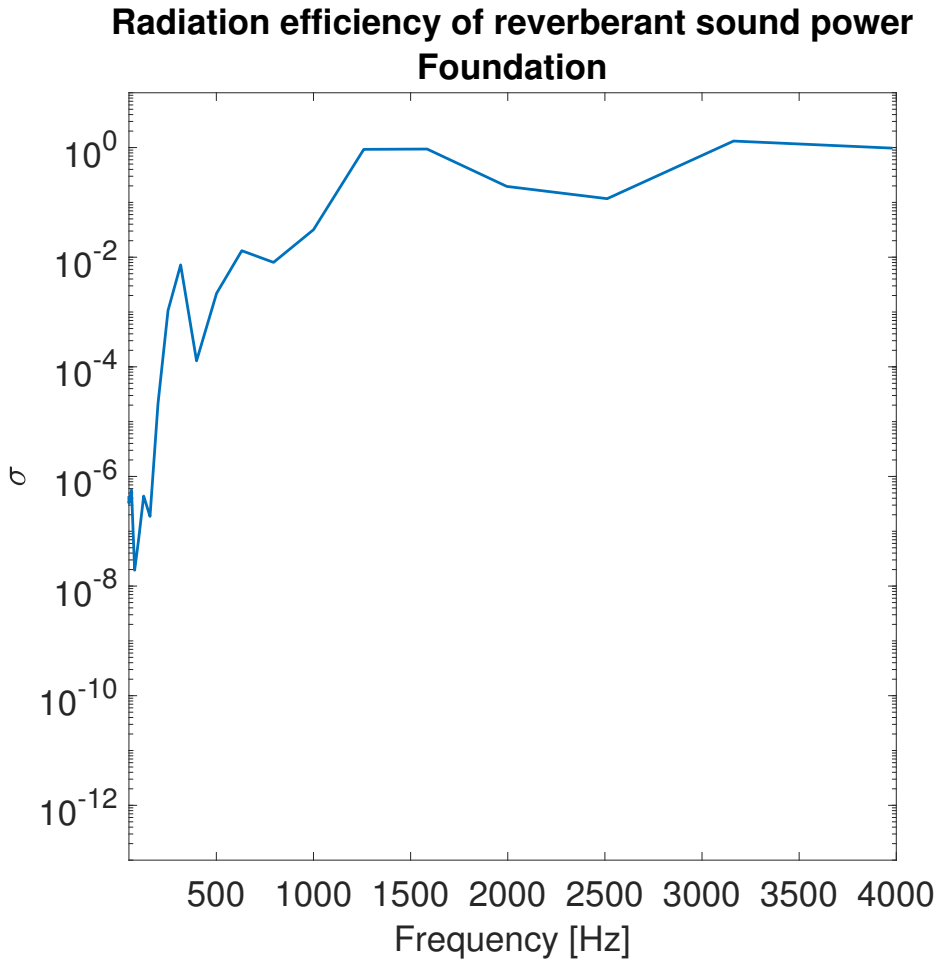

Figure 3.31: Foundation mock-up: radiation efficiency of reverberant sound power, third-octave band data

3.2.2.3 Transfer-path analysis of the dynamics of the foundation mock-up

We can use Equation (2.14) to represent how vibrations generated by a source (e.g. diesel engine) are transmitted through the vibration isolator and the foundation mock-up, and Equation (2.19) to calculate the resulting vibration levels of the base plate.

The mobility function levels $L_{M,\mathrm{f}}$ and $L_{M,\mathrm{b,f}}$ have been presented in Section 3.2.2.1. The isolator impedance level $L_{Z,21}$ can be obtained as described in [34, 35]. As an example, we will consider the cylindrical resilient mount analyzed in [34] and reported in Figure 3.17a. I measured the transmissibility response function of this component (ratio between the amplitude of the acceleration on the top and bottom surface [37], $T_{2,1}$). Then, I created a numerical model of the dynamic response of the component to a vertical harmonic excitation, optimized with a model updating procedure. From $T_{2,1}$ we can calculate the impedance ($Z_{2,1}$):

$$Z_{2,1} = \frac{F_2}{V_1} = \frac{a_2 \cdot m_{\mathrm{eff}}}{\frac{a_1}{\omega}} = \frac{a_2}{a_1} \cdot (\omega\, m_{\mathrm{eff}}) = T_{2,1} \cdot (\omega\, m_{\mathrm{eff}}) \tag{3.4}$$

where m_{eff} is the effective mass of the blocking mass of the test structure (in the tests described in [34], $m_{\mathrm{eff}} = 600\,\mathrm{kg}$).

Summing the engine velocity levels with the mobility levels on the top plate of the engine foundation (plotted in Figure 3.23) and the mechanical impedance levels of the vibration isolator, we can estimate the velocity levels on the top of the foundation with Equation (2.17). For example, we set $L_{v,s} = 100\,\mathrm{dB}$ re. $1 \times 10^{-9}\,\mathrm{m\,s^{-1}}$, uniform across the frequency range

of interest. $L_{v,s}$, $L_{Z,21}$, $L_{M,f}$, and the resulting values of $L_{v,f}$ are plotted in Figure 3.32. Figure 3.33 shows the values of $L_{v,\mathrm{b}}$ calculated from $L_{v,\mathrm{s}}$, $L_{Z,21}$, $L_{M,\mathrm{b,f}}$.

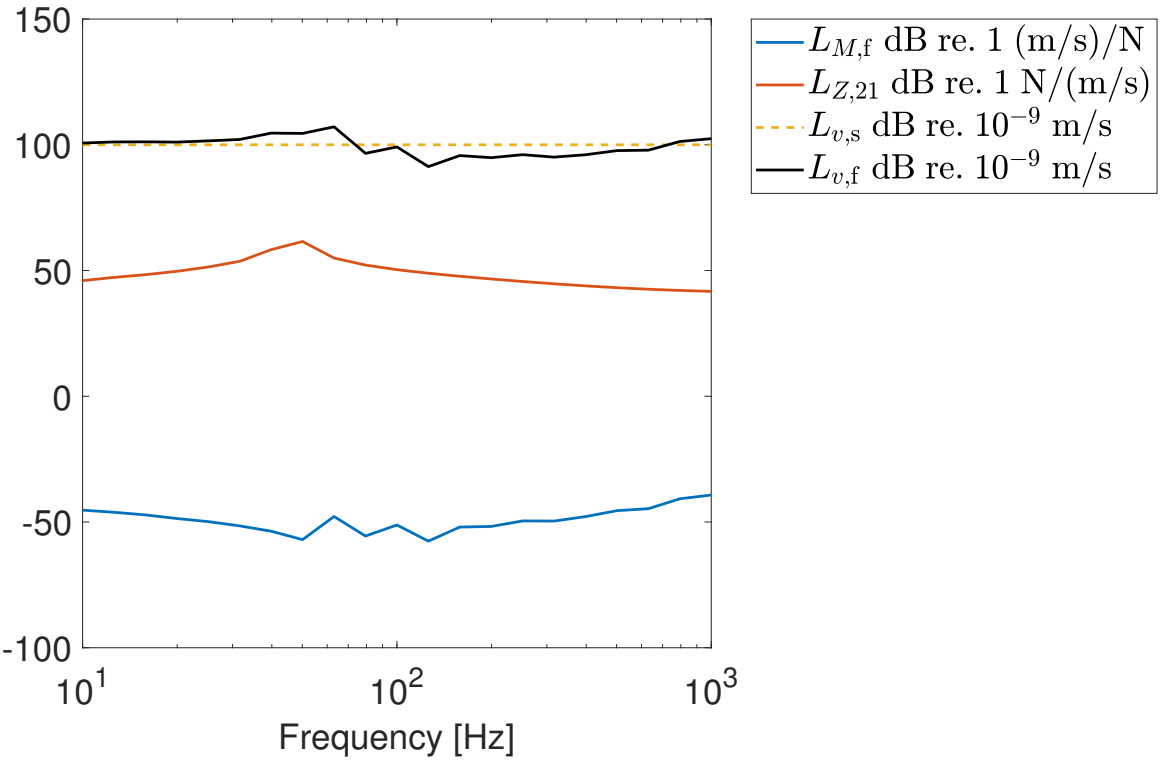

Figure 3.32: Transfer-path analysis from the engine noise source to calculate foundation velocity levels (top of the foundation)

The example of coupling of resilient mount with the foundation presented in Figure 3.33 highlights the importance of the transfer path analysis: the designer can characterize each component separately and understand their contribution to the global structure-borne sound propagation. In particular, we see that the foundation mock-up model and the vibration isolator under test don't provide a significant reduction in the energy levels transmitted through the foundation. Moreover, the resilient mount doesn't have internal modes of vibration in the frequency range of interest that can produce a resonance condition. From Equation (3.4), in order to achieve a significant reduction of vibration levels on the foundation, we need a

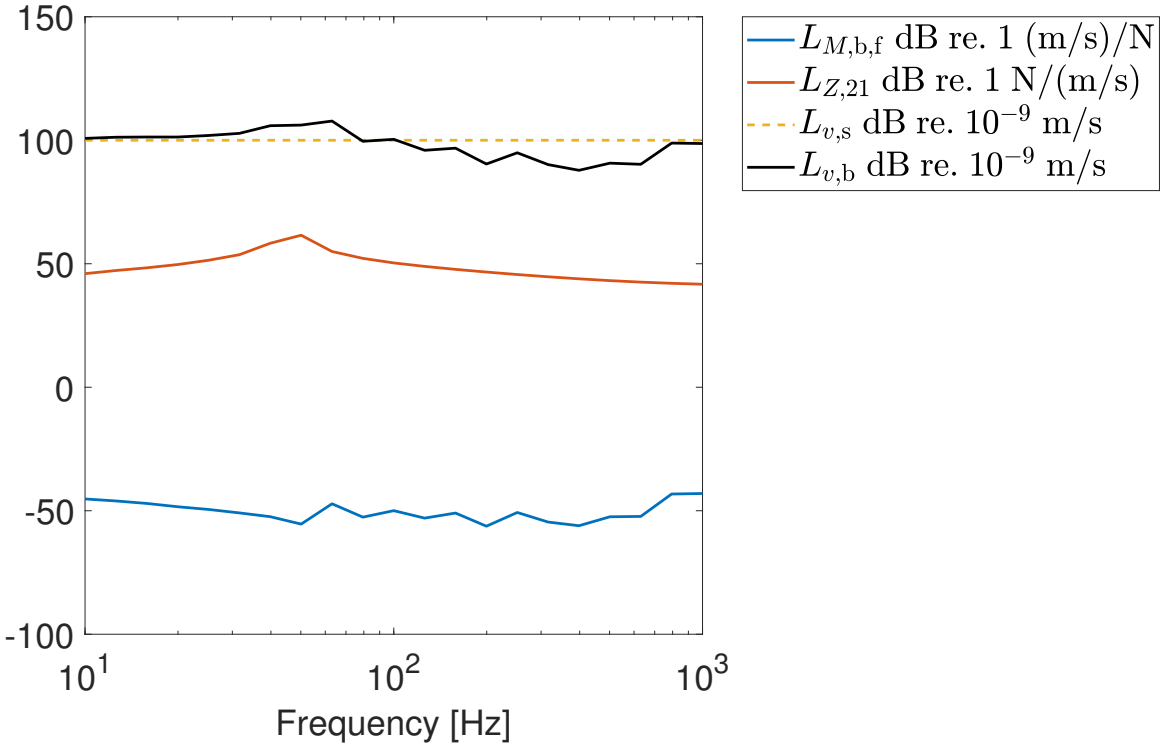

Figure 3.33: Transfer-path analysis from the engine noise source to calculate foundation velocity levels (base plate)

stiffer foundation and/or a softer isolator.

Numerical models are powerful tools that allow the designer to assess the effects of modifications on the components of the transfer path on the global sound radiation. Using the numerical model of the foundation presented in Section 2.2.8, we can modify the design of the foundation structure to decrease its transfer mobility and evaluate the effects of the design changes. In the same way, following the numerical procedures presented in [34, 35], we can evaluate the effect of any alteration of the rubber material of the resilient mount or the mount's shape on its impedance $L_{Z,21}$.

Chapter 4

Summary and final remarks

This Chapter summarizes the thesis' contents and resumes the main accomplishments of the work; finally, the plans to further augment the research project are outlined.

4.1. Summary

This thesis analyzes and improves transfer path analysis (TPA) of structure-borne noise produced by on-board sources. The work is focused on the noise and vibration produced by the medium-speed diesel engine of the ship because of its primary role in the vessel noise signature. TPA allows the designer to estimate noise and vibration levels at the receiving point as the composition of the source energy levels and the contributions of the components of the transfer path. With TPA, the dynamic behaviour of the elements of the transfer path can be represented as the composition of transfer functions that relate vibrational quantities measured at the interfaces of the components.

A key component of the TPA of the engine noise is the vibration isolator mounted under the diesel engine. A procedure is presented for the dynamic characterization of the vibration isolator, that yields an accurate estimate of the mechanical impedance of the component over the frequency range of interest, and detects potential resonance conditions in the dynamics of the isolator.

Moreover, the TPA of underwater radiated noise from marine vessels is investigated: the transfer path of structure-borne noise generated onboard is extended in order to include the dynamics of the engine foundation and the radiation through the water medium. The transfer contribution of the underwater radiation is measured with model-scale experimental tests and a numerical acoustic-structural analysis.

This thesis highlights the importance of numerical models in the TPA of structure-borne noise, and shows how finite-element dynamic simulations can be implemented in order to help the designer estimate the contribution of the components of the transfer path. Generally, the assessment of noise and vibration levels at the receiver point (onboard or underwater) requires full-scale experimental measurements performed in the operating conditions of the ship, that are not available in the design phase. Numerical models were used in the characterization of the isolator, in order to estimate the hyperelastic coefficients of the Yeoh model (static characterization) and the frequency-dependent modal damping ratios (dynamic characterization). The numerical model that was developed can be used to represent the dynamic behaviour of the isolator in the TPA. The numerical model of the underwater radiation in the deep tank provides an estimation of sound pressure levels in the deep tank in relation to the excitation applied to the vibrating structure. This model allows the designer to

estimate a coefficient of sound radiation efficiency (σ), that is used in the TPA of underwater sound radiation.

4.2. Conclusions and discussion on the outcomes

The achievements presented in the thesis can be subdivided into four main topics:

1. *Procedure for the static and dynamic characterization of vibration isolators* I developed a procedure to represent the response of resilient mounting elements to quasi-static compression and dynamic excitation. While previous works focused on simple cylindrical elements, this research developed an experimental characterization procedure that can be applied to rubber vibration isolators of all shapes and sizes. The resilient mount is modeled with a finite-element commercial code. The transfer characteristics of the isolator found with this procedure can be used in the TPA of the resiliently-mounted noise source.

    - The static characterization relies on the Yeoh model (a hyperelastic constitutive relation for rubber materials) to simulate the response of the isolator to a mono-axial compression force. Response Surface Methodology (RSM) is used to maximize the fit of the response of the numerical model to experimental compression tests using a small number of runs. Implicit time-integration schemes make the computational time of the numerical solution compatible with the needs of the modern marine industry.
    - The dynamic characterization simulates the response of the isolator to harmonic

excitation and highlights potential internal modes of resonance. A numerical modal analysis is performed on the optimized model developed in the static characterization. Similarly to what is done in the static characterization, the fit of the numerical model to the experimental transfer function is maximized by finding the optimal values of the frequency-dependent damping ratios. RSM makes it possible to analyze the variation of all the damping coefficients at the same time, keeping the number of numerical simulations to a minimum. Moreover, the model allows the designer to estimate the effect of the preload applied to the isolator on the damping performance of the component.

2. *Analytical formulation of the transfer path of underwater noise radiation of structure-borne noise sources using a single-point approach* This work extends the formulation of the balance equations of the transmission of noise and vibration from resiliently-mounted structure-borne noise sources in order to include the contribution of the ship foundation and the underwater radiation. Neglecting the coupling effect of the resilient mounting elements, a simple lumped-parameter representation is used to model each component of the transfer path. This allows the designer to estimate sound pressure levels at the underwater receiver as the combination of the transfer characteristics of the components of the transfer path.

3. *Numerical modeling of the underwater radiation from model-scale structures with complex geometry* Previous works analyzed the underwater sound radiation from vibrating structures with a simple geometry, in terms of coefficient of sound radiation efficiency

(σ). In this work, I performed the tests using a foundation mock-up composed of plates with different geometry and thickness, welded together. Despite the small size of the tank, and the reverberant field assumptions, the procedure yields accurate results and can be generalized to different geometries and testing conditions. In particular, this procedure can be adapted to provide a first estimate of sound radiation from full-scale vessels in deep water. Moreover, the comparison of the sound pressure levels measured experimentally and simulated with the numerical model developed in this research activity yields accurate results even below the threshold frequency of Equation (2.32).

4. *Use of numerical models in the simulation of components of the TPA of structure-borne noise* More broadly, this thesis gives the designer tools to represent the dynamic behaviour of the components of the transfer path of structure-borne noise sources using numerical models. As shown, finite-element simulations can produce a numerical model that represents the dynamic response of a component of the transfer path in normal steady-state operating conditions. The characterization of some components of the transfer path relies on the results of simple tests performed in standardized conditions, while the contribution of other elements can be estimated using numerical models built with a low amount of experimental data. The contributions of these numerical simulations can be combined together according to the analytical formulation presented in Section 2.2, in order to estimate vibration levels at the receiving point of the vibrational transfer path of structure-borne noise.

4.3. Limitations of this work and future developments

4.3.1. Limitations of the Yeoh material model

The static characterization of the vibration isolator performed in this work relies on the use of the Yeoh constitutive relationship for the modelling of the rubber material. The Yeoh coefficients are estimated with mono-axial compression tests. The resulting material model may yield inaccurate results when the rubber part of the resilient mount operates under multi-axial states of tension, because shear stresses aren't modeled directly in the constitutive relationship. In the cases presented, the model produced accurate results, but further investigation is needed in the case of a multi-dimensional force applied to the interface of the resilient mount.

4.3.2. Coupling effect between vibration isolators in the low-frequency range

An issue to consider in the dynamic analysis at low frequencies is the interaction in the dynamic response of the resilient mounts placed under the diesel engine. The analysis of the coupling effect of the vibration isolators requires the measurement of amplitude and relative phases of the forces transmitted through each isolator. The multi-point approach for the characterization of the vibration source and the dynamics of the isolators is presented in [36]. In addition, the presented mock-up simulates the typical configuration of a foundation-resilient mount system of a four-stroke diesel engine. Two-stroke diesel engines are not installed on rubber mounts and require an analysis focused on the low-frequency range due

to the low rotational speed.

4.3.3. Systematic errors in the tank tests

As discussed in Section 2.2.7, the experimental setup used in the tank tests cannot yield an accurate estimation of the sound pressure level in the low-frequency range. Due to the small tank size, below the threshold frequency of Equation (2.32), the modal density is not compatible with the assumption of reverberant field. To improve the accuracy of the results in the low-frequency range, the experiments should be repeated in a larger tank. Future work should also include tests in open water.

4.3.4. Extension of model-scale results to full-scale conditions

The coefficient of radiation efficiency (σ) depends on the geometry of the structure under test. The values of L_σ of the model-scale setup cannot be directly applied to full-scale conditions, and need to be validated with full-scale measurements. However, the values of L_σ measured in this work show the same trend of the results of [78, 99], and can be used as a first approximation in the full-scale URN analysis. Discrepancies in the values of σ might be more common in the low-frequency range.

4.3.5. Use of Statistical Energy Analysis in the high-frequency range

In the high-frequency range, the larger modal density may make deterministic modal analysis unreliable, especially in the case of large ship structures, due to the overlap between mode shapes and the influence of small variations of geometrical and material properties on the

response of the system. Statistical Energy Analysis [83] provides the designer with a simpler representation of the system, based on wave properties.

References

[1] Abrahamsen, K. (2012). The ship as an underwater noise source. In *Proceedings of Meetings on Acoustics ECUA2012*, volume 17, pages 1–10. Acoustical Society of America. 5

[2] Andrew, R. K., Howe, B. M., Mercer, J. A., and Dzieciuch, M. A. (2002). Ocean ambient sound: comparing the 1960s with the 1990s for a receiver off the california coast. *Acoustics Research Letters Online*, 3(2):65–70. 4

[3] ANSI/ASA S12.64-2009 (2009). Quantities and Procedures for Description and Measurement of Underwater Sound from Ships – Part 1: General Requirements. American national standard, Acoustical Society of America. 4

[4] Avcu, M. and Güney, A. (2018). Computation of dominant energy transmission paths for ship structure using a graph theory algorithm. *Ocean Engineering*, 161:136–153. 5

[5] Baş, D. and Boyacı, I. H. (2007). Modeling and optimization I: Usability of response surface methodology. *Journal of Food Engineering*, 78(3):836–845. 13, 30, 32, 33

[6] Beatty, M. F. (1987). Topics in finite elasticity: hyperelasticity of rubber, elastomers, and biological tissues—with examples. *Applied Mechanics Reviews*, 40(12):1699–1734. 21

[7] Beijers, C. (2005). *A Modeling Approach to Hybrid Isolation of Structure-Borne Sound*. PhD thesis, University of Twente. 8, 13

[8] Beijers, C. and de Boer, A. (2003). Numerical modelling of rubber vibration isolators. In *Tenth International Congress on Sound and Vibration*, pages 805–812. 14

[9] Beijers, C., Noordman, B., and de Boer, A. (2004). Numerical modelling of rubber vibration isolators: identification of material parameters. In *Proceedings of the 11th International Congress on Sound and Vibration*, pages 3193–3200. 6, 8, 9, 20, 64

[10] Bezerra, M. A., Santelli, R. E., Oliveira, E. P., Villar, L. S., and Escaleira, L. A. (2008). Response surface methodology (RSM) as a tool for optimization in analytical chemistry. *Talanta*, 76(5):965–977. 29, 32

[11] Biot, M. and De Lorenzo, F. (2007). Noise and vibration on board cruise ships: Are new standards effective? In *2nd International Conference on Marine Research and Transportation (ICMRT)*, volume 7, pages 93–100. 2

[12] Box, G. E. P. and Wilson, K. B. (1951). On the experimental attainment of optimum conditions. *Journal of the Royal Statistical Society. Series B (Methodological)*, 13(1):1–45. 31

[13] Boyce, M. C. and Arruda, E. M. (2000). Constitutive models of rubber elasticity: a review. *Rubber Chemistry and Technology*, 73(3):504–523. 21, 22

[14] Brandt, A. (2018). *ABRAVIBE: A MATLAB/Octave Toolbox for Noise and Vibration Analysis and Teaching*. Department of Technology and Innovation, University of Southern Denmark, 2.0 edition. 80

[15] Burella, G. and Moro, L. (2021). Design solutions to mitigate high noise levels on small fishing vessels. *Applied Acoustics*, 172:107632. 2, 6

[16] Burella, G., Moro, L., and Colbourne, B. (2019). Noise sources and hazardous noise levels on fishing vessels: The case of Newfoundland and Labrador's fleet. *Ocean Engineering*, 173:116–130. 2

[17] Carfagni, M., Lenzi, E., and Pierini, M. (1998). The loss factor as a measure of mechanical damping. In *Proceedings of the 16th International Modal Analysis Conference*, volume 3243, pages 580–584. 62

[18] Carlton, J. and Vlasic, D. (2005). Ship vibration and noise: some topical aspects. In *Proceedings of the 1st International Ship Noise and Vibration Conference*, pages 1–11. 5

[19] Charlton, D. J., Yang, J., and Teh, K. K. (1994). A review of methods to characterize rubber elastic behavior for use in finite element analysis. *Rubber Chemistry and Technology*, 67(3):481–503. 20

[20] Chen, V. C., Tsui, K.-L., Barton, R. R., and Meckesheimer, M. (2006). A review on design, modeling and applications of computer experiments. *IIE Transactions*, 38(4):273–291. 28

[21] Cintosun, E. and Gilroy, L. (2021). Estimating ship underwater radiated noise from onboard vibrations. In *SNAME Maritime Convention*. 11

[22] Cochard, N., Lacoume, J., Arzelies, P., and Gabillet, Y. (2000). Underwater acoustic noise measurement in test tanks. *IEEE Journal of Oceanic Engineering*, 25(4):516–522. 57, 58

[23] Cremer, L., Heckl, M., and Petersson, B. A. T. (2005). *Structure-borne sound*. Springer, 3rd edition. 51

[24] Czitrom, V. (1999). One-factor-at-a-time versus designed experiments. *The American Statistician*, 53(2):126–131. 13

[25] De Soto, N. A., Delorme, N., Atkins, J., Howard, S., Williams, J., and Johnson, M. (2013). Anthropogenic noise causes body malformations and delays development in marine larvae. *Scientific Reports*, 3(2831). 3

[26] Devriendt, C., Steenackers, G., De Sitter, G., and Guillaume, P. (2010). From operating deflection shapes towards mode shapes using transmissibility measurements. *Mechanical Systems and Signal Processing*, 24(3):665–677. 42

[27] Dylejko, P. G., MacGillivray, I. R., Moore, S. M., and Skvortsov, A. T. (2016). The influence of internal resonances from machinery mounts on radiated noise from ships. *IEEE Journal of Oceanic Engineering*, 42(2):399–409. 8

[28] EN ISO 10846-3 (2008). Acoustics and vibration - Laboratory measurement of vibro-acoustic transfer properties of resilient elements - Part 3: Indirect method for determination of the dynamic stiffness of resilient supports for translatory motion. Standard, International Organization for Standardization. 14, 38, 41, 78

[29] Erbe, C., Marley, S. A., Schoeman, R. P., Smith, J. N., Trigg, L. E., and Embling, C. B. (2019). The effects of ship noise on marine mammals—a review. *Frontiers in Marine Science*, 6. 3

[30] Fischer, R. W., Burroughs, C. B., and Nelson, D. L. (1983). *Design Guide for Shipboard Airborne Noise Control*. Society of Naval Architects and Marine Engineers (SNAME). 6

[31] Fragasso, J., Helal, K. M., and Moro, L. (2023). Transfer-path analysis to estimate underwater radiated noise from onboard structure-borne sources. *Applied Ocean Research*. Manuscript submitted for publication. 18, 64

[32] Fragasso, J. and Moro, L. (2019a). Design procedure to estimate the mechanical behaviour of resilient mounting elements for marine applications. In *PRADS 2019, 14th International Symposium on Practical Design of Ships and Other Floating Structures*. 18, 64

[33] Fragasso, J. and Moro, L. (2019b). Dynamic analysis of the stationary behavior of resilient mounting elements for marine applications. In *Proceedings of the IMAM Conference, Varna, Bulgaria*. 18, 41, 64

[34] Fragasso, J. and Moro, L. (2022). Structure-borne noise of marine diesel engines: Dynamic characterization of resilient mounts. *Ocean Engineering*, 261. 6, 18, 64, 105, 107

[35] Fragasso, J., Moro, L., Lye, L., and Quinton, B. W. T. (2019). Characterization of resilient mounts for marine diesel engines: prediction of static response via nonlinear analysis and response surface methodology. *Ocean Engineering*, 171:14–24. 6, 18, 36, 64, 84, 105, 107

[36] Fulford, R. and Gibbs, B. (1997). Structure-borne sound power and source characterisation in multi-point-connected systems, part 1: Case studies for assumed force distributions. *Journal of Sound and Vibration*, 204(4):659–677. 113

[37] Gajdatsy, P., Janssens, K., Desmet, W., and Van Der Auweraer, H. (2010). Application of the transmissibility concept in transfer path analysis. *Mechanical Systems and Signal Processing*, 24(7):1963–1976. 105

[38] Gil-Negrete, N., Vinolas, J., and Kari, L. (2006). A simplified methodology to predict the dynamic stiffness of carbon-black filled rubber isolators using a finite element code. *Journal of Sound and Vibration*, 296(4-5):757–776. 46

[39] Gobbert, M. K., Huang, X. C., Khuvis, S., Askarian, S., and Peercy, B. E. (2013). Coupled PDEs with Initial Solution From Data in COMSOL Multiphysics®. 60

[40] Goujard, B., Sakout, A., and Valeau, V. (2005). Acoustic comfort on board ships: An evaluation based on a questionnaire. *Applied Acoustics*, 66(9):1063–1073. 2

[41] Gray, L. M. and Greeley, D. S. (1980). Source level model for propeller blade rate radiation for the world's merchant fleet. *Journal of the Acoustical Society of America*, 67(2):516–522. 10

[42] He, J. and Fu, Z.-F. (2001). *Modal Analysis*. Butterworth-Heinemann. 62

[43] Hibbert, D. B. (2012). Experimental design in chromatography: A tutorial review. *Journal of Chromatography B*, 910:2–13. 30

[44] Hynnä, P. (2002). Vibrational power methods in control of sound and vibration. Research report BVAL37-021229, VTT Technical Research Centre of Finland. 6

[45] IMO MEPC.1/Circ.833 (2014). Guidelines for the reduction of underwater noise from commercial shipping to address adverse impacts on marine life. Guidelines, International Maritime Organization, London, England. 4

[46] Islam, S. M. (2022). Measurements of Underwater Radiated Noise from Non-cavitating Propellers in Atmospheric Towing Tank. Master's thesis, Memorial University of Newfoundland, Canada. 55, 58, 60, 61

[47] ISO 17208:2016 (2016). Underwater acoustics — Quantities and procedures for description and measurement of underwater sound from ships — Part 1: Requirements for precision measurements in deep water used for comparison purposes. Standard, International Organization for Standardization. 4

[48] ITTC 7.5-02-01-05 (2017). Model-Scale Propeller Cavitation Noise Measurements. Guideline, International Towing Tank Conference. 4, 57, 58

[49] Jeong, H., Lee, J.-H., Kim, Y.-H., and Seol, H. (2021). Estimation of the noise source level of a commercial ship using on-board pressure sensors. *Applied Sciences*, 11(3). 10

[50] Jones, A. D. and Hoefs, S. A. (1996). Acoustical properties of the MOD Salisbury test tank and techniques for measurements. Technical Report DSTO-RR-0068, Defence Science and Technology Organization, Canberra (Australia). 52

[51] Kari, L. (2001). Dynamic transfer stiffness measurements of vibration isolators in the audible frequency range. *Noise Control Engineering Journal*, 49(2):88–102. 14

[52] Kari, L. (2003). On the dynamic stiffness of preloaded vibration isolators in the audible frequency range: Modeling and experiments. *The Journal of the Acoustical Society of America*, 113(4):1909–1921. 8

[53] Kellett, P., Turan, O., and Incecik, A. (2013). A study of numerical ship underwater noise prediction. *Ocean Engineering*, 66:113–120. 3, 10

[54] Kinsler, L. E., Frey, A. R., Coppens, A. B., and Sanders, J. V. (2000). *Fundamentals of Acoustics*. John Wiley & Sons. 51

[55] Krause, P., Boyle, D., and Bäse, F. (2005). Comparison of different efficiency criteria for hydrological model assessment. *Advances in Geosciences*, 5:89–97. 35

[56] Kromulski, J. and Hojan, E. (1996). An application of two experimental modal analysis methods for the determination of operational deflection shapes. *Journal of Sound and Vibration*, 196(4):429–438. 42

[57] Li, D.-Q., Hallander, J., and Johansson, T. (2018). Predicting underwater radiated noise of a full scale ship with model testing and numerical methods. *Ocean Engineering*, 161:121–135. 3, 11

[58] Licciulli, F. (2006). *Caratterizzazione di Fondazioni di Motori per Applicazioni Navali tramite Analisi di Mobilità*. PhD thesis, University of Trieste. 6, 47

[59] Lin, T. R., Pan, J., O'Shea, P. J., and Mechefske, C. K. (2009). A study of vibration and vibration control of ship structures. *Marine Structures*, 22(4):730–743. 6

[60] Liu, W., Pan, J., and Matthews, D. (2010). Measurement of sound-radiation from a torpedo-shaped structure subjected to an axial excitation. In *Proceedings of the 20th International Congress on Acoustics, Sydney, Australia*. 9, 10

[61] Livermore Software Technology Corporation (2018a). *LS-DYNA® Keyword User's Manual - Volume I*. r:9393. 26

[62] Livermore Software Technology Corporation (2018b). *LS-DYNA® Keyword User's Manual - Volume II*. r:9393. 25

[63] Luo, R., Gahagan, P., Wu, W., and Mortel, W. (2001). Determination of rubber material properties for finite element analysis from actual products. In Besdo, D., Schuster, R. H., and Ihlemann, J., editors, *Constitutive Models for Rubber*, volume II, pages 257–260. Swets & Zeitlinger. 21

[64] Lye, L. (2002). Design of Experiments in Civil Engineering: Are We Still in the 1920's? In *Proceedings of the 30th Annual Conference of the Canadian Society for Civil Engineering, Montreal, Quebec, June*. 13

[65] McKay, M. D., Beckman, R. J., and Conover, W. J. (2000). A comparison of three methods for selecting values of input variables in the analysis of output from a computer code. *Technometrics*, 42(1):55–61. 82

[66] Molloy, C. (1957). Use of four-pole parameters in vibration calculations. *The Journal of the Acoustical Society of America*, 29(7):842–853. 38

[67] Montgomery, D. C. (2017). *Design and Analysis of Experiments*. John Wiley & Sons, 9th edition. 30, 31, 33, 34, 65, 67, 70

[68] Moriasi, D. N., Arnold, J. G., Van Liew, M. W., Bingner, R. L., Harmel, R. D., and Veith, T. L. (2007). Model evaluation guidelines for systematic quantification of accuracy in watershed simulations. *Transactions of the ASABE*, 50(3):885–900. 34, 35

[69] Moro, L. (2015). *Structure borne noise due to marine diesel engines: experimental study and numerical simulation for the prediction of the dynamic behaviour of resilient mounts*. PhD thesis, University of Trieste. 6, 8, 47, 48

[70] Moro, L. and Biot, M. (2013). Laboratory tests pave the way for the knowledge of dynamic response of resilient mountings on board ships. In *PRADS 2013, 12th International Symposium on Practical Design of Ships and Other Floating Structures*, volume 2, pages 853–860. 5, 7, 22

[71] Moro, L., Brocco, E., Mendoza Vassallo, P., Biot, M., and Le Sourne, H. (2015). Numerical simulation of the dynamic behaviour of resilient mounts for marine diesel engines. In Guedes Soares, C. and Shenoi, A. A., editors, *Proceedings of the 5th International Conference on Marine Structures (MARSTRUCT 2015)*, pages 149–157. 6, 8, 9, 13, 14, 22, 24, 38, 39, 64

[72] Myers, R. H., Montgomery, D. C., and Anderson-Cook, C. M. (2009). *Response Surface Methodology: Process and Product Optimization Using Designed Experiments*. John Wiley & Sons, 3rd edition. 28, 29, 30, 31

[73] Nash, J. E. and Sutcliffe, J. V. (1970). River flow forecasting through conceptual models: Part I - A discussion of principles. *Journal of Hydrology*, 10(3):282–290. 34

[74] Neitzel, R. L., Berna, B. E., and Seixas, N. S. (2006). Noise exposures aboard catcher/processor fishing vessels. *American Journal of Industrial Medicine*, 49(8):624–633. 2

[75] Nolet, V. (2017). Understanding anthropogenic underwater noise. Technical Report TP 15348 E, Green Marine. Prepared for Transportation Development Centre of Transport Canada. 4

[76] Nolet, V. (2021). Underwater noise pollution from shipping in the arctic report. Technical Report SAOIS203_2021_RVK-VIRTUAL1, Arctic Council. Prepared for Transportation Development Centre of Transport Canada. 4

[77] Oppenheimer, C. and Dubowsky, S. (1997). A radiation efficiency for unbaffled plates with experimental validation. *Journal of sound and vibration*, 199(3):473–489. 50

[78] Pan, X. (2017). Investigations on the total radiation efficiency of ribbed plates floating on water. 99, 114

[79] Pan, X., MacGillivray, I., and Forrest, J. (2016). The effect of boundary conditions and ribs on the total radiation efficiency of submerged plates. *Proceedings of ACUSTICS*. 10

[80] Petersson, B. and Gibbs, B. (1993). Use of the source descriptor concept in studies of multi-point and multi-directional vibrational sources. *Journal of Sound and Vibration*, 168(1):157–176. 48

[81] Petersson, B. and Plunt, J. (1980). Structure-borne sound transmission from machinery to foundations: final report. Technical Report 80-19, Department of Building Acoustics, Chalmers University of Technology. 6

[82] Petersson, B. and Plunt, J. (1982). On effective mobilities in the prediction of structure-borne sound transmission between a source structure and a receiving structure. *Journal of Sound and Vibration*, 82(4):517–540. 49

[83] Plunt, J. (1998). Statistical energy analysis – theory and applications, international masters programme in sound and vibration course: Technical acoustics ii. 115

[84] Rackl, M. (2015). Curve Fitting for Ogden, Yeoh and Polynomial Models. In *ScilabTEC, conference (Regensburg)*. 64

[85] Renaud, C., Cros, J.-M., Feng, Z.-Q., and Yang, B. (2009). The Yeoh model applied to the modeling of large deformation contact/impact problems. *International Journal of Impact Engineering*, 36(5):659–666. 22

[86] Rolland, R. M., Parks, S. E., Hunt, K. E., Castellote, M., Corkeron, P. J., Nowacek, D. P., Wasser, S. K., and Kraus, S. D. (2012). Evidence that ship noise increases stress in right whales. *Proceedings of the Royal Society B: Biological Sciences*, 279(1737):2363–2368. 3

[87] Sirimanne, S. N. (2022). Review of maritime transport. Technical Report UNCTAD/RMT/2022, United Nations Conference on Trade and Development. 3, 4

[88] Sjöberg, M. M. and Kari, L. (2002). Non-linear behavior of a rubber isolator system using fractional derivatives. *Vehicle System Dynamics*, 37(3):217–236. 8

[89] Spence, J. H. and Fischer, R. W. (2016). Requirements for reducing underwater noise from ships. *IEEE Journal of Oceanic Engineering*, 42(2):388–398. 5

[90] Sunde, E., Bråtveit, M., Pallesen, S., and Moen, B. E. (2016). Noise and sleep on board vessels in the Royal Norwegian Navy. *Noise & Health*, 18(81):85. 3

[91] Suzuki, H. and Yamaguchi, M. (2002). Comparison of FRF curve fitting methods for the loss factor measurements. In *INTER-NOISE and NOISE-CON Congress and Conference Proceedings*, pages 1060–1065. Institute of Noise Control Engineering. 37, 46

[92] Tarrago, M. G., Gil-Negrete, N., and Vinolas, J. (2009). Viscoelastic models for rubber mounts: influence on the dynamic behaviour of an elastomeric isolated system. *International Journal of Vehicle Design*, 49(4):303–317. 47

[93] Treloar, L. (1958). *The Physics of Rubber Elasticity*. Oxford University Press, 2nd edition. 21

[94] Turan, O. (2006). A Rational Approach for Reduction of Motion Sickness & Improvement of Passenger Comfort and Safety in Sea Transportation. Technical Report G3RD-CT-2002-00809, COMPASS. 2

[95] Turkmen, S., Aktas, B., Atlar, M., Sasaki, N., Sampson, R., and Shi, W. (2017). On-board measurement techniques to quantify underwater radiated noise level. *Ocean Engineering*, 130:166–175. 3, 11

[96] van der Seijs, M. V., de Klerk, D., and Rixen, D. J. (2016). General framework for transfer path analysis: History, theory and classification of techniques. *Mechanical Systems and Signal Processing*, 68:217–244. 6

[97] Vergassola, G., Pais, T., and Boote, D. (2018). Numerical tools and experimental procedures for the prediction of noise propagation on board superyachts. *Transactions of the Royal Institution of Naval Architects Part B: International Journal of Small Craft Technology*, 160(B1):9–16. 2

[98] Verheij, J. W. (1982). *Multi-path sound transfer from resiliently mounted shipboard machinery: Experimental methods for analyzing and improving noise control*. PhD thesis, TU Delft, Delft University of Technology. 7

[99] Wang, G., Li, W., and Liu, T. (2020). The average radiation efficiency of a plate immersed in water with general boundary conditions. *Mechanics Research Communications*, 106(103532). 99, 114

[100] Wang, Y. and Abrahamsen, K. (2019). Control of ship radiated underwater noise. In *OCEANS 2019 MTS/IEEE SEATTLE*, pages 1–5. IEEE. 5

[101] Weilgart, L. S. (2007). A brief review of known effects of noise on marine mammals. *International Journal of Comparative Psychology*, 20(2). 3

[102] Wilcove, G. L. and Schwerin, M. J. (2008). Shipboard habitability in the US Navy. *Military Psychology*, 20(2):115–133. 3

[103] Williams, R., Erbe, C., Ashe, E., and Clark, C. W. (2015). Quiet(er) marine protected areas. *Marine Pollution Bulletin*, 100(1):154–161. 3

[104] Wittekind, D. K. (2014). A simple model for the underwater noise source level of ships. *Journal of Ship Production & Design*, 30(1). 5

[105] Yeoh, O. (1993). Some forms of the strain energy function for rubber. *Rubber Chemistry and Technology*, 66(5):754–771. 21, 36

[106] Yokoyama, H., Miki, A., Onitsuka, H., and Iida, A. (2015). Direct numerical simulation of fluid–acoustic interactions in a recorder with tone holes. *The Journal of the Acoustical Society of America*, 138(2):858–873. 61

[107] Zacharias, C., Könke, C., and Guist, C. (2022). A new efficient approach to simulate material damping in metals by modeling thermoelastic coupling. *Materials*, 15(5). 62

[108] Zarnekow, M., Ihlenburg, F., and Grätsch, T. (2020). An efficient approach to the simulation of acoustic radiation from large structures with FEM. *Journal of Theoretical and Computational Acoustics*, 28(04). 10

[109] Zheng, H., Liu, G., Tao, J., and Lam, K. (2001). FEM/BEM analysis of diesel piston-slap induced ship hull vibration and underwater noise. *Applied Acoustics*, 62(4):341–358. 5

[110] Zytoon, M. A. (2012). Occupational injuries and health problems in the Egyptian Mediterranean fisheries. *Safety Science*, 50(1):113–122. 2